Development and assessment of a haemodynamic based numerical model for stenosis growth in the carotid artery

Stamou Aikaterini

January 2016

This thesis is submitted in partial fulfilment of the requirements for the award of the degree of Doctor of Philosophy of the University of Portsmouth

Abstract

A model for stenosis development in the carotid artery, employing the lattice Boltzmann method, is presented and its suitability is investigated and demonstrated. The development of a stenosis is modelled based on the blood flow; and the subsequent changes in the flow are examined. The model is applied to investigate the role of different haemodynamic markers on stenosis development and also the importance of modelling the non-Newtonian nature of the blood.

A stenosis growth model based on the time-averaged velocity magnitude at the wall is considered. The wall position where this marker has a minimum value is determined and the stenosis is allowed to develop at this point. The extent to which the stenosis develops is controlled by two parameters which are introduced. Simulations are then run based on the new geometry and a new position selected for stenosis development. The stenosis developed in this way was seen to be compatible with observations from the literature.

Simulations of stenosis development are presented to investigate the effect of the introduced model parameters to determine suitable ranges for their application. A range of parameters are determined over which the stenosis develops in an independent manner.

These parameters relate the extent to which the stenosis can grow in each development phase with no physical significance. It is important to find a variable which will describe the evolution in a manner which is independent of the model parameters.

As well as the time-averaged velocity magnitude, a selection of alternative markers were applied to the model. The results show that a number of markers involving near-wall velocity, wall shear stress, residential time, stagnation index and second invariant of the strain rate tensor, all resulted in a realistic stenosis. The oscillatory shear index, which gives a measure of the oscillatory nature of the shear, was found to not be a suitable marker, unless it was combined with the wall shear stress in the form of a ratio.

The effect of the non-Newtonian nature of blood on the stenosis development model is also considered. Here the non-Newtonian simulation showed noticeable differences compared to Newtonian; however both produced a realistic stenosis.

Declaration

Whilst registered as a candidate for the above degree, I have not been registered for any other research award. The results and conclusions embodied in this thesis are the work of the named candidate and have not been submitted for any other academic award.

I certify that to the best of my knowledge, any help received in preparing this thesis, and all sources used, have been acknowledged in this thesis.

.....

Aikaterini Stamou

January 2016

Acknowledgements

My first and greatest thank you must of course go to my supervisor Dr Jim Buick, he is, I am convinced, possessed of almost infinite patience and never seemed to mind answering subtly reworded questions many times. His actual faith in my qualities overall helped me to bring my career a step forward. The guidance, massive support and advice that he provided were invaluable, thank you so much Dr Jim Buick.

Thanks must also be given to my second supervisors Dr Jovana Radulovic and Prof Jie Tong for their overall guidance to the project and for always having a wise one. Massive thanks also are given to the laboratory technician Mr Robert Elliott for being continually happy and backing me up in the whole way to the completion of my PhD.

I would also like to thank my parents Christos Stamos and Polyxeni Stamou as well as my brother Dimitris Stamos who have been extremely supportive, loving and caring and brought me so far all along these years. I would also thank them for their investment in my education so far.

I would like to express my gratitude to the School of Engineering in the University of Portsmouth and the many members of staff who have taken an interest and supported my work.

Last but not least I would like to express my gratitude to the University of Portsmouth which funded the project, a project that could not be accomplished without this opportunity.

Contents

Abstract **i**

Contents **v**

Figures **x**

Tables **xv**

Symbols **xvi**

1 Introduction **1**

1.1 Navier-Stokes equations 2

1.2 Flow parameters 2

1.3 Numerical modelling 3

1.4 Lattice Boltzmann Method 4

1.5 Notation 4

1.6 Thesis Aims 4

1.7 Structure of the Thesis 5

2 The Lattice Boltzmann Method **6**

2.1 Fluid Analysis at several scales 6

2.2 Study at microscopic scale 7

2.3 Study at mesoscopic scale 7

2.3.1 The Bhatnagar Gross Krook (BGK) approximation 9

2.3.2 Conservation laws 10

2.4 Cellular Automata 11
2.4.1 The Lattice Gas Automata 11
2.4.2 The FHP Automaton 12
2.4.3 FHP collisions 14
2.5 From the Lattice Gas Automaton to the Lattice Boltzmann Method 16
2.6 D_2Q_9 lattice 17
2.6.1 Lattice symmetries 17
2.6.2 Distribution functions for the D2Q9 20
2.7 Chapman Enskog expansion 21
2.8 Application of the LBM algorithm 25
2.9 Boundary conditions 25
2.9.1 Bounceback scheme 26
2.9.2 Half-way bounceback scheme 26
2.9.3 Extrapolation scheme 27
2.9.3.1 Extrapolation boundary scheme 27
2.9.3.2 Inflow and outflow boundary conditions 30

3 LBM simulation of the carotid artery 31

3.1 Carotid artery geometry 31
3.2 Pulsatile flow 32
3.3 Simulation convergence 33
3.4 Non Newtonian simulations using the Carreau-Yasuda Model . . . 34
3.5 Set-up of the simulation 35
3.6 Model parameters 35

4 Literature on LBM applications 38

4.1 Lattice Boltzmann Modelling of flows 38
4.2 Lattice Boltzmann Modelling in general blood-flow projects 38
4.2.1 Lattice Boltzmann Modelling of blood flow in arteries . . . 39

4.2.2 Lattice Boltzmann Modelling of Blood Clotting 40
4.3 Cellular Nature of Blood 41
4.3.0.1 Lattice Boltzmann Modelling of Cellular Material in Blood flow 42
4.3.0.2 Non-Newtonian simulations 43
4.4 LBM modelling the flow in stenosed geometries 44

5 Medical problem **48**
5.1 Pathogenesis of atherosclerosis 48
5.2 Composition of the arterial wall 49
5.3 Localisation of Atherosclerosis 49
5.4 Association of haemodynamics to Atherosclerosis 50
5.4.1 Shear stress 50
5.4.1.1 Reaction of endothelium to shear stress 51
5.4.1.2 Association of shear stress variations with atherosclerotic processes 51
5.4.2 Flow separation and Geometry 52
5.4.2.1 Oscillatory flow 53
5.4.2.2 Oscillatory Shear Index 54
5.4.2.3 Relative Residence Time 55
5.4.3 High Shear Stress flow and Endothelial injury 55
5.5 Relationship of intimal media thickening to flow 56

6 Stenosis growth model **58**
6.1 Boundary movement mechanism 58
6.2 Boundary description and orientation 58
6.3 Selection criteria 61
6.3.1 Velocity magnitude 61
6.3.2 Tangential velocity 62

6.3.3 Wall Shear Stress 63
6.3.4 Second invariant of the deviatoric stress tensor 63
6.3.5 Oscillatory Shear Index (OSI) 64
6.3.5.1 Ratio OSI:WSS 64
6.3.6 Relative Residence Time 64
6.3.7 Reversibility Flow Indexes 65
6.3.8 Stagnation index 65
6.4 Boundary movement 65
6.5 Summary 67

7 Haemodynamics in a healthy artery 68

8 Stenosis model results 73
8.1 Illustration of stenosis growth 73
8.1.1 Layer Development 74
8.2 Stenosis Development 75
8.3 Applicable range of h 80
8.4 Applicable range of w 82
8.5 Flow profiles 83
8.6 Shear stress 85
8.7 Conclusion 87

9 Effect of stenosis growth 88
9.1 Stenosis development and wall Haemodynamics 91
9.2 Stenosis Development and time averaged wall haemodynamics . . 97
9.3 Conclusions 106

10 Alternative haemodynamic markers 108
10.1 Stenosis development 108
10.2 Geometrical development 115

10.3 Conclusion 126

11 Non-Newtonian model **128**

11.1 Introduction 128

11.2 Stenosis development 128

11.3 Conclusion 139

12 Conclusions **140**

12.1 Stenosis model 140

12.2 Wall haemodynamics 140

12.3 Haemodynamic markers 141

12.4 Non-Newtonian model 142

12.5 Future Directions 142

A **143**

A.1 Hamiltonian of a system 143

A.2 Collision integral 143

A.3 Summation properties 144

A.4 Chapman-Enskog expansion 144

A.5 Ethic Review 145

List of Figures

2.1 The FHP lattice 12

2.2 FHP collisions, inspired from Wolfram 15

2.3 The D_2Q_9 lattice 18

2.4 The half-way bounceback scheme 27

2.5 The extrapolation scheme 28

3.1 Carotid artery geometry. 32

3.2 Carotid artery velocity waveform, obtained from Holdsworth et al.. 33

3.3 Convergence of LBM simulation 34

6.1 Model for the wall development is shown for selected values of h and w; (a) $h = 0.5$, $w = 1$, (b) $h = 0.5$, $w = 2$, (c) $h = 0.15$, $w = 1$. The movement boundary scheme depends on h and w which have no physical significance. These parameters relate to the extent to which the stenosis can grow in each development phase. 60

7.1 Velocity and vorticity for the healthy artery 71

8.1 The development of the stenosis for $h = 0.7$ and $w = 1$. The stenosis geometry is shown at selected times corresponding to the final period during which each of the layer is developed. 74

8.2 Stenosis development in terms of T_s for different values of h, when compared to $h = 0.5$. 77

8.3 Stenosis development in terms of T_s^* for different values of h. . . . 78

8.4 Stenosis development in terms of T_s^{**} for different values of h. . . 79

8.5 ΔT_s^* for different values of h. 81

8.6 Comparison of $h = 0.3$ results for $w = 1$ and $w = 2$. 82

8.7 Velocity and vorticity at peak flow. 84

8.8 Velocity and vorticity during deceleration. 85

8.9 Shear stress at peak flow and during deceleration. 86

9.1 The development of the stenosis for $h = 0.3$ and $w = 1$. The stenosis geometry is shown at selected times corresponding to the final period during which each of the layer is developed. 90

9.2 Instantaneous $u^{(1)}$ on outer ECA over the cardiac pulse for (a) healthy artery, (b) $T_s = 249$, (c) $T_s = 368$, (d) $T_s = 381$, (e) $T_s = 408$ and (f) $T_s = 739$. 92

9.3 Instantaneous WSS on outer ECA over cardiac pulse for (a) healthy artery (b), $T_s = 249$, (c) $T_s = 368$, (d) $T_s = 381$, (e) $T_s = 408$ and (f) $T_s = 739$. 93

9.4 Instantaneous $u_t^{(1)}$ on outer ECA wall over cardiac pulse for (a) healthy artery, (b) $T_s = 249$, (c) $T_s = 368$, (d) $T_s = 381$, (e) $T_s = 408$ and (f) $T_s = 739$. 94

9.5 Instantaneous $u^{(1)}$ on outer ICA wall over the cardiac pulse for (a) healthy artery, (b)$T_s = 322$, (c) $T_s = 506$ and (d) $T_s = 739$. . 95

9.6 Instantaneous WSS on outer ICA wall over the cardiac pulse for (a) healthy artery, (b)$T_s = 322$, (c) $T_s = 506$ and (d) $T_s = 739$. . 96

9.7 Instantaneous $u_t^{(1)}$ at the outer ICA wall across the cardiac pulse for (a) healthy artery, (b)$T_s = 322$, (c) $T_s = 506$ and (d) $T_s = 739$. 97

9.8 (a) $\overline{u^{(1)}}$, (b) TAWSS, (c) OSI, (d) RRT and (e) O:WS on the outer wall of the ECA over the development of the stenosis. 99

9.9 (a) $\overline{u_t^{(1)}}$ and (b) RFI on the outer wall of the ECA over the development of the stenosis. 102

9.10 (a) $\overline{u^{(1)}}$, (b) TAWSS, (c) OSI, (d) RRT, (e) O:WS on the outer wall of the ICA over the development of the stenosis. 103

9.11 (a)$\overline{u_t^{(1)}}$ and (b) RFI on the outer wall of the ICA over the development of the stenosis. 104

9.12 (a) $\overline{u^{(1)}}_{\mathrm{f}}$ and (b) $\mathrm{RRT}_{\mathrm{f}}$ on the inner walls of the ECA and (c) and (d) on the inner walls of the ICA over the development of the stenosis. 105

10.1 Stenosis development in layers when the position of the development is determined by for triggers (a) $\overline{u^{(1)}}$, (b) $\overline{|u_t^{(1)}|}$, (c) TAWSS, (d) RFI, (e) SI, (f) RRT, (g) TAD_{II} (h) OSI and (i) O:WS . . . 110

10.2 Stenosis development for markers (a) $\overline{u^{(1)}}$, (b) $\overline{|u_t^{(1)}|}$, (c) TAWSS, (d) RFI, (e) SI, (f) RRT, (g) TAD_{II}, (h) OSI and (i) O:WS . . . 113

10.3 ΔT_s^*, where $X = \overline{u^{(1)}}$ and (a) Y=$\overline{|u_t^{(1)}|}$, (b) Y = TAWSS, (c) Y = RFI, (d) Y = SI, (e) Y = RRT, (f) Y = TAD_{II} and (g) Y = O:WS.115

10.4 ΔT_s^*, where X = O:WS, (a) Y = RFI, (b) Y = SI, (c) Y = RRT and (d) = Y = TAD_{II} 116

10.5 Area removed from (a) the ECA and (b) the ICA by the developing stenosis for different markers 117

10.6 Artery sections 117

10.7 Change in artery diameter as the stenosis develops along the sections a) S_1, (b) S_2, (c) S_3, (d)S_4, (e) S_5 and (f) S_6, for alternative markers. 118

10.8 $\overline{u^{(1)}}$ on outer wall of ECA, over the development of the stenosis when the applied marker is (a) $\overline{u^{(1)}}$, (b) O:WS, (c) RFI, (d) SI and (e) TAD_{II}. 120

10.9 RFI on outer wall of ECA, over the development of the stenosis when the applied marker is $\overline{u^{(1)}}$, (b) O:WS, (c) RFI, (d) SI and (e) TAD_{II}. 121

10.10 OSI on outer wall of ECA over the development of the stenosis when the applied marker is (a) $\overline{u^{(1)}}$, (b) O:WS, (c) RFI, (d) SI and (e) TAD_{II}. 122

10.11 $\overline{u^{(1)}}$ on outer wall of ICA, over the development of the stenosis when the applied marker is (a) $\overline{u^{(1)}}$, (b) O:WS, (c) RFI, (d) SI and (e) TAD_{II}. 123

10.12 RFI on outer wall of ICA, over the development of the stenosis when the applied marker is $\overline{u^{(1)}}$, (b) O:WS, (c) RFI, (d) SI and (e) TAD_{II}. 124

10.13 OSI on outer wall of ICA over the development of the stenosis when the applied marker is (a) $\overline{u^{(1)}}$, (b) O:WS, (c) RFI, (d) SI and (e) TAD_{II}. 125

11.1 Layer development of the stenosis using TAWSS as a marker for (a) the Newtonian model and (b) the non-Newtonian C-Y model. 129

11.2 Layer development of the stenosis using O:WS as a marker for (a) the Newtonian model and (b) the non-Newtonian C-Y model. . . 129

11.3 Stenosis development using TAWSS as a marker for (a) Newtonian model and (b) Non-Newtonian C-Y model and (c) their comparison. 130

11.4 Stenosis development using O:WS as a marker for (a) Newtonian model and (b) Non-Newtonian C-Y model and (c) their comparison. 131

11.5 Area removed from (a)the ECA and (b) the ICA by the developing stenosis using TAWSS and O:WS as markers for both the Newtonian and Non-Newtonian C-Y models. 132

11.6 Change in artery diameter as the stenosis develops along the sections a) S_1, (b) S_2, (c) S_3, (d)S_4, (e) S_5 and (f) S_6 using TAWSS and O:WS as a marker for both the Newtonian and Non-Newtonian models. 133

11.7 Near-wall haemodynamics over the development of the stenosis using TAWSS as a marker: ECA. 136

11.8 Near-wall haemodynamics over the development of the stenosis using TAWSS as a marker: ICA. 138

A.1 Ethical Committee Approval 146

A.2 UPR16 Form 147

List of Tables

2.1 Velocities, i and W_i for the D_2Q_9 lattice 20

3.1 Carotid artery parameters, based on Holdsworth *et al.* and equivalent Boltzmann scaled parameters 36

3.2 C-Y model parameters from Abraham *et al.* and equivalent Boltzmann scaled parameters. 37

9.1 Details of the stenosis development on the ICA and ECA walls for $h = 0.3$ $w = 1$. 89

9.2 Stenosis development in layers on the ICA and ECA for $h = 0.3$ $w = 1$ 90

Roman Symbols

$\mathbf{A}$	Selected site for stenosis development
A	Constant
A	Subscript used for a variable in SI units
$\mathbf{a}_j$	Sub-set of all fluid sites, $\mathbf{x}$, which are adjacent to the arterial wall
$\mathbf{B}$	Constant
B	Subscript used for a variable in Lattice Boltzmann units
$\mathbf{b}_j$	Boundary point lying at the intersection of the artery wall and a grid link
C	Constant
c_s	Speed of sound
D	Diameter
D_{II}	Second invariant of shear stress tensor
d	Artery diameter
$\mathbf{e}_i$	Link vectors connecting each site of a regular grid to its neighbours
$\mathbf{e}_n^{\mathbf{b}}$	Link vectors which but intersect the boundary
$\mathbf{F}$	Total applied force
$F_N(x, \mathbf{p}, t)$	Probabilistic distribution function for an N-body
F_s	s particles distribution function
f_i	Distribution function on link i
$f_i^{(eq)}$	Equilibrium distribution function on link i
$f_i^{(neq)}$	Non-equilibrium distribution function on link i
$f_i^{(k)}$	kth expansion of $f_i^{(neq)}$
f_i^1	Intermediate distribution function on link i after streaming
H	Hamiltonian
h	Incremental wall movement parameter
k_B	Boltzmann constant

$L(t)$	Error term used for convergence
$\mathbf{l}_j$	Grid based normal (out of the wall)
M	Mach number
m	Mass of a fluid molecule
m	Number of links cutting the boundary
N	Number of Periods
N_R	Number of time steps when the velocity is reversed
N_S	Number of time steps when the velocity is stagnant
$\mathbf{n}_j$	Normal vector to the wall
n	Parameter for C-Y model
n	Number of dimensions
n_i	Occupation number in the LGA:, the number of particles present on a link i
n	Empirically determined constant in C-Y model
$\mathbf{p}$	Momentum
p	Hydrostatic pressure
$Q(f,f)$	Collision integral
R	Gas constant
Re	Reynolds number
$S_{\alpha\beta}$	Strain rate tensor
S	Section
s	Number of particles in BBGKY equation
T	Period
T_s	Number of sites converted from wet to dry
T_s^*	Normalised T_s with respect a fixed number of site conversions
T_s^{**}	Normalised T_s with respect to the number of site conversions for the stenosis to reach the y buffer
T	Temperature

$\mathbf{t}_j$	Tangential vector at the wall
t	Time
$\mathbf{u}$	Fluid Velocity
$\overline{\mathbf{u}}$	Mean velocity
$\mathbf{u}_j^{(1)}$	Velocity at $\mathbf{a}_j$,1 lu from the wall
$\mathbf{u}_t^{(1)}$	Tangential component of $\mathbf{u}^{(1)}$
$\mathbf{u}_j^{(\delta)}$	Velocity a distance δ_j from the wall along direction l_j, at point $\mathbf{a}_j$
$\mathbf{u}_j^{l+\delta}$	Velocity a distance $\delta_j + l_j$ from the wall along direction l_j, at point $\mathbf{a}_j$
$\mathbf{u}'_w$	Fictitious velocity used in the extrapolation boundary scheme
V_s	Normalisation factor in BBGKY equation
W_i	Weight function for the equilibrium distribution function
w	Incremental wall movement parameter
$w_B(\mathbf{u})$	Maxwell distribution
X	Haemodynamic parameter
$\mathbf{x}$	Position
$\mathbf{x}_b$	Boundary point. The position where a link intersects the boundary
$\mathbf{x}_f$	Fluid site in extrapolation boundary scheme
$\mathbf{x}_{ff}$	Site used in extrapolation boundary scheme: $\mathbf{x}_{ff} = \mathbf{x}_f + \mathbf{e}_i$
Y	Haemodynamic parameter

Greek symbols

α	Empirically determined constant in C-Y model
α	Womersley parameter
$\dot{\gamma}$	Shear rate
Δ_i	Collision operator

ΔT_s^*	Different between the value of T_s^* for different wall parameters
δ	Stokes layer thickness
δ_i	Distance of fluid site from the wall along link i
δ_i^*	δ_i normalised by the link length
$\delta_{\alpha\beta j}$	Kronecker Delta
ϵ	Knudsen number
η	Dynamic shear viscosity
η_0	Limiting value of the viscosity in the low shear rate limit
η_∞	Limiting value of the viscosity in the high shear rate limit
λ	Empirically determined constant in C-Y model
ν	Kinematic shear viscosity
$\Pi_{\alpha\beta}$	Momentum flux tensor
ρ	Density
ρ'_w	Fictitious density used in the extrapolation boundary scheme
$\sigma_{\alpha\beta}$	Stress tensor
σ_y	Yield stress
$\sigma\left(\Omega\right)$	Differential cross-section
τ	Relaxation time
$\phi\left(\mathbf{u}\right)$	General collision invariant
$\psi\left(\mathbf{u}\right)$	Elementary collision invariant
Ω_i	BGK Operator for link i
ω	Angular frequency
$\boldsymbol{\omega}$	Vorticity

Mathematical Operators

∂_{x_α}	$\frac{\partial}{\partial x_\alpha}$

∂_x	$\frac{\partial}{\partial x}$
∂_t	$\frac{\partial}{\partial t}$
$< \alpha >$	Ensemble average of α
$x^{(i)}$	i^{th} order expansion of x
$x_{\mathrm{f}}(t)$	x normalised by its value at $t = 0$

Abbreviations

BBGKY	Bogolijubov, Born, Green, Kirkwood, Yvon
BGK	Bhatnagar Gross Krook
CCA	Common Carotid Artery
CFD	Computational Fluid Dynamics
C-Y	Carreau-Yasuda
ECA	External Carotid Artery
FDM	Finite Difference Method
FEM	Finite Element Method
FHP	Frisch, Hasslacher, Pomeau
FVM	Finite Volume Method
HPP	Hasslacher, Pazis and Pomeau
IB	Immersed Boundary
IB-LBM	Immersed Boundary-Lattice Boltzmann Method
ICA	Internal Carotid Artery
IMT	Intimal Media Thickening
LBGK	Lattice Boltzmann Models after named by Bhatnagar Gross Krook
LBM	Lattice Boltzmann Method
LDL	Low-Density Lipoprotein
LGA	Lattice Gas Automaton

N-S	Navier-Stokes
OSI	Oscillatory Shear Index
O:WS	Ratio OSI: TAWSS
RBC	Red Blood Cell
RFI	Reversible flow index
RRT	Relative Residence Time
SI	Stagnation index
TA	Time Averaged
TPA	Tissue Plasminogen Activator
WSS	Wall Shear Stress
2-D	Two-dimensional
3-D	Three-dimensional

Chapter 1

Introduction

Cardiovascular diseases have constituted a major cause of mortality in developed countries over the last decade [1]. Atherosclerosis is the main cardiovascular disease [1, 2] responsible for ischaemic stroke as it can lead to the progressive narrowing of blood vessels, due to a build-up of plaque. There is a growing body of evidence which suggests a correlation between regions of low Wall Shear Stress (WSS) and early development of atherosclerosis [3–8] in blood vessels. Within regions of low WSS, oscillatory flow may also be associated with regions where stenosis is observed to develop [9–11]. The haemodynamic (blood flow mechanics) parameters such as the velocity, shear stress and vorticity are some of the properties studied in relation to the progression of stenosis in the present project.

Examination of the haemodynamic parameters needs careful treatment because of the nature of the blood flow. Blood is a two-phase suspension of formed elements (e.g., red blood cells, white blood cells, platelets) [12–15] in plasma. Red Blood Cells (RBCs) constitute an important component in blood because of their large concentration [13, 14] and their crucial role in oxygen transfer [12, 16]. The RBC membrane is highly deformable so that the RBCs can pass through capillaries of as smalls as 4 µm inner diameter [17] after undergoing large deformation.

In certain cases, particularly in narrow arteries, the behaviour of the blood deviates from the standard Newtonian case of the constant viscosity and exhibit Non-Newtonian behaviour. Blood is a shear-thinning fluid [12, 18, 19] meaning that the viscosity is reduced in regions of high shear.

1.1 Navier-Stokes equations

Fluid (blood in our case) flow is governed by the Navier Stokes equations as well as the continuity equation. Assuming the case of incompressible flow (constant density, ρ), its behaviour is described by the Navier-Stokes equation:

$$\frac{\partial \mathbf{u}}{\partial t} + (\mathbf{u} \cdot \nabla)\mathbf{u} = -\frac{\nabla p}{\rho} + \nu(\bigtriangledown^2)\mathbf{u}, \tag{1.1}$$

accompanied with the continuity equation,

$$\nabla \cdot \mathbf{u} = 0, \tag{1.2}$$

where $\mathbf{u}$ is the fluid velocity, p is the hydrostatic pressure and $\nu = \frac{\eta}{\rho}$ is the kinematic shear viscosity with η the dynamic shear viscosity.

1.2 Flow parameters

Blood flow can be described by the dimensionless parameters, Reynolds number, Mach number and Womersley parameter. The Reynolds number, Re, for flow in a section of diameter D, is expressed as:

$$Re = \frac{\rho u D}{\eta} = \frac{uD}{\nu}. \tag{1.3}$$

The Mach number, M, is expressed as:

$$M = \frac{u}{c_s}, \tag{1.4}$$

when c_s is the speed of sound. The Womersley parameter α, is expressed as:

$$\alpha = \frac{D}{2}\sqrt{\frac{\omega}{\nu}}, \tag{1.5}$$

where ω is the angular frequency. For low values of α, the flow is quasi-steady and the instantaneous flow is approximately parabolical with the amplitude proportional to the pressure gradient. At high values of α the flow reaches the acoustic limit with approximately uniform flow across the diameter (except close to the walls) and is out of phase with the pressure gradient. In the carotid artery $\alpha \simeq 4.5$ and so takes an intermediate value. This results in flow, which for a purely oscillatory pressure gradient, can have a positive velocity profile towards the centre of the section and a negative profile closer to the walls, or vice-versa.

1.3 Numerical modelling

Most fluid flow problems are too complex to be solved analytically and so a numerical solution to the Navier-Stokes equations, Equation (1.1) is required. The most commonly used classical approaches to the discrete solution [20] are the Finite Difference Method (FDM), the Finite Element Method (FEM) and the Finite Volume Method (FVM). Here, we implement a more novel approach, the Lattice Boltzmann Method (LBM) [21, 22].

1.4 Lattice Boltzmann Method

The LBM [23, 24] is a relatively recent approach to Computational Fluid Dynamics (CFD) which differs from the conventional commercial solvers [25–28]. LBM has attracted interest from researchers in a broad range of fields such as acoustically induced flows [29], bubble dynamics [30], free surface flows [31] and flow in porous media [32] as well as a range of blood flow simulations [33–43]. Its strength is based on its simple coding and its local application. Briefly, the LBM describes the flow in a mesoscopic manner. The fluid is comprised of a set of fictitious particles [21, 24] moving on the nodes of a Cartesian lattice, represented by distribution functions f_i, with i the index for a link which connects each grid node to its nearest neighbours. The LBM, from which physical properties of the flow can be determined, will be described in detail in Chapter 2.

1.5 Notation

Throughout this thesis, Roman index will be used to represent a label and a Greek index to represent a component. Summation over repeated Greek indices will be assumed. For example, in f_i the 'i' labels the distribution function with, typically, i in the range 0 - 6. The component of the velocity $\mathbf{u}$ in the α-direction is expressed as u_α, with α = 1,2 in a 2D simulation. The dot produce $\mathbf{u} \cdot \mathbf{u} = \sum_{\alpha=1}^{2} u_\alpha u_\alpha$ or $u_\alpha u_\alpha$ for short.

1.6 Thesis Aims

The aim of the present work is to develop and investigate a numerical model for the development of a stenosis in the carotid artery. In particular, the development of a stenosis is modeled based on the haemodynamical properties of the

blood flow; and the subsequent changes in the flow are examined as the stenosis develops. This blood modelling work has been undertaken with the Lattice Boltzmann Method (LBM) [23,24]. The non-Newtonian nature of blood will also be considered, as will the manner in which this affects the stenosis development.

1.7 Structure of the Thesis

In the present chapter, Chapter 1, an introduction to the main concepts is presented. In Chapter 2, the concept and application of the Lattice Boltzmann Method is developed in detail. Chapter 3 presents details of the LBM simulation specific to its application here. In Chapter 4 a review on blood modelling simulations with the LBM is presented. Chapter 5 presents a literature review of the medical problem. The original achievevents within the PhD Thesis are presented as follows. In Chapter 6, the stenosis development model is described. Chapter 7 presents the flow fields for a healthy artery. In Chapter 8, simulations of stenosis development are presented to investigate the performance of the model and to determine suitable ranges for its application. In Chapter 9, haemodynamics during stenosis development is studied. In Chapter 10, alternative methods, based on alternative haemodynamic markers are presented and investigated. In Chapter 11, the influence of non-Newtonian nature of blood on the stenosis development is considered. The conclusions are set out in Chapter 12. Chapters 2-5 provide a review of existing literature and Chapters 6-11 document the novel work of this thesis.

Chapter 2

The Lattice Boltzmann Method

The present chapter is devoted to the Lattice Boltzmann Method (LBM). It considers the continuous Boltzmann equation as well as the Lattice Gas Model which preceded the LBM. The method is described and developed; and it is shown to satisfy the Navier-Stokes equation. Aspects of its implementation are also considered.

2.1 Fluid Analysis at several scales

Fluids, such as air and water, are common in our daily life. From a physics viewpoint, all fluids are composed of a large set of atoms or molecules that collide one with the other [44–47] and whose motion contains a random component. In contrast, the microscopic dynamics of the fluid [47, 48], which is the average of the motion of the molecules, is homogeneous and continuous. The motion of a fluid can be described with mathematical models with regards to these scales; microscopic models at molecular scale, mescoscopic scale subjected to kinetic theories and the macroscopic scale undergoing continuum mechanics principles.

2.2 Study at microscopic scale

In microscopic analysis, a fluid is regarded as a set of fluid molecules. Then, the position and momentum of each molecule is tracked. Under these circumstances, the accumulative dynamics of a fluid system can be computed. The molecular dynamics of a fluid is described [44, 47, 48] by Newton's second law, expressed as:

$$\mathbf{F}_i = m\ddot{\mathbf{x}}_i, \tag{2.1}$$

where m is the mass of a fluid molecule and $\mathbf{x}_i$ and $\mathbf{F}_i$, are the position vector of the i molecule and the total force applied to it, respectively. A fluid can be described microscopically with the Hamiltonian of a N-Body system [21] considered, $H = H(\mathbf{x}, \mathbf{p}, t)$, where $\mathbf{x} = (\mathbf{x}_1, \mathbf{x}_2, .., \mathbf{x}_N)$ are the N spatial molecules and $\mathbf{p} = (\mathbf{p}_1, \mathbf{p}_2, .., \mathbf{p}_N)$ are the N corresponding momentums. H is the total energy of the system composed by the kinetic energy and the potential energy due to molecular interactions. However, the study of the fluid flow, even in a small volume, is troublesome because of the vast number of molecules [49, 50] which yields this research impractical. This highlights the need to investigate fluid flow at a higher level, such as the mesoscopic.

2.3 Study at mesoscopic scale

From the viewpoint of mesoscopic physics, the N-body fluid system can be described through employing the concept of a probabilistic distribution function $f_N(\mathbf{x}, \mathbf{p}, t)$ in the 3N space-momentum phase. This probabilistic distribution determines, [46, 47], the probability $f_N(\mathbf{x}, \mathbf{p}, t)$ that a system is found in the state $([\mathbf{x}_N, \mathbf{x}_N + d\mathbf{x}_N], [\mathbf{p}_N, \mathbf{p}_N + \mathbf{dp}_N])$. The distribution function f_N contains all the statistics information characterising the N particles. f_N satisfies the Liouville

equation [51]:

$$\frac{df_N}{dt} = \frac{\partial f_N}{\partial t} + \sum_i^N \left[\frac{\partial f_N}{\partial p_i}\dot{p}_i + \frac{\partial f_N}{\partial x_i}\dot{x}_i \right] = 0, \tag{2.2}$$

with $\mathbf{p}_i$ the momentum of the i particle, $\mathbf{x}_i$ the position vector of the i particle. Based on the definitions for H given by equations (A.1), (A.2), equation (2.2) can be re-written as:

$$\frac{\partial f_N}{\partial t} - \sum_i^N \left[\frac{\partial H}{\partial x_i}\frac{\partial f_N}{\partial p_i} - \frac{\partial H}{\partial p_i}\frac{\partial f_N}{\partial x_i} \right] = 0. \tag{2.3}$$

A shrinking into $d\mathbf{x}$ can be achieved through integration by parts, [52], to give:

$$F_s\left(\mathbf{x}_1, \mathbf{p}_1, .., \mathbf{x}_N, \mathbf{p}_N, t\right) = V^s \int f_N\left(\mathbf{x}_1, \mathbf{p}_1, .., \mathbf{x}_N, \mathbf{p}_N, t\right) d\mathbf{x}_{s+1} d\mathbf{p}_{s+1} \; .. \; d\mathbf{x}_N d\mathbf{p}_N, \tag{2.4}$$

defining a so called s-particles distribution function, where V^s works as a normalisation factor and $1 \leq s \leq N$. This is the called BBGKY equation [52] after Bogoljubov, Born, Green, Kirkwood and Yvon. The BBGKY hierarchy is identical to the Liouville equation. The BBGKY needs to be truncated at some point to calculate approximate solutions. Starting from the BBGKY equation Boltzmann derived the Boltzmann equation [53]. Even though the Boltzmann equation is based on the BBGKY, it employs at its core a number of approximations:

- The case of $s = 2$, considers only two-particle collisions.
- Before the two particles collide their velocities are uncorrelated.

The Boltzmann equation for this case is expressed [51], in the absence of a body force, as:

$$\partial_t f + \mathbf{u} \cdot \partial_{\mathbf{x}} f = Q\left(f, f\right), \tag{2.5}$$

where $\mathbf{u} = \dfrac{\mathbf{p}}{m}$ is the particle velocity, m is a constant particle mass, f the velocity distribution function defined as $f\left(\mathbf{x}, \mathbf{u}, t\right)$ and $f\left(\mathbf{x}, \mathbf{u}, t\right) d^3x d^3u$ is the probability of finding a particle in the 3-D d^3x box around $\mathbf{x}$, the position vector, and velocity

over $\mathbf{u}$ to $\mathbf{u}+d\mathbf{u}$, $\mathbf{u}=(u_1,u_2,u_3)$. The $Q\left(f,f\right)$ is the collision integral (equation (A.3)) describing the two particles collision [54]. The collision integral may be shown to possess four elementary collision invariants $\psi_k(\mathbf{u})$ [54–56], $k=0,1,2,3$, such that:

$$\int Q\left(f,f\right)\psi_k\left(\mathbf{u}\right)d^3u=0, \tag{2.6}$$

with $\psi_0=1$, $(\psi_1,\psi_2,\psi_3)=\mathbf{u}$ and $\psi_4=\mathbf{u}^2$. General collision invariant $\phi(\mathbf{u})$ can have the form of a linear combination of ψ_k: $\phi\left(\mathbf{u}\right)=A+\mathbf{B}\cdot\mathbf{u}+C\mathbf{u}^2$ with A, $\mathbf{B}$, C constants. It can be further shown [54, 57] that there are positive functions f which give $\int Q(f,f)\mathbf{x}_i d^3\mathbf{u}=0$. The functions f are of the form [52], $f(\mathbf{u})=\exp\left(A+\mathbf{B}\cdot\mathbf{u}+C\mathbf{u}^2\right)$ where C must be negative. The Maxwell distribution [58, 59] given by:

$$f^M=f\left(\mathbf{x},\mathbf{u},t\right)=4\pi\mathbf{u}^2\left(\frac{m}{2\pi k_BT}\right)^{\frac{3}{2}}\exp\left[-\frac{m}{2k_BT}\left(\mathbf{u}-\overline{\mathbf{u}}\right)^2\right], \tag{2.7}$$

is special among these solutions, where $\overline{\mathbf{u}}$ is the mean velocity,

$$\overline{\mathbf{u}}=\frac{1}{N}\int\mathbf{u}f\left(\mathbf{x},\mathbf{u},t\right)d^3u. \tag{2.8}$$

Equation (2.7) may be re-written as:

$$f^M\left(\mathbf{x},\mathbf{u},t\right)=4\pi\mathbf{u}^2\left(\frac{1}{2\pi RT}\right)^{\frac{3}{2}}\exp\left[-\frac{\left(\mathbf{u}-\overline{\mathbf{u}}\right)^2}{2RT}\right], \tag{2.9}$$

where $R=\dfrac{k_B}{m}$ is the gas constant with k_B the Boltzmann constant, T the temperature and m the molecular mass.

2.3.1 The Bhatnagar Gross Krook (BGK) approximation

The collision integral $Q(f,f)$, as seen in equation (2.5), can be approximated with a simplified operator proposed by [60], the BGK (Bhatnagar Gross Krook)

operator. The BGK operator $-\frac{1}{\tau}\left(f - f^{(eq)}\right)$, where τ is the relaxation time, has to satisfy the constraints; it conserves the collision invariants ψ_k of $Q(f, f)$:

$$\int \psi_k \left[-\frac{1}{\tau}\left(f - f^{(eq)}\right)\right] d^3x d^3u = 0, \tag{2.10}$$

for $k = 0, 1, 2, 3, 4$. The BGK operator reflects the overall effect of inter-molecular collisions. The term $f^{(eq)}$ is the equilibrium distribution function for the particle to lie in the equilibrium state and is taken as f^M. According to the constraint, equation (2.10):

$$\frac{1}{\tau}\left[\int \psi_k f^{(eq)}(\mathbf{x}, \mathbf{u})\, d^3x d^3u - \int \psi_k f(\mathbf{x}, \mathbf{u}, t)\, d^3x d^3u\right] = 0 \tag{2.11}$$

meaning that at any space point and time instant $f^{(eq)}(\mathbf{x}, \mathbf{u})$ must describe the same density, velocity and temperature, as described by $f(\mathbf{x}, \mathbf{u}, t)$ [54].

2.3.2 Conservation laws

Conservation laws can be determined by multiplying the Boltzmann equation, equation (2.5), with a collision invariant for $i = 0, 1, 2, 3, 4$ and integrating with respect to $\mathbf{u}$. Using equation (2.6) we see that for $i = 0$:

$$\int (\partial_t + \mathbf{u}\partial_x) f(\mathbf{x}, \mathbf{u}, t)\, d^3u = 0, \tag{2.12}$$

which gives [52]:

$$\partial_t \rho + \partial_x (\rho u) = 0, \tag{2.13}$$

where $\rho = \int f d^3u$. Considering $i = 1, 2, 3, 4$, gives:

$$\int \left(u_\alpha + u_\beta + u^2\right)(\partial_t + u_\alpha \partial_{x_\alpha}) f(\mathbf{x}, \mathbf{u}, t)\, d^3u = 0, \tag{2.14}$$

which expands to

$$\int u_\alpha \partial_t f(\mathbf{x},\mathbf{u},t)\, d^3u + \int u_\alpha u_\alpha \partial_{x_\alpha} f(\mathbf{x},\mathbf{u},t)\, d^3u + \int u_\alpha u_\beta \partial_{x_\beta} f(\mathbf{x},\mathbf{u},t)\, d^3u = 0 \tag{2.15}$$

which can be written:

$$\rho \partial_t u_\alpha + \rho u_\beta \partial_{x_\beta} u_\alpha = -\partial_{x_\beta} \Pi_{\alpha\beta} \tag{2.16}$$

since $\rho u_\alpha(\mathbf{x},t) = \int u_\alpha f(\mathbf{x},\mathbf{u},t)\, d^3u$ and $\Pi_{\alpha\beta} = \int u_\alpha u_\beta f(\mathbf{x},\mathbf{u},t)\, d^3u$, is the momentum flux tensor.

2.4 Cellular Automata

Cellular Automata are mathematical models introduced by von Neumann and Ulam [61]. A cellular automaton consists of a lattice, where each discrete site can take on a finite number of states, at each discrete time [62, 63]. The automaton evolves in discrete timesteps at discrete sites, the condition of which is updated by either deterministic or nondeterministic rule. The rules for the evolution of a site depend only on local neighbourhood sites around it [52]. The Lattice Gas Automaton (LGA) is a Cellular Automaton developed for the simulation of fluid dynamics.

2.4.1 The Lattice Gas Automata

The Lattice Gas Automaton is used for the simulation of fluid dynamics problems. In a Lattice Gas Automaton the fluid is treated as a set of simulated particles residing on the sites of the lattice, as shown in Figure 2.1. LGA situations are updated in two parts; streaming and collision. The streaming consists of simple particle transpositions from site $\mathbf{x}$ to the site $\mathbf{x}+\mathbf{e}_i$, where $\mathbf{e}_i$ are the link vectors

connecting each site on a regular lattice to their neighbours as shown in Figure 2.1 for a hexagonal lattice. Streaming can be expressed as:

$$n_i\left(\mathbf{x}+\mathbf{e}_i, t+1\right) = n_i\left(\mathbf{x}, t\right), \tag{2.17}$$

where n_i is the occupation number: the number of particles present on the link i. A hexagonal grid was used since this was the simplest (with only 7 links) grid which provided adequate symmetry. For the hexagonal lattice, shown in Figure 2.1, $i = 0, .., 6$ is a label, corresponding to the 6 links, connecting the site to its neighbours and $i = 0$ is a 'rest particle' with $\mathbf{e}_0$ the null vector. When particles

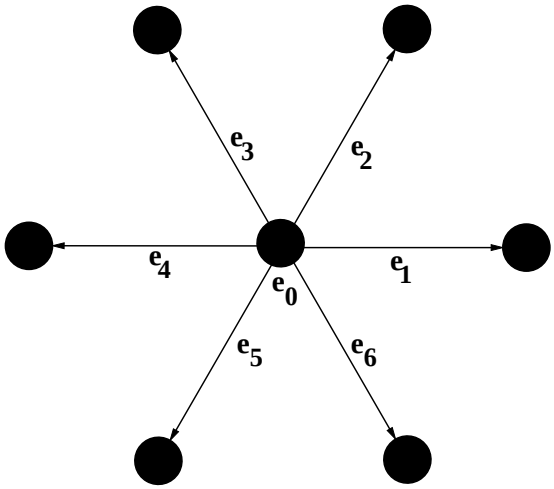

Figure 2.1: The FHP lattice

approach a site, they collide [21, 52]. In collision, the conservation of mass and momentum are satisfied at each node. The collision is grid dependent and will be discussed in Section 2.4.3.

2.4.2 The FHP Automaton

The first Lattice Gas Automaton was known as HPP, introduced by Hasslacher, Pazzis and Pomeau [64]. The HPP model operated on a square lattice where the limited number of collisions produced non-physical effects [65, 66]. The difficulties

of the HPP model were overcome by Frisch, Hasslacher, Pomeau (FHP) [66, 67] for the two dimensional (2-D) Navier-Stokes.

The FHP automaton evolved on a lattice with hexagonal symmetry such that each site is surrounded by six neighbours. The six neighbours are connected by the displacement vectors $\mathbf{e}_i$, with $i = 0, 1, .., 6$, as shown in the Figure 2.1. Particles were allowed to travel on these 6 links, and also remain at rest (rest particles) on each null link $\mathbf{e}_0$.

The following rules were updated to the FHP model.

- All the particles carry the same mass $m = 1$.
- Particles can either move along one of the $\mathbf{e}_i$, $i = 1, .., 6$ at unit speed or remain at rest, at $\mathbf{x}$. In each streaming step, lasting a time-step, the particles either shift to their nearest neighbours or remain at rest.
- Only one particle is allowed on each link such that:

$$n_i(\mathbf{x}, t) = \begin{cases} 1 & \text{if } i \text{ link occupied} \\ 0 & \text{if } i \text{ link empty.} \end{cases}$$

  This is referred as the exclusion principle.

- After the streaming step, all the particles arriving at a site collide.
- The collision rules are shown in Figure 2.2. These will be described for the FHP model in the Section 2.4.3. Collisions occur such that particle mass and momentum are conserved.

The density (mass) and momentum at each site is found as

$$\rho(\mathbf{x}, t) = \sum_i f_i(\mathbf{x}, t) \text{ and } \rho(\mathbf{x}, t)\mathbf{u}(\mathbf{x}, t) = \sum_i f_i(\mathbf{x}, t)\mathbf{e}_i \tag{2.18}$$

2.4.3 FHP collisions

The collision rules are shown in the Figure 2.2, where the particles on links $1-6$ are represented by outgoing arrows both before and after the collisions. A rest particle is represented by an open circle.

- The first case represents 2-particle head-on collisions, (mass= 2, momentum= 0). The two particles arrive on $\mathbf{e}_1$ and $\mathbf{e}_4$, move off either along $\mathbf{e}_2$ and $\mathbf{e}_5$ or $\mathbf{e}_3$ and $\mathbf{e}_6$. Both of the two collision outcomes conserve mass and momentum, they are selected randomly with probability 0.5. Two alternative head on collisions result from rotating the grid through $\pm 60^o$.

- In the second case, a 3-particles symmetric collision takes place where the total momentum is zero: here the particles move onto the unoccupied links. The inverse of this collision is also possible.

- In the third case, a rest particle is either created or removed. There are six rotational variations of these collisions.

- The fourth case can be thought as the 2-particle head-on collisions with 2 additional particles which do not take place in the collision. Again, alternative configurations are possible by rotating by $\pm 60^o$.

Combining the streaming and collision gives the LGA equation:

$$n_i\left(\mathbf{x}+\mathbf{e}_i, t+1\right) - n_i\left(\mathbf{x}, t\right) = \Delta_i\left(\mathbf{x}, t\right), \tag{2.19}$$

where the collision operator Δ_i is:

$$\Delta_i = \begin{cases} -1 & \text{particle removed} \\ 0 & \text{no change} \\ 1 & \text{particle added,} \end{cases}$$

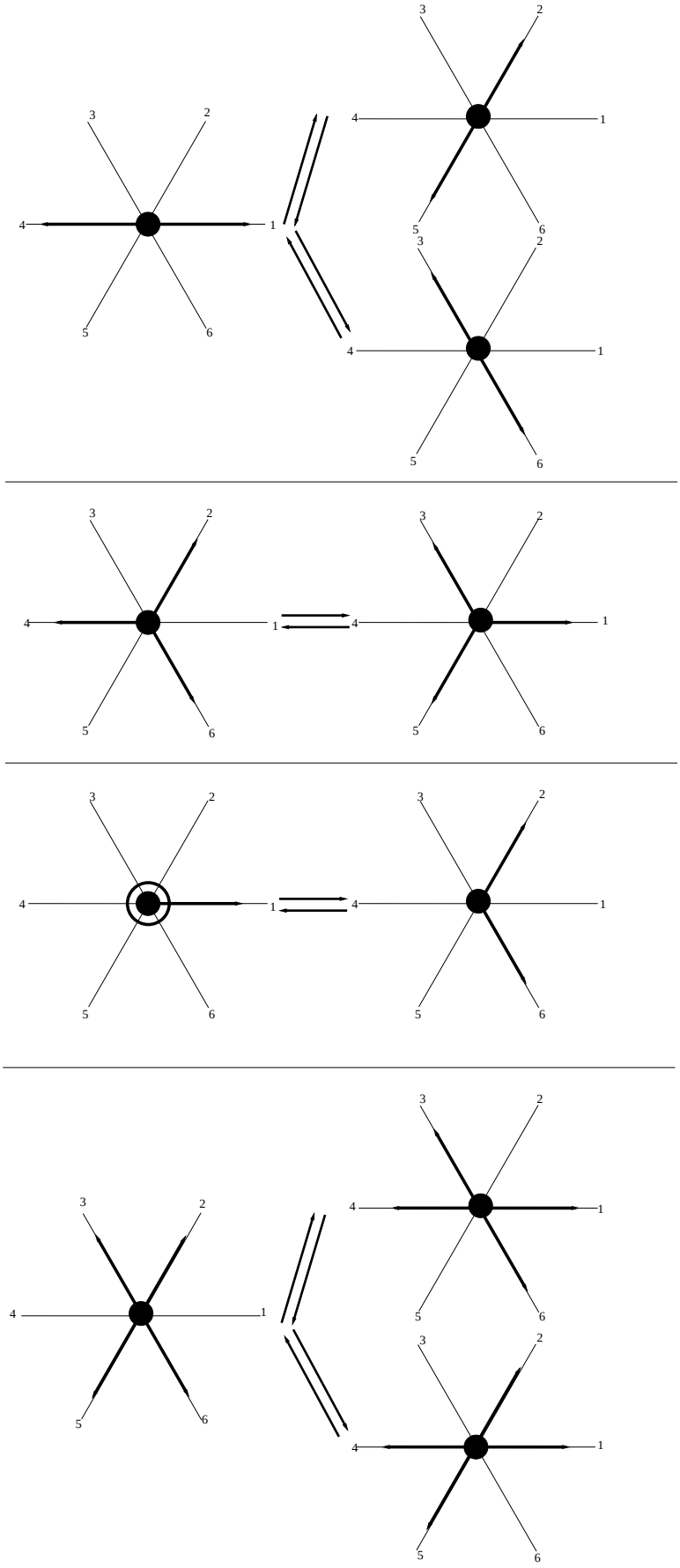

Figure 2.2: FHP collisions, inspired from Wolfram [52]

that is, in the Figure 2.2, for the 'rest particle collision' $\Delta_3 = \Delta_4 = \Delta_5 = 0$, $\Delta_2 = \Delta_6 = 1$ and $\Delta_0 = \Delta_1 = -1$. The mass and momentum at the site are conserved.

2.5 From the Lattice Gas Automaton to the Lattice Boltzmann Method

Although the LGA has been widely used, it has a number of disadvantages. One significant problem is that simulations with LGA automaton tend to be very noisy [68, 69] due to the small number of particles at each site. This is overcome to some extent by calculating density, momentum, and velocity by averaging over a larger region. The results of such averaging can still be noisy and frequently [68,69] very larger averaging cells are used, and/or ensemble averaging, to reduce the statistical noise further.

To suppress the statistical noise, McNamara and Zanetti in 1988 [70], introduced the Lattice Boltzmann Method, as an independent numerical regime for hydrodynamic simulations. The Boolean variables of the LGA are replaced with continuous distributions, f_i in the LBM. The BGK operator $-\frac{1}{\tau}\left(f - f^{(eq)}\right)$, [71–73] replaces the collision operator used in the LGA. This gives the Lattice BGK (LBGK) Boltzmann equation

$$f_i\left(\mathbf{x} + \mathbf{e}_i, t+1\right) - f_i\left(\mathbf{x}, t\right) = -\frac{1}{\tau}\left(f_i - f_i^{(eq)}\right). \tag{2.20}$$

The form of the equilibrium distribution function $f_i^{(eq)}$ is dependent on the grid used in the simulation. Its form will be considered in Section 2.6.2. The density ρ and the velocity $\mathbf{u}$ are found from $f_i\left(\mathbf{x}, t\right)$ following the continuous Boltzmann

equation and the LGA as:

$$\rho\left(\mathbf{x},t\right)=\sum_{i}f_{i}\left(\mathbf{x},t\right), \tag{2.21}$$

and

$$\rho\left(\mathbf{x},t\right)\mathbf{u}\left(\mathbf{x},t\right)=\sum_{i}\mathbf{e}_{i}f_{i}\left(\mathbf{x},t\right). \tag{2.22}$$

2.6 $\mathbf{D_2Q_9}$ lattice

In LBGK models, the Boltzmann equation is solved on a regular lattice, depicted as D_nQ_m, [74], with n the number of the dimensions and m the number of the links including 'rest particles'. The most commonly used 2-D LBGK model is the D_2Q_9 [33, 52, 75–80],

2.6.1 Lattice symmetries

Not all lattice types are adequate for the execution of a Lattice Boltzmann simulation [81]. In order for the simulation to yield the desired asymptotic partial differential equations, the lattice must verify a set of symmetry conditions. The LBGK model requires that for a set of constants W_i and c_s, the link values satisfy [81]:

$$\begin{aligned}
&\textstyle\sum_i W_i = 1\\
&\textstyle\sum_i W_i e_{i\alpha} = 0\\
&\textstyle\sum_i W_i e_{i\alpha} e_{i\beta} = c_s^2\delta_{\alpha\beta}\\
&\textstyle\sum_i W_i e_{i\alpha} e_{i\beta} e_{i\gamma} = 0\\
&\textstyle\sum_i W_i e_{i\alpha} e_{i\beta} e_{i\gamma} e_{i\delta} = c_s^4\left(\delta_{\alpha\beta}\delta_{\gamma\delta}+\delta_{\alpha\gamma}\delta_{\beta\delta}+\delta_{\alpha\delta}\delta_{\beta\gamma}\right)\\
&\textstyle\sum_i W_i e_{i\alpha} e_{i\beta} e_{i\gamma} e_{i\delta} e_{i\epsilon} = 0,
\end{aligned} \tag{2.23}$$

where $\delta_{\alpha\beta}$ is the Kronecker delta:

$$\delta_{\alpha\beta} = \begin{cases} 1 & \alpha = \beta \\ 0 & \alpha \neq \beta \end{cases}$$

The D_2Q_9 satisfies the symmetry conditions [81]. The D_2Q_9 lattice is a 2-D lattice with nine nodes, as shown firstly in Figure 2.3. The $\mathbf{e}_i$ are given by:

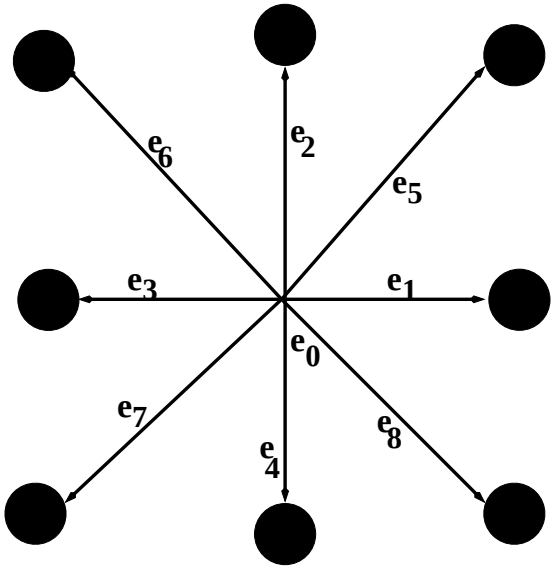

Figure 2.3: The D_2Q_9 lattice

$$\mathbf{e}_i = \left\{ \begin{array}{ll} (0,0) & \text{for } i = 0 \\ \left(\cos\left(\frac{\pi}{2}(i-1)\right), \sin\left(\frac{\pi}{2}(i-1)\right)\right) & \text{for } i = 1,\, 2,\, 3,\, 4 \\ \left(\cos\left(\frac{\pi}{2}(i-\frac{9}{2})\right), \sin\left(\frac{\pi}{2}(i-\frac{9}{2})\right)\right) & \text{for } i = 5,\, 6,\, 7,\, 8, \end{array} \right\} \tag{2.24}$$

For 'vanishing velocities', [52], a global equilibrium distribution W_i for the fluid at rest can be defined. In the vicinity of the equilibrium state, the distribution functions can be expressed as:

$$f_i(\mathbf{x}, t) = W_i + f_i^{(neq)}(\mathbf{x}, t), \tag{2.25}$$

with $|f_i^{(neq)}(\mathbf{x},t)| << W_i$. The W_i have to be positive to ensure positive density. These are chosen to be represented by Maxwell distributions. The lattice velocity moments up to the fourth order over the W_i are set identical to the respective velocity moments over the Maxwell distribution, see equation (2.7):

$$w_B(\mathbf{u}) = \left(\frac{m}{2\pi k_B T}\right) \exp\left(\frac{-m\mathbf{u}^2}{2k_B T}\right), \tag{2.26}$$

with m the mass particle and $\mathbf{u}$ the particle velocity. The odd moments vanish [52]:

$$\sum_i W_i e_{i\alpha} = 0, \tag{2.27}$$

$$\sum_i W_i e_{i\alpha} e_{i\beta} e_{i\gamma} = 0. \tag{2.28}$$

The even moments, [52],read:

$$\sum_i W_i = \int w_B(u) d\mathbf{u} = 1, \tag{2.29}$$

$$\sum_i W_i e_{i\alpha} e_{i\beta} = \int w_B(u) u_\alpha u_\beta d\mathbf{u} = \frac{k_B T}{m} \delta_{\alpha\beta}. \tag{2.30}$$

and

$$\sum_i W_i e_{i\alpha} e_{i\beta} e_{i\gamma} e_{i\delta} = \int w_B(u) u_\alpha u_\beta u_\gamma u_\delta d\mathbf{u} = \frac{k_B T}{m} (\delta_{\alpha\beta}\delta_{\gamma\delta} + \delta_{\alpha\gamma}\delta_{\beta\delta} + \delta_{\alpha\delta}\delta_{\beta\gamma}), \tag{2.31}$$

which can be formed using [82] and

$$\int_0^\infty x^{2n} \exp\left(-ax^2\right) = \frac{(2n-1))!!}{2^{n+1}a^n} \sqrt{\frac{\pi}{a}} \tag{2.32}$$

2.6.2 Distribution functions for the D2Q9

Due to symmetry, W_i for directions with identical speeds are the same [52] and are given by the values in Table 2.1. Evaluating equations (2.29), (2.30), (2.31),

i	e_i^2	W_i
0	0	W_A
1-4	1	W_B
5-8	2	W_C

Table 2.1: Velocities, i and W_i for the D_2Q_9 lattice

we get:

- for the 0^{th} moment, using equation. (2.29):

$$\sum_i W_i = W_A + 4W_B + 4W_C = 1, \tag{2.33}$$

- for the second moment, using equation (2.30):

$$\sum_i e_{i1}^2 W_i = 2W_B + 4W_C = \frac{k_B T}{m}, \tag{2.34}$$

- for the fourth moment,

$$\sum_i e_{i1}^4 W_i = 2W_B + 4W_C = \frac{k_B T}{m}. \tag{2.35}$$

These have solutions: $W_A = \frac{4}{9}$, $W_B = \frac{1}{9}$, $W_C = \frac{1}{36}$, where $\frac{k_B T}{m} = \frac{c_s^2}{3}$ and $c_s = \frac{1}{\sqrt{3}}$, which will later be identified as the speed of sound in equation (2.56). For non-vanishing velocities, it can be shown that the equilibrium distribution functions can be defined as [83]:

$$f_i^{(eq)}(\rho, \mathbf{u}) = W_i \left\{ \rho + \frac{m}{k_B T} \rho \mathbf{e}_i \cdot \mathbf{u} + \frac{m}{2\rho k_B T} \left[\frac{m}{k_B T} (\mathbf{e}_i \rho \cdot \mathbf{u})^2 - \rho^2 \mathbf{u}^2 \right] \right\}. \tag{2.36}$$

Thus:

$$f_i^{(eq)} = \begin{cases} \dfrac{4\rho}{9}\left(1 - \dfrac{3}{2}\dfrac{\mathbf{u}^2}{c_s^2}\right), \text{ if } i = 0, \\ \dfrac{\rho}{9}\left[1 + 3\dfrac{\mathbf{e}_i \cdot \mathbf{u}}{c_s^2} + \dfrac{9}{2}\dfrac{(\mathbf{e}_i \cdot \mathbf{u})^2}{c_s^4} - \dfrac{3}{2}\dfrac{\mathbf{u}^2}{c_s^2}\right], \text{ if } i = 1, 2, 3, 4, \\ \dfrac{\rho}{36}\left[1 + 3\dfrac{\mathbf{e}_i \cdot \mathbf{u}}{c_s^2} + \dfrac{9}{2}\dfrac{(\mathbf{e}_i \cdot \mathbf{u})^2}{c_s^4} - \dfrac{3}{2}\dfrac{\mathbf{u}^2}{c_s^2}\right], \text{ if } i = 5, 6, 7, 8, \end{cases} \tag{2.37}$$

is the equilibrium distribution function for the D2Q9 lattice.

2.7 Chapman Enskog expansion

The Champman Enskog expansion was applied by Frisch *et al.* [67] to the LGA to demonstrate that it satisfied the Navier-Stokes equation. The same approach is applied here to the LBM with a D2Q9 grid. The derivation is based on that of Chen and Doolen [84]. Taking the Taylor expansion of the left-hand-side of equation (2.20) with respect to $\mathbf{x}$ and t, we find that to second order in the small expansion parameter ϵ:

$$\frac{\partial f_i}{\partial t} + \mathbf{e}_i \cdot \nabla f_i + \epsilon\left(\frac{1}{2}\left(\mathbf{e}_i \cdot \nabla\right)^2 f_i + \mathbf{e}_i \cdot \nabla\frac{\partial f_i}{\partial t} + \frac{1}{2}\frac{\partial^2 f_i}{\partial t^2}\right). \tag{2.38}$$

We assume that f_i can be expanded formally around $f_i^{(eq)}$ in the following manner:

$$f_i = f_i^{(eq)} + \epsilon f_i^{(neq)} \tag{2.39}$$

with $f_i^{(neq)}$ the non-equilibrium distribution function, expanded as:

$$f_i^{(neq)} = f_i^{(1)} + \epsilon f_i^{(2)} + O\left(\epsilon^2\right), \tag{2.40}$$

satisfying the constraints

$$\sum_i f_i^{(k)} = 0, \qquad \sum_i \mathbf{e}_i f_i^{(k)} = 0 \qquad (k = 1, 2)\,. \tag{2.41}$$

Two time and one spatial scale are introduced [24]:

$$\frac{\partial}{\partial t} = \epsilon \frac{\partial}{\partial t_1} + \epsilon^2 \frac{\partial}{\partial t_2}, \qquad \frac{\partial}{\partial x} = \epsilon \frac{\partial}{\partial x_1}. \tag{2.42}$$

The right-hand-side of equation (2.20) can then be written:

$$-\frac{1}{\tau}\left(f_i^{(1)} + \epsilon f_i^{(2)}\right). \tag{2.43}$$

Substituting equations (2.42), (2.39) and (2.40) into equation (2.38) combined with equation (2.43), and separating the orders of ϵ we get:

$$\frac{\partial f_i^{(eq)}}{\partial t_1} + \mathbf{e}_i \cdot \nabla_1 f_i^{(eq)} = -\frac{f_i^{(1)}}{\tau}, \tag{2.44}$$

and

$$\begin{aligned} \frac{\partial f_i^{(eq)}}{\partial t_2} + \left(\frac{\partial f_i^{(1)}}{\partial t_1} + \mathbf{e}_i \nabla_1 f_i^{(1)}\right) + \frac{1}{2}\frac{\partial}{\partial t_1}\left(\frac{\partial f_i^{(eq)}}{\partial t_1} + \mathbf{e}_i \cdot \nabla_1 f_i^{(eq)}\right) \\ + \frac{1}{2}\left(\mathbf{e}_i \cdot \nabla_1\right)\left(\frac{\partial f_i^{(eq)}}{\partial t_1}\left(\mathbf{e}_i \cdot \nabla_1\right) f_i^{(eq)}\right) = -\frac{f_i^{(2)}}{\tau}. \end{aligned} \tag{2.45}$$

Substituting equation (2.44) into equation (2.45), we find:

$$\frac{\partial f_i^{(eq)}}{\partial t_2} + \left(1 - \frac{1}{2\tau}\right)\left[\frac{\partial f_i^{(1)}}{\partial t_1} + \mathbf{e}_i \cdot \nabla_1 f_i^{(1)}\right] = -\frac{f_i^{(2)}}{\tau}. \tag{2.46}$$

Summing equation (2.44) over i and using equations (2.18) and (2.41) we find:

$$\frac{\partial \rho}{\partial t_1} + \nabla_1 \cdot \rho \mathbf{u} = 0, \tag{2.47}$$

if we also multiply equation (2.44) by $\mathbf{e}_i$ and sum over i we find:

$$\frac{\partial \rho u_\alpha}{\partial t_1} + \nabla_\beta \Pi^{(0)}_{\alpha\beta} = 0, \tag{2.48}$$

where

$$\Pi^{(0)}_{\alpha\beta} = \sum_i f_i^{(eq)} e_{i\alpha} e_{i\beta} \tag{2.49}$$

is the momentum flux tensor to the first order approximation [52]. Similarly, summing over i in equation (2.45) gives:

$$\frac{\partial \rho}{\partial t_2} = 0. \tag{2.50}$$

Multiplying equation (2.45) by $\mathbf{e}_i$ and summing over i:

$$\frac{\partial \rho u_\alpha}{\partial t} + \nabla_\beta \cdot \left(1 - \frac{1}{2\tau}\right) \Pi^{(1)}_{\alpha\beta} = 0, \tag{2.51}$$

where

$$\Pi^{(1)}_{\alpha\beta} = \sum_i f_i^{(1)} e_{i\alpha} e_{i\beta} \tag{2.52}$$

is the second order approximation of the momentum flux tensor [52]. Using equation (2.36) we can express (2.49) and (2.52) generally as, [85]:

$$\Pi^{(0)}_{\alpha\beta} = \rho c_s^2 \delta_{\alpha\beta} + \rho u_\alpha u_\beta, \tag{2.53}$$

and

$$\Pi^{(1)}_{\alpha\beta} = \rho\tau \left[-c_s^2 \left(\nabla_\beta u_\alpha + \nabla_\alpha u_\beta\right)\right]. \tag{2.54}$$

Combining equations (2.48) and (2.51) and using equations (2.53) and (2.54), we recover the Navier-Stokes equation [24]:

$$\frac{\partial u_\alpha}{\partial t} + \nabla_\beta u_\alpha u_\beta = -\frac{\nabla_\alpha p}{\rho} + \nu \nabla_\beta \left(\nabla_\alpha \rho u_\beta + \nabla_\beta \rho u_\alpha\right), \tag{2.55}$$

where the pressure p, is given by [52]:

$$p = \frac{k_B T}{m}\rho = \frac{c_s^2}{3}\rho, \tag{2.56}$$

and the kinematic viscosity [24, 52], $\nu = \dfrac{2\tau - 1}{6}$. Equation (2.56) is an equation of state where c_s is the speed of sound. The shear stress can be determined in the LBM directly from the distribution functions. The derivation shown here follow closely than in [85]. For a viscous fluid, this affects fluid motion. Dissipation energy is associated with the momentum flux tensor $\Pi_{\alpha\beta}$, which is symmetric, $\Pi_{\alpha\beta} = \Pi_{\beta\alpha}$. This tensor gives the α^{th} component of the amount of momentum flowing in unit time through unit area perpendicular to the x_β- axis. The momentum flux tensor is given by

$$\Pi_{\alpha\beta} = \rho u_\alpha u_\beta - \sigma_{\alpha\beta} \tag{2.57}$$

where

$$\sigma_{\alpha\beta} = -p\delta_{\alpha\beta} + \nu\left(\nabla_\beta u_\alpha + \nabla_\alpha u_\beta\right) = -p\delta_{\alpha\beta} + 2\nu\rho S_{\alpha\beta}, \tag{2.58}$$

is the stress tensor for an incompressible fluid.

$$S_{\alpha\beta} = \frac{1}{2}\left(\partial_\beta u_\alpha + \partial_\alpha u_\beta\right), \tag{2.59}$$

is the strain rate tensor. Thus, equation (2.54) becomes:

$$S_{\alpha\beta} = -\frac{1}{2\rho\tau c_s^2}\Pi^{(1)}_{\alpha\beta}. \tag{2.60}$$

Substituting $\nu = \dfrac{2\tau - 1}{6}$ in equations (2.60), (2.56) into equation (2.58) and using equation (2.52), we write the stress tensor:

$$\begin{aligned} \sigma_{\alpha\beta} &= -\rho c_s^2 \delta_{\alpha\beta} - \left(1 - \frac{1}{2\tau}\right) \Pi_{\alpha\beta}^{(1)} \\ &= -\rho c_s^2 \delta_{\alpha\beta} - \left(1 - \frac{1}{2\tau}\right) \sum_i f_i^{(1)} e_{i\alpha} e_{i\beta}. \end{aligned} \tag{2.61}$$

Thus, the shear stress can be calculated locally at each site.

2.8 Application of the LBM algorithm

The LBM is implemented in the following steps.

1. Initialising the system for given initial values of $\rho(\mathbf{x})$ and $\mathbf{u}(\mathbf{x})$ by assigning $f_i = f_i^{(eq)}$ through equation (2.37).

2. Streaming the distribution function according to $f_i'(\mathbf{x} + \mathbf{e}_i, t+1) = f_i(\mathbf{x}, t)$.

3. Calculating ρ and $\mathbf{u}$ from equations (2.21) and (2.22), respectively, using the new distribution function f'.

4. Computing $f_i^{(eq)}$ through equation (2.37).

5. Performing the collision according to $f_i(\mathbf{x}, t) = f_i'(\mathbf{x}, t) + f_i^{(eq)}(\mathbf{x}, t)$.

6. Repeating from step (2).

2.9 Boundary conditions

When applying the scheme set out in Section 2.8, the streaming step. step 2, relies on the distribution functions being available at the neighbouring sites. When these are not available, they must be determined by applying an appropriate

boundary condition. The modelling of the boundary condition in the LBM is crucial because it determines the overall accuracy and stability of the method [86, 87]. A boundary can be introduced to an LBM by picking the grid sites where the boundary is to be set and streaming the fluid in a different manner at these sites. The commonly used boundary scheme for modelling no-slip boundary conditions is the half-way bounceback scheme [88, 89], however more complex boundary conditions such as the extrapolation scheme [77] used here have been developed to deal with more complex geometries.

2.9.1 Bounceback scheme

The most commonly used LBM non-slip boundary condition is the bounceback scheme. This is the case encountered when a fluid particle meeting a wall rebounds in the opposite direction. That is, when a distribution function in link $\mathbf{e}_i$ encounters a wall during the streaming stage, it reflects and returns to the original site along link $-\mathbf{e}_i$. Averaging the velocity of the distribution functions before and after the collision, we get:

$$\langle \mathbf{u} \rangle = 0. \tag{2.62}$$

This original bounceback scheme is only first order [88].

2.9.2 Half-way bounceback scheme

If the wall boundary is placed half way between a boundary site and an adjacent fluid site, the bounceback scheme is referred to as half-way bounceback scheme, as shown in Figure 2.4 [21, 87]. A distribution function streaming from the fluid site (A) towards the boundary is reflected back to site (A) [21]. The half-way bounceback scheme is generally credited with second order accuracy in simple geometries where the boundary is parallel to the link directions [21, 87]. Hence,

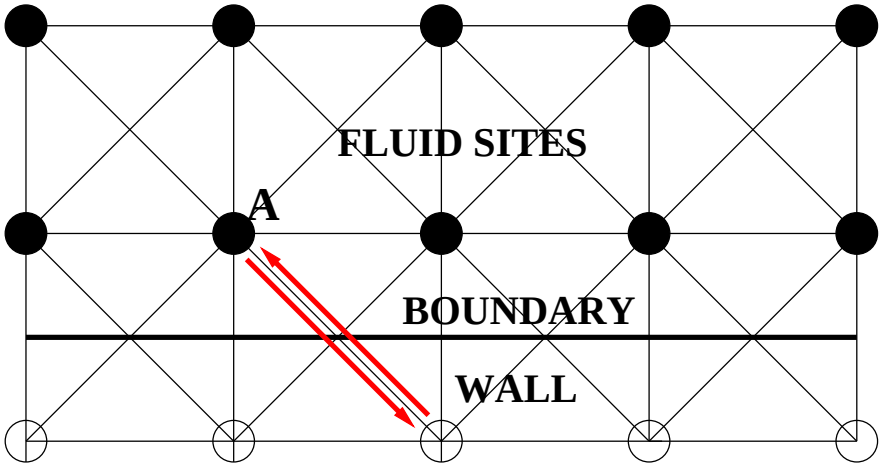

Figure 2.4: The half-way bounceback scheme

this is preferable to the bounceback scheme.

2.9.3 Extrapolation scheme

A number of boundary regimes have been proposed [77, 90–92]. These methods seek to enhance the accuracy of boundary schemes and also find methods of modelling more complicated wall geometries. Although the half-way bounceback scheme provides second order accuracy in planar geometries, its accuracy is reduced to first order when more complicated curved boundaries are considered. These additional errors are imposed partially because the half-way bounceback scheme requires the boundary sites to be placed halfway between the fluid sites and the wall sites, parallel to lattice links. However, this is unfeasible for a curved wall as it requires a staircase of straight lines, such as the dotted line, shown in Figure 2.5.

2.9.3.1 Extrapolation boundary scheme

The extrapolation scheme [77] seeks to overcome the deficits of the half-way bounceback scheme by approximating the position of the boundary more precisely and calculating the distribution functions which reflect from it. The underlying

idea of Guo [77] is documented in Figure 2.5, where the fluid sites (filled circles) and the boundary sites (empty circles) are separated by the curved boundary, represented by the solid line. The squares represented by the wall points where the curved boundary intersects the lattice links. We will consider the boundary condition at site $\mathbf{x}_f$, for the distribution function which is incoming along the link which intersects the boundary at $\mathbf{x}_b$. The distribution function is split into two parts; an equilibrium and a non-equilibrium part. We are required to compute a fictitious distribution function $f_5'(\mathbf{x}_w)$. The non-equilibrium part is approximated by that of the neighbouring fluid site ($\mathbf{x}_f$ or $\mathbf{x}_{ff} = \mathbf{x}_f + \mathbf{e}_5$) and the equilibrium part is determined from a fictitious density and velocity $\rho_w'(\mathbf{x}_w)$ and $\mathbf{u}_w'(\mathbf{x}_w)$. The density is approximated by $\rho_w'(\mathbf{x}_w) = \rho(\mathbf{x}_f)$ and $\mathbf{u}_w'$ is determined

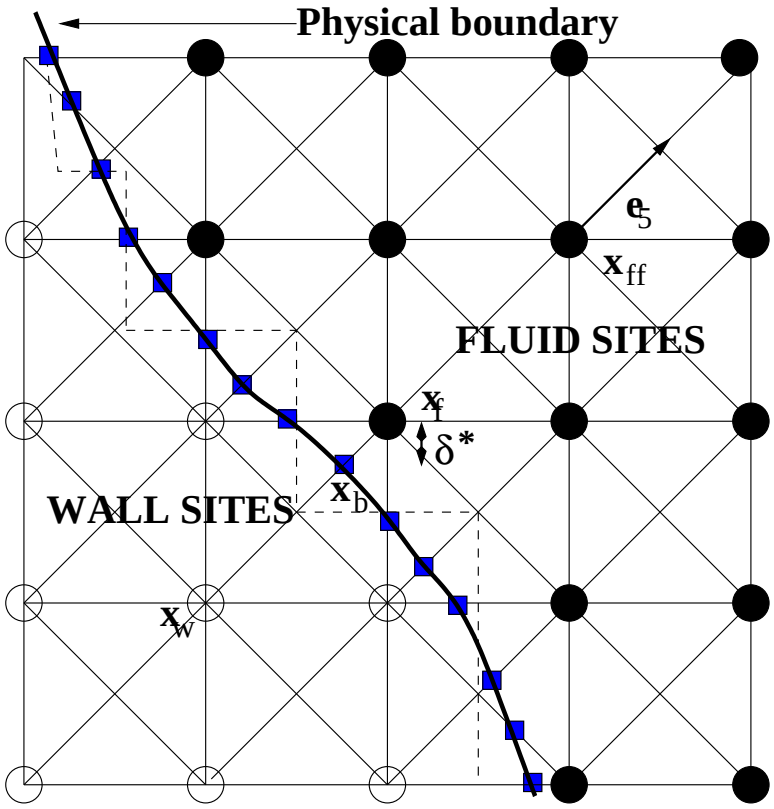

Figure 2.5: The extrapolation scheme. The fluid sites are shown as filled circles and the wall sites as open circles. They are separated by a physical boundary represented by the solid line. The dashed line represents the staircase boundary applied by the half-way bounce back scheme. Also shown are the sites $\mathbf{x}_f$,$\mathbf{x}_w$ and $\mathbf{x}_{ff}$ which are sued in the extrapolation boundary scheme; and the normalised distance δ^*.

by extrapolation based on the known boundary velocity, $\mathbf{u}_b = \mathbf{u}(\mathbf{x}_b) = 0$ and the known velocities of $\mathbf{u}_f = \mathbf{u}(\mathbf{x}_f)$ and $\mathbf{u}_{ff} = \mathbf{u}(\mathbf{x}_{ff})$. Two approximations are quantified [77] by either:

$$\mathbf{u}'_{w1} = \frac{(\mathbf{u}_b + (\delta^* - 1)\,\mathbf{u}_f)}{\delta^*}, \tag{2.63}$$

or

$$\mathbf{u}'_{w2} = \frac{(2\mathbf{u}_b + (\delta^* - 1)\,\mathbf{u}_{ff})}{1 + \delta^*}, \tag{2.64}$$

where δ^* is the normalised fraction of the intersected link, still in the fluid, [77]:

$$\delta^* = \frac{(|\mathbf{x}_f - \mathbf{x}_b|)}{(|\mathbf{x}_f - \mathbf{x}_w|)}. \tag{2.65}$$

It is usually more accurate to use $\mathbf{u}'_{w1}$ than $\mathbf{u}'_{w2}$ to approximate $\mathbf{u}'_w$. However if δ^* is small, then numerical instability may result [77], so we select $\mathbf{u}'_w = \mathbf{u}'_{w1}$ for $\delta^* \geq 0.75$, and $\mathbf{u}'_w = \delta^*\mathbf{u}'_{w1} + (1 - \delta^*)\,\mathbf{u}'_{w2}$, for $\delta^* < 0.75$. Similarly, to $\mathbf{u}'_w$, the distribution functions are formulated as:

$$f_i^{(neq)}(\mathbf{x}_w) = f_i^{(neq)}(\mathbf{x}_f), \quad \text{if } \delta^* \geq 0.75 \tag{2.66}$$

and

$$f_i^{(neq)}(\mathbf{x}_w) = \delta^* f_i^{(neq)}(\mathbf{x}_f) + (1 - \delta^*)\, f_i^{(neq)}(\mathbf{x}_{ff}), \quad \text{if } \delta^* < 0.75\ . \tag{2.67}$$

Then, the required expression for $f_i(\mathbf{x}_w, t)$ is:

$$f_i(\mathbf{x}_w) = f_i^{(eq)}(\mathbf{x}_w) + \left(1 - \frac{1}{\tau}\right) f_i^{(neq)}(\mathbf{x}_w), \tag{2.68}$$

with $f_i^{(eq)}(\mathbf{x}_w, t)$ calculated from equation (2.37) with $\rho = \rho'_w$ and $\mathbf{u} = \mathbf{u}'_w$.

2.9.3.2 Inflow and outflow boundary conditions

The velocity waveform seen in Figure 3.2 was implemented at the base of this geometry by setting the incoming distribution functions to their equilibrium values, given by equation (2.37) when $\rho = 1$ and $\mathbf{x}$ is the velocity shown in Figure 3.2. This profile was applied uniformly across the base of the artery at each position of the cycle except for a boundary layer of approximately 1mm, over which the profile was linearly reduced so that there was zero velocity at the wall of the artery.

At the outflow boundary, the unknown distribution functions were found from the following linear extrapolation based on the work by Neal [93], as given:

$$f_i\left(\mathbf{x}, t+1\right) = 2f_i\left(\mathbf{x}+\mathbf{e}_i, t+1\right) - f_i\left(\mathbf{x}+2\mathbf{e}_i, t+1\right). \tag{2.69}$$

This boundary condition ensures that a pre-determined velocity is not forced on the outflow, thus enabling the mass fraction exiting from the ICA and ECA to the dependent on the artery geometry and flow conditions, in a similar way to be constant pressure outflow condition.

Chapter 3

LBM simulation of the carotid artery

3.1 Carotid artery geometry

Figure 3.1 shows the model of the carotid geometry used here. It has been, used previously in [78, 94]. The carotid artery geometry is complex, consisting of irregular walls, changing vessel diameter and a bifurcation. The three main regions of the carotid artery near the bifurcation are the Internal Carotid Artery (ICA), External Carotid Artery (ECA) and Common Carotid Artery (CCA), as shown in Figure 3.1. The box in Figure 3.1 highlights the region of interest around the bifurcation which is known to be susceptible to atheroslerosis [3–8, 11, 95, 96] and where the results will be presented. This region is sufficiently far from the inlet and outlet boundaries so as to avoid any effects caused by the method of applying these boundary conditions. No-slip boundary conditions were implemented at the geometry wall using the extrapolation scheme, discussed previously in Section 2.9.3.

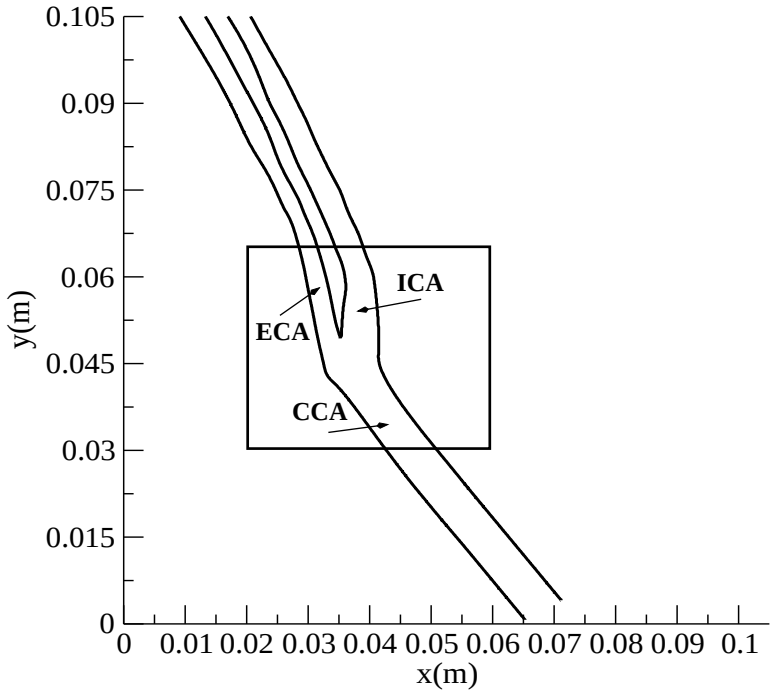

Figure 3.1: Carotid artery geometry. The entire carotid artery geometry. Regions corresponding to the ICA, ECA and CCA are indicated. The box indicates the region of interest around the bifurcation where results will be presented.

3.2 Pulsatile flow

The velocity waveform used to drive the blood flow in the carotid artery is displayed in Figure 3.2, in terms of the period, T. This waveform was adapted from Holdsworth *et al.* [97]. The velocity waveform, seen in Figure 3.2 was implemented at the base of the geometry. The complicated shape was implemented by decomposing the pulse shape into harmonic components using the Fourier decomposition. For simulations of an arterial pulse, it is held that 5-10 harmonics will generally suffice to describe the pulse accurately [98]. A decomposition of 31 harmonics was used for greater accuracy as in [78, 94]. It was shown in [94] that small variations in the inlet parameters, such as the width of the boundary layer did not significantly affect the results.

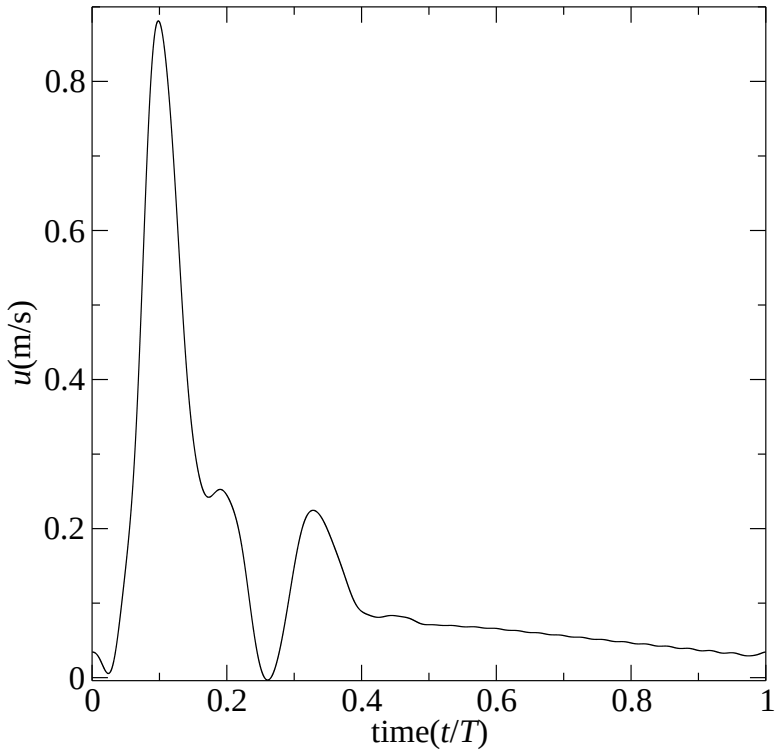

Figure 3.2: Carotid artery velocity waveform, obtained from Holdsworth et al. [97].

3.3 Simulation convergence

The blood flow simulations were performed in a box of size 401 by 697 lattice units (lu), using the velocity pulse shown in Figure 3.2 and the extrapolation scheme (Section 2.9.3). After initialising the model was run over seven periods to achieve convergence. This is shown in Figure 3.3 for a Newtonian simulation where:

$$L(t) = \left| \frac{\mathbf{x}^{max}\mathbf{u}(\mathbf{x},(T+t))\text{-}\mathbf{x}^{max}\mathbf{u}(\mathbf{x},t)}{\mathbf{x}^{max}\mathbf{u}(\mathbf{x},t)} \right|, \tag{3.1}$$

is the normalised maximum absolute difference between the velocity $\mathbf{u}(\mathbf{x},t)$ and the one at the same site one period later $\mathbf{u}(\mathbf{x},(t+T))$. The results show that $L(t)$ converges to $< 10^{-3}$ after 7 periods.

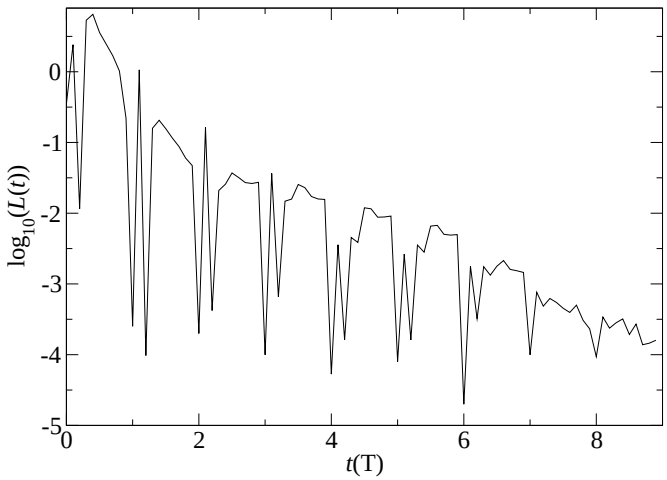

Figure 3.3: Convergence of LBM simulation

3.4 Non Newtonian simulations using the Carreau-Yasuda Model

For a Newtonian fluid the shear viscosity η is constant and is related to the relaxation time τ through equation:

$$\eta = \rho \frac{2\tau - 1}{6}. \tag{3.2}$$

The shear-thinning nature of blood can be mimicked using the Carreau-Yasuda (C-Y) model [99–102] :

$$\eta\left(\dot{\gamma}\right) = \eta_{\infty} + \left(\eta_0 - \eta_{\infty}\right)\left(1 + \left(\lambda\dot{\gamma}^{a}\right)^{\frac{n-1}{a}}\right), \tag{3.3}$$

where $\dot{\gamma}$ is the shear rate, and α, n and λ are empirically determined constant parameters, [103]. The parameters α and n are dimensionless, but λ has units of time. The C-Y model is continuous for all $\dot{\gamma} \geq 0$. η_0 and η_{∞} are limiting values of the viscosity in the lowest and highest shear rate cases, respectively. The shear

rate is defined as:

$$\dot{\gamma} = 2\sqrt{D_{II}}, \tag{3.4}$$

where D_{II} is the second invariant of the strain rate tensor [103]:

$$D_{II} = \sum_{\alpha,\beta} S_{\alpha\beta} S_{\alpha\beta}. \tag{3.5}$$

For the LBM, $S_{\alpha\beta}$ can be found directly from the non-equilibrium distribution function through equation (2.37).

3.5 Set-up of the simulation

We describe here the initiation of the LBM simulation and its parameters as well as the assumptions made in our simulations. Following [33, 43, 78–80, 104–107] our simulations are run in 2-D to capture the mean features of the flow. Mainly, Newtonian simulations are considered, however, non-Newtonian modelling is considered in some cases using the C-Y model. The artery walls are assumed rigid [43, 78]. This is a good approximation in the stenosed region, and for the point of view of this work provides sufficient accuracy in the stenosed region to develop and evaluate the numerical model. Oscillatory flow was presumed to approximate the behaviour of arterial blood flow. No slip boundary condition, using the second-order accurate extrapolation scheme, is applied at the walls.

3.6 Model parameters

In the following, variables labelled with a subscript 'A' refer to that variable in physical SI units, variables labelled with a subscript 'B' refer to that variable in

LBM (lattice) units. Re_δ is determined by:

$$Re_\delta = \frac{\rho U \delta}{\nu} \tag{3.6}$$

where $\rho = 1$, δ is the Stokes layer thickness, used in [108, 109] is expressed:

$$\delta = \sqrt{\frac{\nu T}{\pi}}, \tag{3.7}$$

with T the period. The Womersley parameter, α, defined by equation (1.5), can be expressed as:

$$\alpha = \frac{D}{2}\sqrt{\frac{2\pi}{T\nu}}. \tag{3.8}$$

Parameter	Artery	Boltzmann(lu)
u_0	1.07 ms^{-1}	0.08152
D	6.4×10^{-3} m	36
$\eta = \eta_\infty$	3.5×10^{-6} Pa . s	0.001104
T	0.16744 s	66987
α	4.5	4.5
Re_δ	307	307

Table 3.1: Carotid artery parameters, based on Holdsworth *et al.* [97] and equivalent Boltzmann scaled parameters.

Table 3.1 shows the SI parameters selected to describe the artery, along with the Boltzmann parameters based on an artery diameter of 36 lu. These parameters preserve Re and α between the model and the artery. For non-Newtonian simulations the C-Y model parameters, based on [110] are shown in Table 3.2, along with their Boltzmann equivalents. We can rearrange equation (3.7) to find the peak simulated velocity U_{0B} as:

$$U_{0B} = Re_\delta \sqrt{\frac{\eta_B \pi}{T_B}}, \tag{3.9}$$

Parameter	SI	Boltzmann(lu)
η_0	2.17×10^{-4} Pa . s	0.068364
η_∞	3.5×10^{-6} Pa . s	0.0015
λ	1.5 s^{-1}	603619
a	0.64	0.64
n	0.2128	0.2128

Table 3.2: C-Y model parameters from Abraham et al. [110] and equivalent Boltzmann scaled parameters.

where $\rho_B = 1$. Also from equation (3.8):

$$T_B = \frac{2\pi}{\eta_B}\left(\frac{D_B}{2a}\right)^2, \tag{3.10}$$

for fixed values of Re and α, and D_B, the suitable values of U_B was selected. Matching Reynold's numbers we can find η_B related to η_A by:

$$\eta_B = \eta_A\left(\frac{U_{0B}}{U_{0A}}\right)^2\frac{T_B}{T_A}. \tag{3.11}$$

The λ_B of equation (3.3) is related to the λ_A by:

$$\lambda_B = \lambda_A\frac{T_B}{T_A}. \tag{3.12}$$

Chapter 4

Literature on LBM applications

The Lattice-Boltzmann method (LBM) has been systematically employed in several computational haemodynamics applications. A literature review on blood modelling flows with the Lattice Boltzmann Method is presented in this chapter.

4.1 Lattice Boltzmann Modelling of flows

The Lattice Boltzmann Method has been validated both theoretically, where it can be shown that it mimics the Navier-Stokes equation up to second order [21], and through its application to a range of diverse flow problems including acoustically induced flows [29], bubble dynamics [30], free surface flows [31] and flow in porous media [32]; as well as a range of blood flow simulations [33–39, 41, 111–131].

4.2 Lattice Boltzmann Modelling in general blood-flow projects

LBM has been applied to a limited number of blood-flow simulations. Krafczyk *et al.* [130, 131] considered blood flow through an artificial aortic valve, presented

details of transient flows at selected fixed openings and also considered a two-dimensional model with moving leaflets. Matyka *et al.* [127] calculated the wall shear stress in the human abdominal aorta, in steady flow using LBM and compared the results with a standard finite volume solver and experimental data available in the literature.

4.2.1 Lattice Boltzmann Modelling of blood flow in arteries

Artoli *et al.* [126] considered a two-dimensional model of a symmetric bifurcation and compared the LBM results to a Navier-Stokes solver. Axner [125] compared the LBM to the finite element modelling of the flow in a mesenteric artery. The LBM was validated for systolic flows by comparing the velocity and pressure profiles between the models. LBM was also shown to prove an alternative solution method for computational haemodynamics. Using LBM Chen et al. [124] examined the blood flow in a stented channel embedded in a a blood vessel and four human coronary artery geometries based on the images obtained from patients. For a model of stented flow involving an S-shape stent, a pulsatile flow rate was applied as the inlet boundary condition, and the time- and space-dependent flow field was computed. The LBM was found to be able to reproduce the velocity profiles and wall shear stress distributions for the pulsatile channel flow. For the coronary arteries, the distributions of wall shear stress, which were important for clinical diagnostic purposes, were in good agreement with conventional CFD predictions.

He *et al.* [120] used a haemodynamics analysis approach, a combination of medical imaging analysis and the LBM to simulate flow in cerebral vasculature geometry, a patient-specific cerebral vasculature geometry. Itani *et al.* [123] used an advanced LBM model, FabHemeLB (Python tool assisting automation, the construction and management of ensemble simulation workflows). FabHemeLB is built on HemeLB, as proposed in [121, 123]; that has been applied to simu-

late blood flow in healthy brain vasculature as well as in the presence of brain aneurysms [121, 122]. FabHemeLB was used also to examine the WSS properties in a middle cerebral artery at a location of interest close to the outlet.

4.2.2 Lattice Boltzmann Modelling of Blood Clotting

The formation of atherosclerotic plaques (deposits) within arteries, commonly leading to vessel stenosis, are features of cardiovascular disease. It is likely that regions of stagnant or recirculating flow will develop downstream of a stenosis and if blood remains in such a region for a prolonged period of time, thrombosis may occur. Tamagawa and Matsuo [38] simulated blood flow in a simple model of a blood pump or a medical fluid machine. They further estimated thrombus formation from the shear rate and the effective distance of the wall. Bernsdorf *et al.* [41,119] simulated blood clotting and unsteady flow within a stenosed artery. A simplified blood clotting process, described there, was based on a residence time model, using a lattice Boltzmann flow solver with passive scalar advective-diffusive transport. Tamagawa et al. [39] added the effects of surface tension and adhesion force because of thrombus at the wall. They simulated the thrombus formation by considering the effects of a threshold level of physical parameters such as shear rate and adhesion force (effective distance from the wall). They concluded from the designing viewpoint, the material with low adhesion force (effective length) should be located at the low shear rate and stagnation region in the pumps and other fluidics.

Bernsdorf *et al.* [119] simulated the blood clotting process using a residence time model. They simulated the clotting process numerically, extending LBM in two ways: an advection-diffusion scheme for a passive scalar [132] was applied in order to estimate the residence time of the fluid blood, and a solidification procedure depending on the 'age' of the fluid was introduced. It was assumed initially that activated fluid entered the flow domain at the inlet. The complex

process of blood coagulation was replaced by the 'residence time': if the activated fluid was 'old enough', it solidified. The fluid was presumed able to clot after a certain elapsed period post-activation. The local age of the fluid was determined by the concentration of the passive scalar tracer. When the local concentration of the tracer (computed at each timestep) reached a given threshold, solidification took place; a fluid site became a wall site and the solid surface boundary condition was applied. During any subsequent iterations, the flow field and age distribution adapted to the new geometry, while further clotting on adjacent fluid nodes could occur. Bernsdorf *et al.* in a later study [41] worked on an adaptation of the LBM for simulating blood coagulation within a stenosed artery. LBM was used to compute the flow field, the clotting was simulated via addition of an age scalar, subjected to a passive-scalar advection-diffusion scheme, and solidification occurred based on a threshold age.

Harrison *et al.* [40] presented a simple clotting model, based on residence time and shear stress distribution, that could simulate the deposition over time of enzyme-activated milk in an in vitro system. Carotid changes were observed in the blood clotting models. They compared the flow simulated with LBM and clot deposition to flow visualisation and experimental milk clots, respectively.

4.3 Cellular Nature of Blood

Blood is a heterogeneous multi-phase mixture of solid suspensions (of red blood cells, white blood cells and platelets) in a liquid plasma which is an aqueous solution of proteins, organic molecules and minerals. The rheological characteristics of blood are determined by the properties of these components [133–135] and their interaction with each other as well as with the surrounding structures.

4.3.0.1 Lattice Boltzmann Modelling of Cellular Material in Blood flow

At a microscopic level, blood is a concentrated suspension of several cellular components, including Red Blood Cells (RBCs) or erythrocytes, white blood cells or leukocytes, and platelets, suspended in plasma, an aqueous solution of numerous ions and macromolecules [13]. Among these cellular components, RBCs are the most important components because of their biological roles as carriers of oxygen and carbon dioxide and the direct influence of RBC properties on blood flow characteristics [135, 136]. Migliorini *et al.* [116] considered the forces acting on leukocytes due to red blood cells in a two-dimensional simulation of a blood vessel. This work was continued by Sun *et al.* [115]. Li *et al.* [33, 137] considered the transport of red blood cells through a two-dimensional symmetric model of an artery containing a semi-circular stenosis. Zhang [114] used the coupled LBM with Immerse Boundary (IB), (IB-LBM) to simulate the suspending viscosity effect on RBC dynamics and microscopic haemorheology in shear and channel flows.

Arterioles, small blood vessels that carry arterial (oxygenated) blood might be affected by atherosclerosis associated with vessel wall thickening and luminal narrowing. Vahidkhah and Fatouraee [112] simulated the interactions between the RBC membrane and plasma flow in a stenosed arteriole using the IB-LBM method, used in [114]. Using IB-LBM Alinejad and Fallah [111] examined the deformation of RBC transferred in a carotid artery whose flow subjects to drug delivery. It was shown in [111] that the IB-LBM can properly simulate the RBCs deformation and also damage to the vessel wall can lead to the formation of vortices inside the arteries and block to its passage.

4.3.0.2 Non-Newtonian simulations

Unless fluid flow forces are sufficient to keep them dispersed, red cells tend to adhere to each other due to bridging by plasma proteins [138]. In bulk shear flow, aggregation increases blood viscosity at low shear rates. As the shear rate is increased, the progressive breakup of aggregates leads to a decrease in viscosity ('shear thinning') [135]. Despite this fact, a large body of literature concerning computational haemodynamics characterises blood as a Newtonian fluid under the assumption that this is acceptable in large arteries [139].

Due to its kinetic essence, the LBM allows straightforward calculations of the local shear rate to second-order accuracy. It thus has been applied to simulate the non-Newtonian behaviour of blood flows. Boyd *et al.* [140] employed LBM to analyse the Casson and Carreau-Yasuda (C-Y) non-Newtonian blood models in steady and oscillatory flows. They compared their results to analogous Newtonian flows and characterised the differences. The use of a Non-Newtonian model has some effect on the blood flow especially at stenoses or bifurcations where the shear rate of blood is very small and its non-Newtonian nature cannot be neglected [141].

Wang and Bernsdorf [141] have used the Carreau Yasuda model applied to the Lattice Boltzmann Method to simulate the flow on several occlusion percentage geometries; general stenosed geometries created by a mesh generator. The non-Newtonian nature was modelled by the C-Y model and was compared to the Newtonian model. The Newtonian flow had a longer recirculation length than the non-Newtonian, due to the low shear rates within the recirculations, caused by the overestimate of the WSS. The shear stress for C-Y was lower than the Newtonian case.

Ashrafizaaden and Bakhshaei [142] compared three non-Newtonian models for lattice Boltzmann blood flow simulations: the Casson, C-Y and K-L models.

They demonstrated the capability of LBM for complex blood flows.

Yanhong Liu [143] used a Bi-viscosity model and compared it to the Casson model adapted from [144, 145] to simulate the blood flow of a stenosed artery. Yanhong Liu introduced a ceiling viscosity and cutoff viscosity to produce a relaxation time for $\sigma < \sigma_y$, (σ_y is the yield stress). Qualitative agreements were shown for the velocity profiles of the lattice Boltzmann Bi-viscosity model against that of the lattice Casson's model; well accepted as a useful method to simulate various fluid behaviours. In the meantime, research toward the heat transfer enhancement due to the use of nanofluid using lattice Boltzmann method has recently become attractive for many researchers.

4.4 LBM modelling the flow in stenosed geometries

Boyd *et al.* [78] simulated, using the LBM, flow in 2D arteries with varying degrees of stenosis. During the simulation, the arterial walls were assumed rigid and the level of compliance for the healthy walls was not considered. The aim of the study was to investigate how the wall shear varies in the presence of a stenosis. Thirty incrementally larger stenosis growths were implemented in such a way that the geometries varied smoothly between increments. The stenosis growth was implemented in a region of the carotid artery prone to atherosclerotic progression, which exhibits low velocity and a low near wall shear stress [3]. Maximum near wall shear stresses at points in the artery were compared with literature results and changes in the velocity and shear fields due to stenosis growth within the artery were examined. Regions of low velocity, rotational flow and low near wall shear were observed in areas of the unstenosed artery known to be susceptible to atherosclerosis. These regions persisted during the simulated stenosis growth as well as during the pulse cycle, suggesting that growing stenosis

maintain conditions in the artery which can further promote their growth. A small region of rotational flow was observed just upstream of the upper edge of the implemented stenosis. This may increase the particle residency time for lipids and blood cells in this region and further promote stenosis progression. This also suggested that the plaque build-up maintained flow conditions favourable to its progression.

Boyd and Buick [80] applied the LBM to examine the variations in velocity profiles across three regions of the artery, for different waveforms (resting with long period and lower mass flow rate, [97] and exercising, with shorter period and larger mass flow rate, [94]). Again, thirty incrementally larger stenosis geometries were implemented in a region known to exhibit low velocity flow and be susceptible to atherosclerosis, [78]. For the waveform describing heart at rest, it was observed that some low velocity rotational flow was preserved as the growth of the stenosis increased and remained adjacent to the stenosis region. For the exercising heartbeats waveform, the narrowing of the artery created higher shears near the wall of the stenosis.

Karimpour and Javdan [43] considered an LBM model, where a stenosis develops based on the details of the simulated arterial flow. The stenosis growth is based on the Oscillatory Shear Index (OSI) calculated along the artery wall. Regions of high OSI, which are related to the oscillatory nature of the WSS and which will be formally defined in Chapter 5, were deemed to be prone to atherosclerosis and layers of deposits were progressively deposited in these regions. Although no algorithm is presented in this work, this appears to be based on a pre-determined threshold similar to [38–41] and results in a layer of deposit at each step. The stenosis growth was simulated by laying a segment at these locations through converting adjacent fluid nodes to solid ones. The authors identified difficulties in applying their strategy due to the step-like nature of their artery walls which lead to boundary roughness; difficulty in defining the wall nor-

mal; and fluctuations in the wall velocity which feeds into the OSI calculation. To address this the authors introduced a 'parallel' surface three units from the wall which was used to calculate the WSS. The artery normal was defined to be the normal to the fluid velocity at this surface. Regions subjected to partial obstructions identified qualitatively well with those susceptible to atherosclerosis in an *in vivo* sample, thereby approving this criterion by verifying its accumulative effect. The artery walls were reshaped in a recursive manner. Shear stress level elevation was observed in the vicinity of the apex and the relative minimum near the sinus region.

In literature, LBM has been proposed to describe flow in geometries with distinct characteristics. A number of studies have been designed to simulate fluid flow through constricted tubes. Fu *et al.* [146] developed a Finite Difference Lattice Boltzmann model coupled to an Immersed boundary (FDLBM/IB) scheme to simulate the flow in constricted pipes. The model is based on the FDLBM model designed by Fu *et al.* [147, 148] that provides a convenient algorithm for setting the boundary condition using a splitting method to solve the discrete lattice Boltzmann (LB) equation. The FDLBM proposed in [147, 148], is not easily adapted to flows with complex boundary geometries. This is a serious drawback of the FDLBM which was intended to be overcome with the implementation of the IB method. In this study, the FDLBM was applicable for Newtonian and non-Newtonian fluids. The non-Newtonian flow through constricted tubes with different constriction geometries was demonstrated. In a related study [149], they validated the time-accurate FDLBM/IB scheme proposed in [146] in order to simulate Newtonian and non-Newtonian fluid flow in constricted tubes. FDLBM/IB was used to investigate a model blood flow problem of an axisymmetric pulsating flow in a constricted tube with 75% area occlusion in Newtonian fluid and non-Newtonian (C-Y) flow. This study showed a smaller pressure drop in non-Newtonian flow compared to the Newtonian flow under the same flow conditions.

LBM has also been used to simulate the pulsatile blood flow in realistic stenosed carotid arteries. Kang [150] used LBM to simulate the pulsatile blood flow in carotid artery bifurcations of internal carotid arteries for severe stenosed carotid bifurcations. The main focus of the investigation was the wall shear stress in the internal carotid arteries for severe stenosed and recanalised carotid bifurcations. The OSI was used to measure the oscillatory features of WSS during pulsatile cycles, representing the disturbed flow patterns leading to reverse velocity components occurring near the arterial walls. The stenosed carotid geometries were digitally reconstructed from a 2D human angiography with severe ICA stenosis. Kang validated the simulations conducted with the half-way bounceback scheme, against numerical experiments, on a 2D Poiseuille flow, which were inclined with respect to the lattice axis. Kang investigated the spatiotemporal and average distributions of the WSS along the outer and inner walls of the internal carotid arteries. In the severely stenosed arteries, the WSS increased dramatically in the narrowed area, thereby resulting in plaque rupture and thrombus formation. Along the path downstream of the stenosed segment, the severely disturbed flow also caused the lesion region to continue to expand downstream and become more serious.

Kang, in a second study [151], simulated the flow in a three-dimensional (3-D) moderate stenosed carotid bifurcations aiming to examine the relevance of the local haemodynamics to arterial atherosclerosis formation and its progression. The helical flow patterns, secondary flow and wall dynamical pressure spatiotemporal distributions were investigated, which lead to the disturbed shear forces in the carotid artery bifurcations. The study [151] concluded that the LBM was an attractive computational tool in haemodynamics research due to its high efficiency and robustness in dealing with complex boundaries.

Chapter 5

Medical problem

Atherosclerosis is a major cause of mortality in our society representing up to 35% of all deaths in the western world [1].

5.1 Pathogenesis of atherosclerosis

Cardiovascular diseases [1, 152, 153], particularly when they are atherosclerotic-related [152, 153] are responsible for a significant proportion of mortality in the developed countries [1, 2, 154, 155].

Among the many cardiovascular risk factors, elevated plasma cholesterol level is probably unique in being sufficient to drive the development of atherosclerosis, even in the absence of the next more widely known factors [156]. The other risk factors, such as hypertension [134, 157, 158], diabetes, smoking [157, 158], male gender, and possibly inflammatory markers (like C reactive protein and cytokines), appear to accelerate a disease driven by atherogenic lipoproteins, the first of which being Low-Density Lipoprotein (LDL) [156].

Exercise, and High-Density Lipoprotein (HDL) and its major apolipoprotein (apoA-I) confer protection against diseases caused by atherothrombosis. Among other things, HDL/apoA-I prevents the atherogenic modifications of LDL and

promotes 'reverse cholesterol transport' which retards plaque progression.

5.2 Composition of the arterial wall

The geometry of the arteries have been suggested to play a role in determining atherosclerotic lesion localisation [159]. Blood does not flow uniformly in the arterial tree because of variations in geometric configuration which impose resistance to flow. The artery wall is composed of the intima, which is covered on the luminal surface by a monolayer of endothelial cells; the media, which among its constituents contains smooth muscle cells, collagen, and elastin [157].

Endothelial cells, leukocytes, and intimal smooth muscle cells are the major activators in the development of this disease. Their dyfunctions favour the occurrence of Atherosclerosis [134].

Atherosclerosis is a chronic immunoinflammatory, fibroproliferative disease of large and medium-sized arteries fuelled by lipid [160, 161].

5.3 Localisation of Atherosclerosis

Certain vessels such as the abdominal aorta, carotid arteries [158], coronary arteries and peripheral arteries, are particularly susceptible to plaque formation, whereas others, such as upper extremity vessels rarely experience it [95, 157, 162, 163].

The distal internal carotid is mainly free of disease despite marked atherosclerosis in the adjacent carotid bifurcation [157].

Considering that blood flow exerts stresses on vessel walls and affects mass transport to the arterial tissue, we are led to the hypothesis that fluid dynamic forces are localising factors in atherogenesis [157].

5.4 Association of haemodynamics to Atherosclerosis

Blood flow in an arterial tree is not uniform. Differing lumen diameters, curvatures, branchings, and angles favour local disturbances in the primary flow field resulting in regions of altered shear stress [164] and boundary conditions with areas of separation, secondary flow patterns and occasional turbulence. Characterisation of these conditions at specific sites becomes much more complex when the pulsatile nature of blood flow is considered [157]. Branch points are known to be particularly vulnerable to plaque formation and are subjected to wide variation in haemodynamic conditions. Hence, it is not unexpected that a wide variety of haemodynamic factors have been connected to plaque pathogenesis, including high and low wall shear stress, flow separation and stasis, oscillation of flow, turbulence and hypertension [95, 162, 163, 165].

5.4.1 Shear stress

Prior to studying the association of the shear stress to the atherosclerosis its definition related to the flow in arteries has to be given.

Wall Shear Stress in arteries is the tangential force per unit area produced by blood moving across the endothelial surface [5, 157, 162]. WSS is an expression of the velocity gradient of blood near the endothelial surface and is dependent on blood flow, blood viscosity, as well as the geometry of the artery [157].

The endothelium is very sensitive to shear stress, and local haemodynamic conditions related to branching, low and oscillating shear, and reverse flow may offer some of the explanation for the fact that the coronary arteries are much more susceptible to atherosclerosis than the internal mammary arteries [161].

5.4.1.1 Reaction of endothelium to shear stress

Endothelium reciprocates through various pathophysiological mechanisms depending on the kind and the magnitude of shear stresses. Normal laminar flow induces adequate shear stress forces, which promote endothelial cells stability and increase their survival [166]. Also, these stresses align the endothelial cells in the direction of flow and participate to the secretion of agents with direct or indirect antithrombotic and vasodilatory properties such as Nitric Oxide (NO) [167] and thrombomodulin [168]. Especially the secretion of NO and transforming growth factor beta (TGF- β) are stimulated by normal levels of arterial shear stress (10-70 dyn/cm^2) [167, 169, 170] and inhibit smooth muscle cell proliferation [167, 168].

Under normal conditions, shear stresses maintain their direction and their magnitude within a range of values that does not enable atherogenesis, thrombosis, adhesion of leukocytes, smooth muscle proliferation, vascular remodelling and endothelial apoptosis [166]. Also, under normal shear conditions, endothelial as well as smooth muscle cells have a rather low rate of proliferation [170].

5.4.1.2 Association of shear stress variations with atherosclerotic processes

The carotid atherosclerosis is usually asymmetrical in the carotid artery [3, 95, 162, 163]. From Gnasso's study [3], the peak and mean wall shear stress are lower in carotid arteries where atherosclerotic plaques are located than in plaque-free carotids.

This concept is explained as there is a an association between the wall shear stress, the blood velocity. A reduction of shear stress contributes to an increased fluid residence time [171] and therefore to increased mass transport of atherogenic particles, thus interfering with endothelial metabolism [171].

Platelets more probably adhere to the endothelium in regions of increased

residence time and in human endothelial cells the Tissue Plasminogen Activator (TPA) secretion rate decreases with decreasing values of shear stress, at least in vitro experiments [158, 172, 173]. Furthermore, shear stress has been shown to modulate the transcription of genes for nitric oxide (NO) syntheses, platelet-derived growth factor and transforming growth factor-β1, all factors involved in vascular remodelling [134, 174–176].

Plaque localisation has been noted in humans and Caro and his associates [171] have suggested that low wall shear rates may retard the mass transport of atherogenic particles at the wall, resulting in increased intimal accumulation of lipids [171] interfering with endothelial metabolism.

Correlative studies of plaque localisation in the human carotid bifurcations [95, 96] with quantitative flow models have shown that intimal plaques form in the low shear stress region of the carotid sinus, opposite the flow divider, and not in the high shear stress region along the inner wall of the internal carotid artery [95, 96]. Negligible shear stress values were recorded in the region most likely to develop plaque [95]. It has been suggested that a threshold value below which plaque deposition occurs may exist [96].

5.4.2 Flow separation and Geometry

A number of flow field alterations, other than shear stress, occur at branch points and have been implicated in the plaque localisations. These changes are particularly prominent in the carotid bifurcation because of the carotid sinus and may account for the marked vulnerability of this site to atherosclerosis [157, 177]. The carotid sinus has double the cross-sectional area of the distal internal carotid artery and this, together with the effects of branching and angulation, results in a large area of flow separation and stasis along the outer wall of the carotid sinus [96, 157, 177]. As flow from the common carotid artery enters the bifurcation, flow streamlines are compressed toward the flow divider and inner wall of the internal

carotid artery where flow is rapid and laminar and shear stress is high [157]. Plaques do not form in this area. Along the outer wall of the sinus, a large area of flow separation develops in which flow velocity and shear stress are low. The earliest intimal plaques develop in this region, as do late, complicated, and clinically significant lesions [95].

In the region of flow separation, there is a reversibility of axial flow and slow fluid movement upstream. However, the region of separation is not simply a zone of stasis and recirculation but it is a zone of complex secondary flow patterns, including counterrotating helical trajectories [177].

Flow reattaches distally in the sinus, and the distal internal carotid, which is almost always free of plaque and has relatively experienced rapid axial flow throughout its cross-section. The presence of flow separation and stasis in patients in this outer wall region of the carotid bifurcation [95,177] has been also cited by ultrasound studies [177,178].

5.4.2.1 Oscillatory flow

The preferential sites atherosclerotic lesions to develop have been shown to lie in regions of low or oscillating shear stress [95, 162, 163].

Under conditions of pulsatile flow, the flow can be complex. Conditions along the inner wall of the carotid sinus are similar to those seen under steady flow conditions. Flow velocity and shear stress are high and flow remains laminar. There are fluctuations in magnitude of velocity and shear but without significant changes of direction [157]. Along the outer wall, where plaque is known to form, pulsatile flow produces an oscillating shear stress pattern [157, 179, 180].

During early systole, the region of flow separation disappears with forward flow throughout the cross-sectional area of the sinus. During late systole, however, the region of separation and flow reversal becomes prominent along the outer wall, and there is a reversal of direction in the shear stress directional vector [181].

During diastole, conditions are similar to those seen under steady flow conditions. The magnitudes of velocity and shear are low in this region and correlate strongly with plaque localisation. Oscillations in the WSS vector along the outer wall of the carotid sinus have also been shown to correlate strongly with early plaque deposition [96].

Ku [96] described increased residence time along the outer wall of the sinus which is caused by oscillations of fluid velocity about a mean value close to zero. This occurrence delays the convection of fluid and traps fluid elements near the outer wall for several cycles despite the absence of a clear region of stasis or of an area of permanent boundary layer separation.

Low shear stress probably contributes to an increased fluid residence time, which sequentially may result in increased transport of atherogenic particles or interfere with endothelial metabolism [171].

Platelets and macrophages, key elements of atherosclerotic lesions, are more likely to adhere to the arterial wall in regions of increased residence time and the TPA secretion rate of human endothelial cells decreases with decreasing values of shear stress, at least in experiments in vitro [173].

5.4.2.2 Oscillatory Shear Index

An oscillatory shear index (OSI) was introduced to describe the cyclic departure of the wall shear stress vector from its predominant axial alignment [96]. The rationale for development of OSI is justified as follows. In the common carotid artery, flow velocity near the wall, while pulsatile, is continually directed forward or cephalad (toward the head or anterior section), leading to wall shear stress acting in the positive axial direction [96].

However, different wall shear stress behaviour are observed at the outer and side walls of the bifurcation, particularly in the internal carotid sinus. At the side walls of the branches the stress vector changes direction with time [96]. Thus, OSI

could be useful to describe the degree of deviation of the wall shear stress from its average direction. Ku [96] showed that the outer wall of the bifurcation is a region of low, time-averaged, mean shear stress and oscillatory shear stress. Both the low and oscillatory stress contribute to an increased fluid residence time of the particles in the carotid sinus. Low mean shear stress and marked oscillations in the direction of wall shear stress may be critical factors in the development and localisation of atherosclerotic plaques. The OSI is calculated over a period and is defined as:

$$\mathrm{OSI} = 0.5 \left[1 - \frac{\left| \int_0^T WSS(t) dt \right|}{\int_0^T |WSS(t)|\, dt} \right] \tag{5.1}$$

5.4.2.3 Relative Residence Time

Particles in the region of flow separation [177] have an increased residence time and therefore a greater chance to interact with the vessel wall. Time-dependent lipid particle-vessel wall interactions would elevate the intimal entrapment of atherogenic particles [182]. Thereafter, this situation would promote the slow flow, facilitating hence the occurrence of the plaque formation [157].

Caro et al. poses a similar interpretation to the relationship of low flow to the fluid residence time [96,171,183,184]. Caro et al. supported that low shear stress urged high transport of atherogenic particles to the arterial wall [96,171,183,184]. The Relative Residence Time (RRT) is defined as:

$$\mathrm{RRT} \propto \left[\frac{\int_0^T |WSS(t)|\, dt}{T} (1 - 2\mathrm{OSI}) \right]^{-1}. \tag{5.2}$$

5.4.3 High Shear Stress flow and Endothelial injury

In contrast to low shear, high shear stress has been thought to promote plaque formation by evoking endothelial injury and disruption, thereby exposing the underlying artery wall to circulating platelets and Lipids [134]. Endothelial injury

and the response to endothelial injury has been implicated in plaque pathogenesis. According to this hypothesis [134] the endothelial lining of arteries is damaged by one of several factors, including mechanical forces such as shear stress and hypertension, chemical agents (like hyperlipidemia,homocysteine) acting in immunologic reactions, or hormonal dysfunction. The injury hypothesis also encompasses the response to such injury, including platelet deposition, release of platelet-derived growth factor (TGF- β), cellular proliferation, and lipid deposition [185, 186]. In particular, repeated endothelial injury would account for the localised nature of plaque deposition.

Activated endothelial cells which have become permeable to Low-Density Lipoprotein (LDL), are of higher replication rates, and develop prothrombotic properties. They express surface glycoproteins that promote the adhesion of neutrophils, monocytes, and platelets [187].

Thus, although mechanical endothelial injury is unlikely to be a significant contributing factor to plaque initiation, endothelial cell function plays an important role in the responses and functions of the artery wall. The functional state of the media appears to be important in plaque pathogenesis. At peak blood pressure, characterized by increased cells motion and so increased tensile loading along the walls in areas such as the proximals to the coarctation (congenital narrowing) of the aorta, there is smooth muscle cell proliferation, elevated biosynthetic activity, and plaque formation can occur [188].

5.5 Relationship of intimal media thickening to flow

A low shear stress has been associated with Intima Media Thickening (IMT) and plaque occurrence. In particular, an inverse relationship of the wall shear stress to the IMT of the arterial wall, has been observed. Gnasso [3, 189] showed that

the internal carotid diameter has been evidenced to rise with increasing values of blood pressure in regions of reduced flow velocity, accounting for the inverse correlation of these variables with wall shear stress.

A possible relationship between IMT and near wall velocity magnitude considering a viscosity distribution in human coronary arteries has been investigated using Finite Element Modelling by Giannoglou [190]. Low velocity at each point along the length of the vessel was shown to be significantly correlated with IMT.

An interpretation of the relationship between the low velocity and the IMT was proposed by Giannoglou [190]. They suggested that a low near wall velocity promotes wall thickening which is probably due to increased residence time of blood lipoproteins. Long residence time permits the prolonged contact with the endothelium and increases the uptake of LDL lipoproteins particles [95, 163, 191].

Ku [96] verified the occurrence of the intimal thickening in areas of low time averaged shear stress over the pulse. In contrast to the shear stress, the oscillatory shear index was strongly correlated to the intima media thickening [96]. Along the inner wall of the internal carotid sinus, at points where lesions were least prominent, velocity magnitudes were similar to those measured in the common carotid artery lower. Along the anterior and posterior walls of the sinus, where lesions were of intermediate thickness, velocities were lower. Along the outer wall of the carotid sinus, where lesions were thickest, flow velocity was greatly reduced and high oscillations were observed.

Chapter 6

Stenosis growth model

This chapter describes the model used to simulate the stenosis developed. Its development and implementation are considered.

6.1 Boundary movement mechanism

Here we consider a model which monitors the blood flow in the carotid artery over a period and adjusts the wall geometry, based on the simulated blood flow, to model the development of a stenosis. The concept of the presented model is not that the stenosis develops every period; rather the assumption is that there are a large number of periods between each sequential change in the boundary and the flow properties do not change over this time. Thus there is no advantage in simulating all the intermediate periods which are identical. Based on this assumption, that simulations will not give a precise time scale for the development of the stenosis, but rather will indicate its sequential development.

6.2 Boundary description and orientation

The position where the stenosis develops is selected to be one of the fluid sites $\mathbf{a}_j$ which are selected as the set of all fluid sites $\mathbf{x}$ which are adjacent to the arterial

wall; that is $\mathbf{a}_j$, is a fluid site with at least one link which cuts the boundary.

The artery geometry is defined by a series of boundary points $\mathbf{b}_k$ which lie at the intersection of the artery wall and each link which cuts it. Boundary conditions are applied at each boundary point $\mathbf{b}_k$ using a sub-grid accurate extrapolation boundary scheme [77], see Section 2.9.3, which maintains the second-order accuracy of the LBM while describing the geometry of the artery to a resolution greater than the underlying lattice [94, 192].

It is also necessary to define, for each $\mathbf{a}_j$, a grid-based normal direction (out of the wall) defined as $\mathbf{l}_j$. For each $\mathbf{a}_j$ (fluid site adjacent to the wall), the grid base normal $\mathbf{l}_j$ was defined to be one of the m links, subset of the 6 links at the site, which intersect the boundary, $m < 6$. The m links are $\mathbf{e}_n^b$, $n = 1, \cdots m$. When $m = 1$, (only one link through $\mathbf{a}_j$ cuts the artery wall), the normal is set to $-\mathbf{e}_1^b$. A negative sign is required since $\mathbf{l}_j$ is defined to be an outward normal. For $m > 1$ a vector $\mathbf{b}$, approximating the local boundary, is defined joining the first and last boundary points for the site $\mathbf{a}_j$.

For example, in Figure 6.1 the hexagonal node has two links $\mathbf{e}_3$ and $\mathbf{e}_6$ which cut the boundary (thin solid line) at the boundary points (solid squares) $\mathbf{b}_0$ and $\mathbf{b}_1$ respectively. Thus $k = 2$ and $\mathbf{e}_1^b = \mathbf{e}_3$ and $\mathbf{e}_2^b = \mathbf{e}_6$. $\mathbf{l}_j = -\mathbf{e}_3 = \mathbf{e}_1$ is found as the closest grid-based normal to b. This is found numerically as

$$\mathbf{l}_j = -\arg\min_{\mathbf{e}_n^b} \frac{\left|\mathbf{e}_n^{\mathbf{b}} \cdot \mathbf{b}\right|}{\left|\mathbf{e}_n^{\mathbf{b}}\right| |\mathbf{b}|}. \tag{6.1}$$

We note that in Figure 6.1 it is converted to label $\mathbf{b}_m$ such that $\mathbf{b}_0$ is on link $\mathbf{l}_j$ through the site $\mathbf{a}_j$. The remaining boundary points are labelled sequentially.

It is also required to find a unit normal $\mathbf{n}_j$, which is not restricted to lie on a lattice link and the associated unit tangent, $\mathbf{t}_j$. For each $\mathbf{a}_j$ (fluid site adjacent

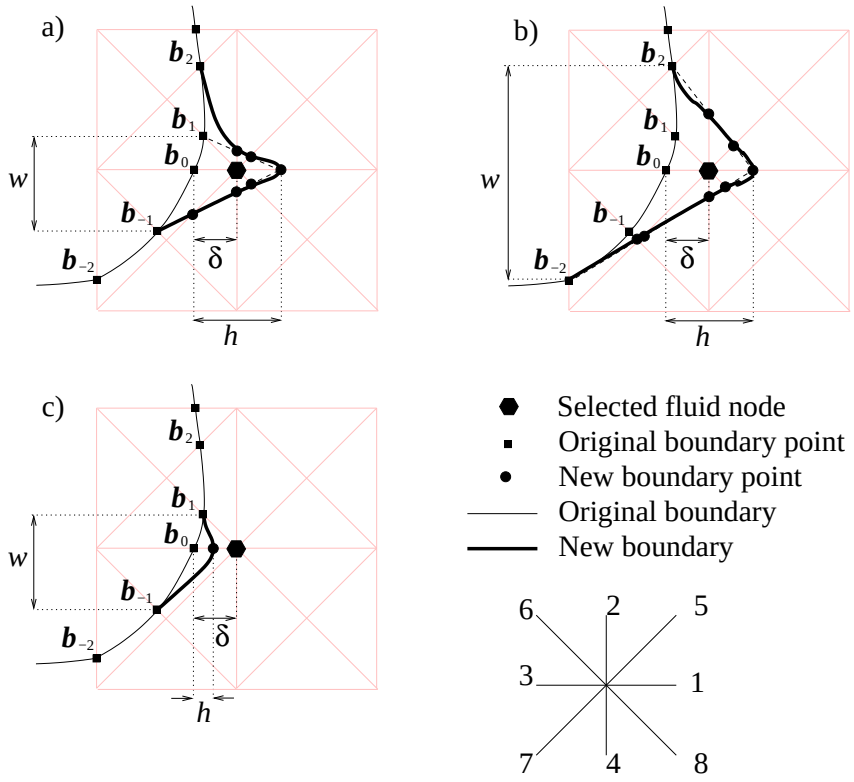

Figure 6.1: Model for the wall development is shown for selected values of h and w; (a) $h = 0.5$, $w = 1$, (b) $h = 0.5$, $w = 2$, (c) $h = 0.15$, $w = 1$. The movement boundary scheme depends on h and w which have no physical significance. These parameters relate to the extent to which the stenosis can grow in each development phase.

to the wall), the unit tangent $\mathbf{n}_j$ is defined as

$$\mathbf{t}_j = \frac{\mathbf{b}_{10} - \mathbf{b}_{-10}}{|\mathbf{b}_{10} - \mathbf{b}_{-10}|}. \tag{6.2}$$

$\mathbf{n}_j$ is then found as the unit vector which satisfies

$$\mathbf{n}_j \cdot \mathbf{t}_j = 0. \tag{6.3}$$

The orientations of $\mathbf{n}_j$ and $\mathbf{t}_j$ are selected such that $\mathbf{t}_j$ is pointing downstream and $\mathbf{n}_j$ is pointing into the fluid.

6.3 Selection criteria

There is a growing body of evidence which suggests a correlation between regions of low WSS and early development of atherosclerosis [3–8]. It has also been suggested that, within regions of low WSS, oscillatory flow may also be associated with regions where stenosis is observed to develop [11,95,96]. Here we considered the following haemodynamic markers for the development of the stenosis:

- TA velocity magnitude
- TA tangential velocity modulus
- TAWSS
- TA seconds invariant of the deviatoric stress tensor, TAD_{II}
- Oscillatory Shear Index (OSI)
- Ratio OSI: TAWSS (O:WS)
- Relative Residence Time (RRT)
- Reversibility Flow Index (RFI)
- Stagnation index (SI)

6.3.1 Velocity magnitude

Since the velocity is zero at the wall, it is necessary to calculate the velocity a short distance from the wall - here we selected 1 lu. Thus the velocity associated with $\mathbf{a}_j$, 1 lu from the wall along link $\mathbf{l}_j$ can be expressed

$$\mathbf{u}_j^{(1)}(t) = \frac{\mathbf{u}_j^{(\delta)}(t)}{\delta}, \tag{6.4}$$

where δ is the distance from the wall to $\mathbf{a}_j$ and $\mathbf{u}_j^{(\delta)}(t)$ is the velocity a distance δ from the wall, that is

$$\mathbf{u}_j^{(\delta)}(t) = \mathbf{u}(\mathbf{a}_j, t). \tag{6.5}$$

Alternatively, we can write

$$\mathbf{u}_j^{(1)} = \frac{(l_j + \delta_j - 1)\mathbf{u}_j^{\delta}(t) + (1 - \delta_j)\mathbf{u}_j^{(l+\delta)}}{l_j}, \tag{6.6}$$

where $\mathbf{u}_j^{(l+\delta)}(t)$ is the velocity a distance $l_j + \delta_j$ from the wall along link $\mathbf{l}_j$. That is

$$\mathbf{u}_j^{(l+\delta)}(t) = \mathbf{u}(\mathbf{a}_j + \mathbf{l}_j, t) \tag{6.7}$$

and

$$l_j = |\mathbf{l}_j|.$$

Since equation (6.4) can become unstable for small δ_j, equation (6.6) was used except if $\mathbf{a}_j + \mathbf{l}_j$ is not in the fluid. The site selected, $\mathbf{A}$ for stenosis development, based on their minimum TA velocity magnitude, was found for the Nth period as

$$\mathbf{A} = \arg\min_{\mathbf{a}_j} \int_{N_p T}^{(N_p+1)T} u_j^{(1)}(t)\, dt. \tag{6.8}$$

6.3.2 Tangential velocity

The tangential velocity component $u_{jt}^{(1)}(t)$ was found as

$$\mathbf{u}_{jt}^{(1)}(t) = \mathbf{u}_j^{(1)}(t) \cdot \mathbf{t}_j, \tag{6.9}$$

where $\mathbf{u}_j^{(1)}(t)$ was calculated from equation (6.4) or equation (6.6). The position where the stenosis development was modelled for the Nth period based on the

TA tangential velocity was

$$\mathbf{A} = \arg\min_{\mathbf{a}_j} \int_{N_pT}^{(N_p+1)T} \mathbf{u}_j^{(1)}(t) \cdot \mathbf{t}_j dt. \tag{6.10}$$

.

6.3.3 Wall Shear Stress

Here, we progress in a similar fashion to the velocity, except that we require the values at the wall, rather than 1 lu away. Thus

$$\sigma_j^{(0)}(t) = \sigma_j^{(\delta)}(t) - \frac{\delta_j}{l_j}\left(\sigma_j^{(l+\delta)}(t) - \sigma_j^{(\delta)}(t)\right), \tag{6.11}$$

where $\sigma_j^{(\delta)}(t) = \sigma(\mathbf{a}_j, t)$ and $\sigma_j^{(\delta+l)} = \sigma(\mathbf{a}_j + \mathbf{l}_j, t)$. We define WSS at time t:

$$WSS_j(t) = \sigma_{j\alpha\beta}^{(0)} n_\beta. \tag{6.12}$$

The selected site is then found by monitoring the Time Average WSS (TAWSS):

$$\mathbf{A} = \arg\min_{\mathbf{a}_j} \int_{N_pT}^{(N_p+1)t} \left|\sigma_{j\alpha\beta}^{(0)} n_\beta\right| dt. \tag{6.13}$$

6.3.4 Second invariant of the deviatoric stress tensor

Based on the second invariant of the deviatoric stress tensor we can define at the selected site for stenosis growth as:

$$\mathbf{A} = \arg\min_{\mathbf{a}_j} \int_{N_pT}^{(N_p+1)t} \left|\left|D_{jII}^{(0)}\right|\right| dt. \tag{6.14}$$

where:

$$D_{jII}^{(0)} = \frac{1}{2}\sigma_{j\alpha\beta}^{(0)}\sigma_{j\alpha\beta}^{(0)}. \tag{6.15}$$

6.3.5 Oscillatory Shear Index (OSI)

Ku et al, [96], proposed the Oscillatory Shear Index (OSI) to describe the shear stress acting in directions other than the direction of the temporal mean shear stress vector. It was used here to measure the cyclic departure of the WSS (t) from its predominant axial alignment. We calculated OSI at the boundary point following equation (5.1),

$$\mathrm{OSI}_j = 0.5 \left[1 - \frac{\left| \int_0^T WSS_j(t) dt \right|}{\int_0^T |WSS_j(t)|\, dt} \right] \tag{6.16}$$

This gives the value $0 \leq \mathrm{OSI}_j \leq 0.5$. The selected criterion is:

$$\mathbf{A} = \arg\max_{\mathbf{a}_j} \mathrm{OSI}_j. \tag{6.17}$$

6.3.5.1 Ratio OSI:WSS

We calculated alternatively O:WS at the wall to model the effect of both the OSI and the TAWSS:

$$\mathrm{O{:}WS}_j = \frac{\mathrm{OSI}_j}{|\mathrm{WSS}_j|}. \tag{6.18}$$

The selected criterion is:

$$\mathbf{A} = \arg\max_{\mathbf{a}_j} \mathrm{O{:}WS}_j. \tag{6.19}$$

6.3.6 Relative Residence Time

We can also use the Relative Residence Time (RRT), defined through equation (5.2) to monitor the residence time of the trapped blood particles at the boundary point $\mathbf{b}_j$. Here the selection criterion as

$$\mathbf{A} = \arg\max_{\mathbf{a}_j} \left[\frac{\int_0^T |WSS_j(t)|\, dt}{T} (1 - 2\mathrm{OSI}_j) \right]^{-1}. \tag{6.20}$$

6.3.7 Reversibility Flow Indexes

The Reversibility Flow Index (RFI) is used to monitor reversibility and is defined as:

$$\mathrm{RFI}_j = \frac{N_{jR}}{T} \tag{6.21}$$

where N_{jR} is the number of time-steps during the period where $\mathbf{u}_j^{(1)} \cdot \mathbf{t}_j < 0$. The selected criterion is:

$$\mathbf{A} = \arg\max_{\mathbf{a}_j} \mathrm{RFI}_j. \tag{6.22}$$

6.3.8 Stagnation index

In a similar way we use the Stagnation Index (SI) to monitor the regions affected by low velocity. We calculated the stagnation index at 1 lu from the wall, SI_j:

$$\mathrm{SI}_j = \frac{N_{jS}}{T}. \tag{6.23}$$

where N_{jS} is the number of time-steps where $\left|\mathbf{u}_j^{(1)}(t)\right| \leq 1\%$ of the maximum velocity of the driving pulse. The selected criterion is:

$$\mathbf{A} = \arg\max_{\mathbf{a}_j} \mathrm{SI}_j. \tag{6.24}$$

6.4 Boundary movement

The mechanism for modifying the artery wall, to represent the development of the stenosis, is shown in Figure 6.1 where the hexagon represents the fluid site selected $\mathbf{A}$, based on one of the criteria set out in Section 6.3. The re-positioning of the wall is based on two parameters h and w which represent the height and width of the deposited plaque, as shown in Figure 6.1. The original artery wall is shown by the thin solid line with the fluid sites (blood flow region)

to the right. The boundary points $\mathbf{b}_k$ are shown by the solid squares at the intersections of the artery boundary and the grid links. For this configuration of the artery boundary and the selected fluid site the link-based normal direction found from equation (6.1) is $\mathbf{e}_1$, the boundary point on this link is labelled $\mathbf{b}_0$, and $\delta = |\mathbf{A} - \mathbf{b}_0| = 0.3$. The remaining wall points are then labelled $\mathbf{b}_{\pm 1}, \mathbf{b}_{\pm 2}$, such that they are numbered sequentially, as shown in Figure 6.1. Three cases are shown corresponding to (a) $h = 0.5$, $w = 1$, (b) $h = 0.5$, $w = 2$ and (c) $h = 0.15$, $w = 1$. For these parameters the new section of the artery wall is shown by the thick solid line and the corresponding new wall points by the filled circles. For these parameters the new section of the artery wall is shown by the thick solid line and the corresponding boundary points by the filled circles. In Figure 6.1 (a) $h = 0.5$ and boundary point $\mathbf{b}_0$ moves h (0.5) units along the normal link ($\mathbf{e}_1$) towards the selected wet node. Since here $h > \delta$, ($\delta = 0.3$), the boundary encapsulates the selected fluid site which becomes wall. Construction lines are then drawn between this new boundary point and the old boundary links $\mathbf{b}_{\pm w}$ (here $w = 1$). New boundary points are then selected where the construction lines cross the links. In Figure 6.1 (a) the new boundary follows the lower construction line through the new boundary points. However, boundary point $\mathbf{b}_1$ is on link $\mathbf{e}_6$ out of the selected wet node $\mathbf{A}$. Since this is now a wall node and the link joins two wall nodes, it is not possible for it to have an associated boundary point. Thus the upper part of the new boundary connects to the next-nearest boundary point: $\mathbf{b}_2$. In Figure 6.1 (b) $h > \delta$ and $w = 2$, the construction lines connect to the old points $\mathbf{b}_{\pm 2}$ and the new boundary follows the construction lines. In Figure 6.1 (c) $h < \delta$, $w = 1$ the old boundary point, $\mathbf{b}_0$ moves h (0.15) units along the normal link ($\mathbf{e}_1$) towards the selected wet node ($\mathbf{A}$). This produces a new boundary point on the same link, a distance 0.15 closer to $\mathbf{A}$. Construction lines are then drawn between this new boundary point and the old boundary links $\mathbf{b}_{\pm w}$ (here $w = 1$). New boundary points are then selected where the construction

lines cross the links.

6.5 Summary

A model for simulating the development of a stenosis within the LBM has been set out. The stenosis develops in stages, based on the local wall haemodynamics. A number of markers for stenosis development are presented based on different haemodynamic properties. A mechanism for the movement of the artery wall was also presented. This is based on two parameters h and w which determine the height and width of the wall movement. These parameters do not have a physical interpretation and their use in the model will be considered in detail in Chapter 8.

Chapter 7

Haemodynamics in a healthy artery

Before considering the application of the stenosis development model described in chapter 6, it is interesting to consider what happens in the healthy artery. This gives details of the blood flow to establish the flow regime in regions where the stenosis will later develop, and will enable comparisons to be made between the flow in a healthy artery and a stenosed one.

The velocity and vorticity field for a healthy artery is shown in Figure 7.1 at the times $2T/66$ T (a and b); $4T/66$ (c and d); $6T/66$ (e and f); $9T/66$ (g and h); $11T/66$ (i and j); $13T/66$ (k and l); $15T/66$ (m and n); $17T/66$ (o and p); and $19T/16$ (q and r). Velocity profiles are shown in the left column while vorticity is in the right column. During the initial acceleration phase, Figures 7.1 (a) and (c), two regions of low velocity are observed, one on the outer wall of the ICA and the other on the outer wall of the ECA. The region on the ECA starts below the bifurcation and extends to slightly above the branch point. The region on the ICA also starts below the bifurcation, but extends significantly further downstream. During this time there is no significant vorticity in the artery. Figures 7.1 (c) and (d) correspond to a time close to the peak velocity. Here the velocity is higher across the whole artery - the areas of low velocity observed at earlier times are still present, but their size is much reduced.

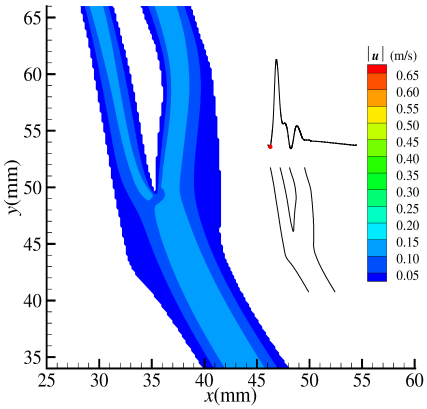

(a) u at $2T/66$

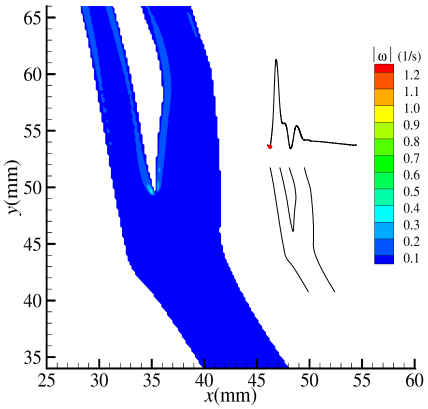

(b) ω at $2T/66$

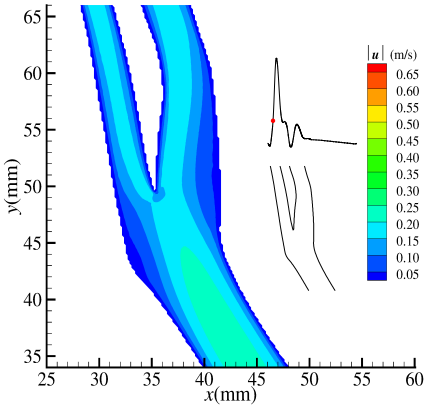

(c) u at $4T/66$

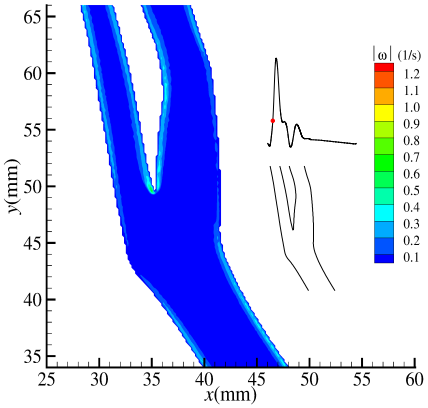

(d) ω at $4T/66$

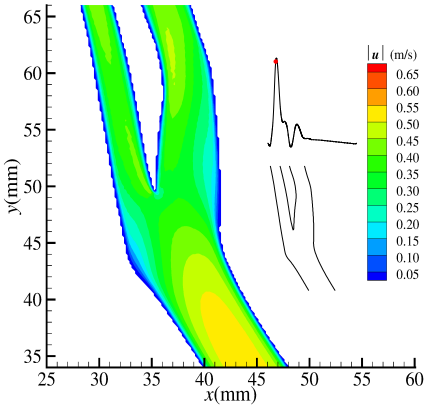

(e) u at $6T/66$

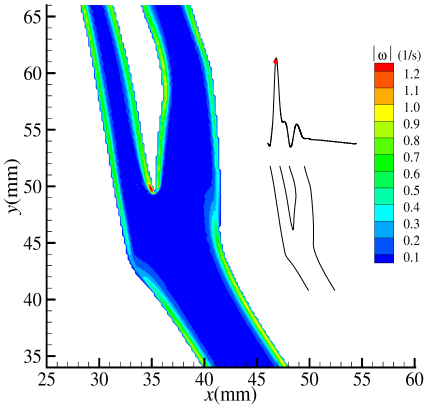

(f) ω at $6T/66$

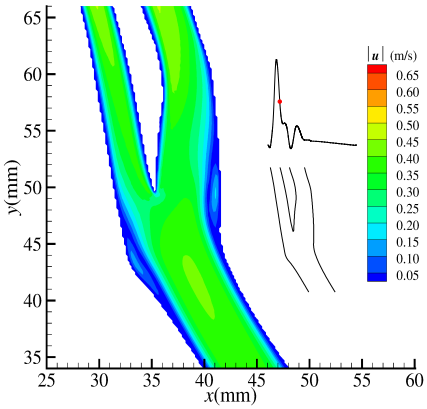

(g) u at $9T/66$

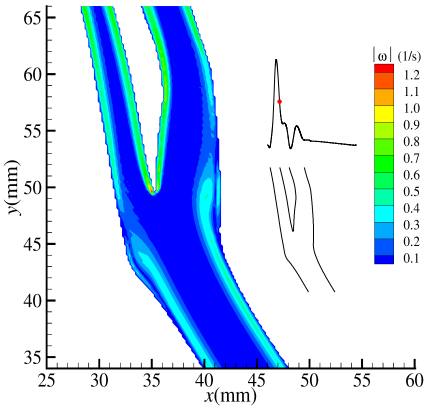

(h) ω at $9T/66$

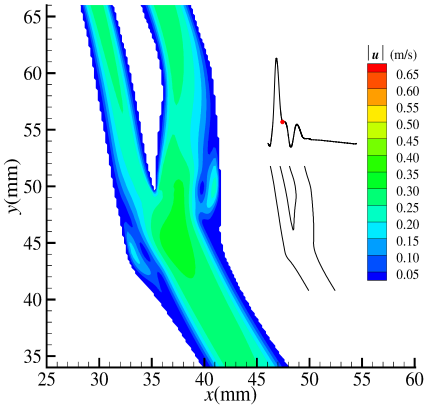

(i) u at $11T/66$

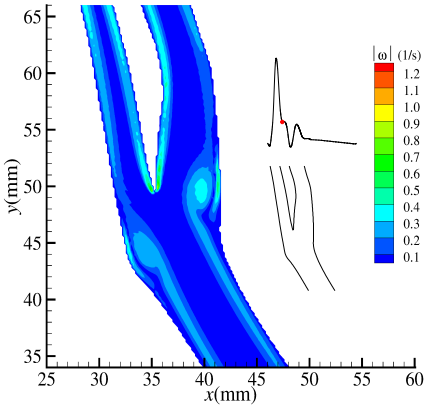

(j) ω at $11T/66$

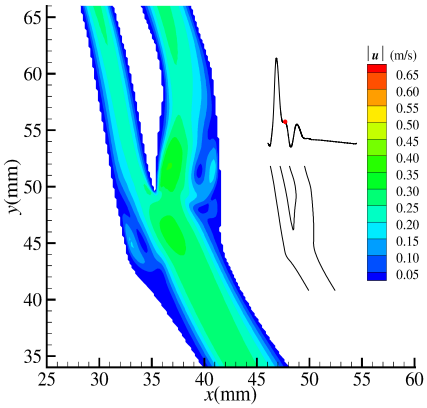

(k) u at $13T/66$

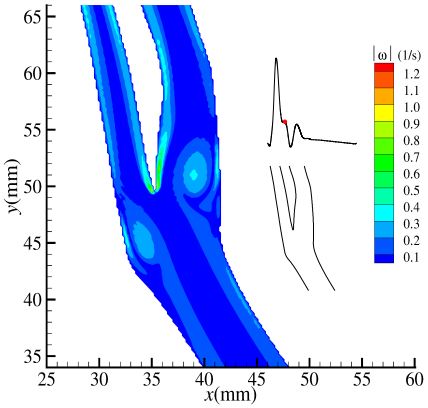

(l) ω at $13T/66$

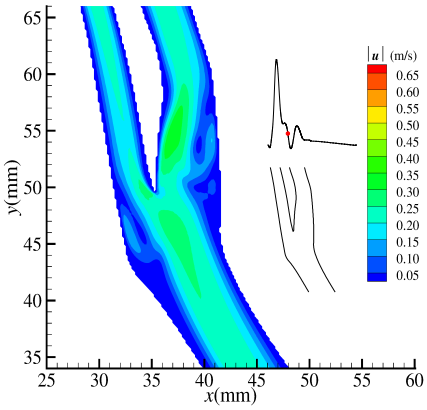

(m) u at $15T/66$

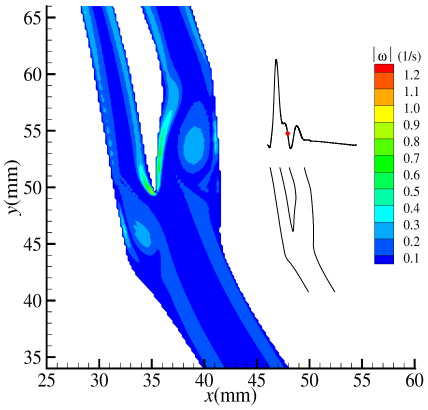

(n) ω at $15T/66$

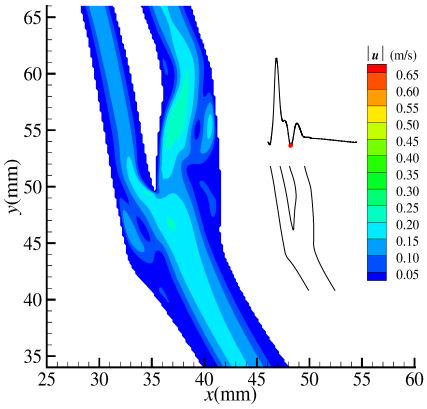

(o) u at $17T/66$

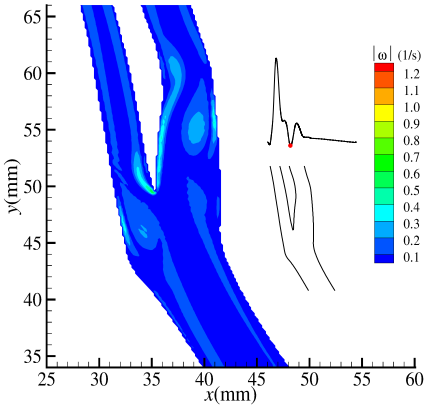

(p) ω at $17T/66$

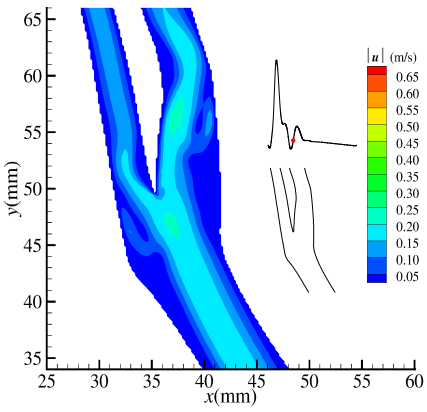

(q) u at $19T/66$

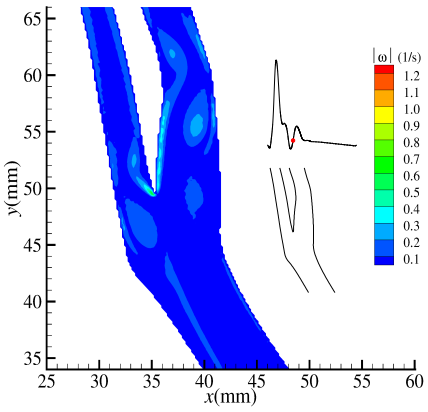

(r) ω at $19T/66$

Figure 7.1: Velocity ($u = |\mathbf{u}|$) (left column) and vorticity $\omega = (|\boldsymbol{\omega}|)$ (right column) for the healthy artery at $2T/66$ (a and b), $4T/66$ (c an d), $6T/66$ (e and f), $9T/66$ (g and h), $11T/66$ (i and j), $13T/66$ (k and l), $15T/66$ (m and n), $17T/66$ (o and p) and $19T/66$ (q and r).

As the flow decelerates, Figures 7.1 (g) - (j), the low velocity regions are re-established; however, they now correspond to a region of vorticity, with a vortex being formed in each region. Figures 7.1 (k) - (r) correspond to times when the velocity is relatively low. During this time the vortices move downstream and reduce in strength. Both have an affect on the flow, but it is greater in the ICA because the vortex progresses further into this branch, due to the different positions where the two vortices were generated. During the rest of the period the vorticity dies out completely and the velocity remains low and decreases in a fairly uniform manner across the artery.

These observations are consistent with previous studies using the same model [78, 94].

Chapter 8

Stenosis model results

The stenosis model described in chapter 6 is considered and discussed. Simulations of stenosis development are presented to investigate the effect of the model parameters w and h to determine suitable ranges for their application. Flow fields are also presented which indicate that the stenosis is developing in a realistic manner, providing evidence that the stenosis development is indeed influenced by the low velocity magnitude rather than occurring in such areas coincidentally.

8.1 Illustration of stenosis growth

It is important to establish how the h and w parameters relate to the extent to which the stenosis can grow in each development phase and how h and w affect this. There are two distinctive time-scales which play a significant role in the stenosis development; these are the heartbeat and the development time of the stenosis. The concept of the model is not that the stenosis develops every period; rather the presumption is that there are a large number of periods between each sequential change in the boundary when the flow properties do not change. Therefore, there is no benefit in simulating all the intermediate periods which are identical. Based on the assumption that we only need to simulate selected

periods where the stenosis changes, the number of periods will not give a precise scale for the development of the stenosis, but rather will indicate its sequential development. Additionally it is not evident that the relationship between the two time-scales will be linear. It is also evident that the stenosis will develop more quickly for larger values of h and w and so the number of periods simulated will not be a good measure of the progression since it is dependent on two non-physical parameters. For this reason, as well as to investigate the effect of h and w on the stenosis development, it is also important to find a variable which will describe the evolution in a manner which is independent of h and w.

8.1.1 Layer Development

The manner of the stenosis development in shown in Figure 8.1, where N represents the number of periods of simulation. This development generally occurs in

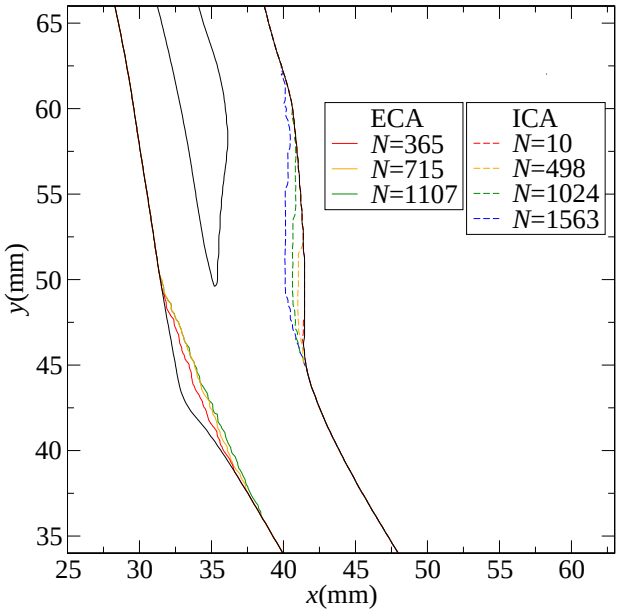

Figure 8.1: The development of the stenosis for $h = 0.7$ and $w = 1$. The stenosis geometry is shown at selected times corresponding to the final period during which each of the layer is developed.

a series of layers which build up from the bottom towards the top of the artery.

After each layer is completed a new layer starts either on the same artery wall or on the opposite wall. For selected layers, Figure 8.1 displays the geometry of the stenosis at the final period over which the layer develops. The layers selected in Figure 8.1 correspond to where a switch occurs between the ICA, on the right of the image, and the ECA, shown on the left. While this description of the stenosis development describes the general process, there are a small number of times where this pattern is broken. Typically, a larger layer, such as the one shown at $N = 365$, which is formed between $N = 10$ and $N = 365$ is composed of a number of sub-layers. There are also a small number of times where this pattern is broken. In these cases the site selected by equation (6.10) is either on the opposite wall or at a different position on the same wall. This can occur for two or three periods before it returns to the current layer. We also note that the development of these layers occurs only on the outer walls of both ICA and ECA. Although the geometry of a stenosis can vary significantly from patient to patient, the geometry shown in Figure 8.1 has geometrical similarities to some imaged arteries [193–196] suggesting that the modelling is performed in a realistic manner.

8.2 Stenosis Development

The results in Figure 8.2 show the stenosis development for different values of h, in terms of T_s which is a sequential label indicating the number of sites converted from wet to dry. For $h = 1$ this corresponds to the number of periods, N, for which the simulation had been running. For $h < 1$ we find $T_s \simeq N/h$. The advantage of using T_s to describe the time evolution of the stenosis rather than N, stems from its being a regular measure independent of h and w. The simulations in Figure 8.2 run until the stenosis reached a top buffer zone at $y = 63$ mm. It is evident from Figure 8.2 that this occurs at a value of T_s of around 750 for the lower values

of h and at a higher value of around 1900 for $h = 1$. The effect of the larger development time can be seen as the considerable thicker wall growth on both the outer walls for $h = 1$, and to a lesser extent for $h = 0.9$. To better evaluate the procedure, Figures 8.3 and 8.4 depict the same results with regards to the normalised parameters T_s^* and T_s^{**} respectively. T_s^{**} is obtained by normalising T_s by the run time in periods which is the maximum value of T_s for each individual run. This gives a normalisation with respect to the extent of stenosis development along the artery wall. In contrast, T_s^* is obtained by normalising with respect to the minimum of these run lengths over the range of h considered. This gives a normalisation with respect to the volumetric (areal) development of the stenosis. To enable a direct comparison, only values of $T_s^* \leq 1$ are shown in Figure 8.3. The results in Figure 8.3 show similar stenosis progression for $h = 0.1$, 0.3 and 0.5. The results for $h = 0.7$ are somewhat similar, while those for the larger values of h are significantly different in terms of the wall plaque extending less far along the wall, but further into the interior of the artery. This can be understood in terms of the mechanics of the model. When $h = 1$, as soon as a wet node is selected by equation (6.8) it is removed from the artery and the stenosis develops into the artery by 1 lattice unit. If $h = 0.1$, then the same wet site can potentially be re-selected for a further nine periods (possibly sequentially) before it is converted to a dry site. However, during this time, it is feasible that the small increments can sufficiently change the flow such that the development moves to another layer and an alternative site is selected; and the original one is not returned to (at least until a later stage in the development of the stenosis). Based on this picture of the stenosis development, it is evident that as h increases, it will reach a level at which the resolution of the artery refinement becomes too large and the value of h becomes significant in determining the evolution. Figure 8.3 suggests that this happens for values of h between 0.5 and 0.7. This would also suggest that the limiting value of h is based on the fraction of a lattice unit, rather than the

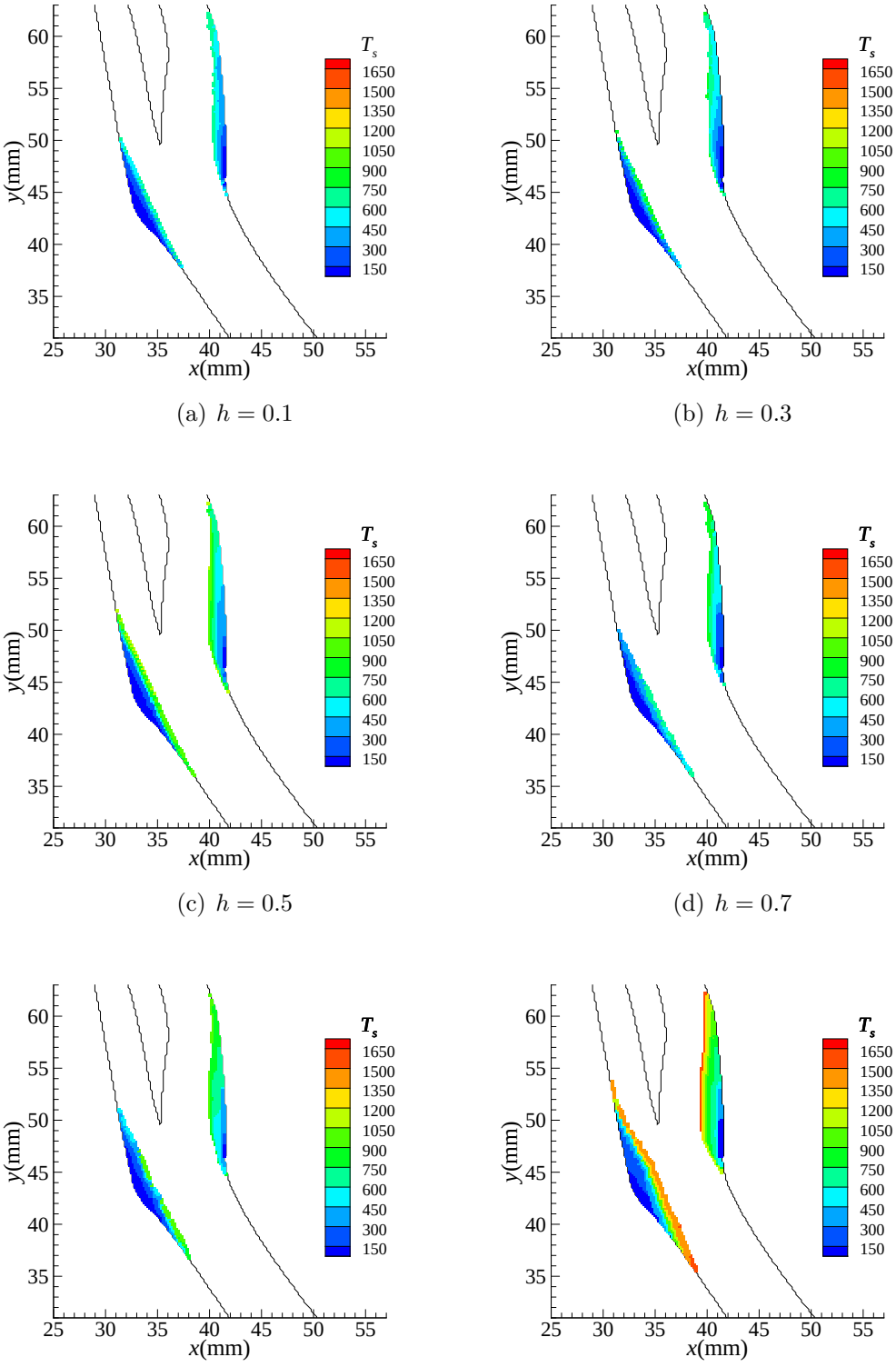

(a) $h = 0.1$ (b) $h = 0.3$

(c) $h = 0.5$ (d) $h = 0.7$

(e) $h = 0.9$ (f) $h = 1.0$

Figure 8.2: Stenosis development in terms of T_s for different values of h, when compared to $h = 0.5$.

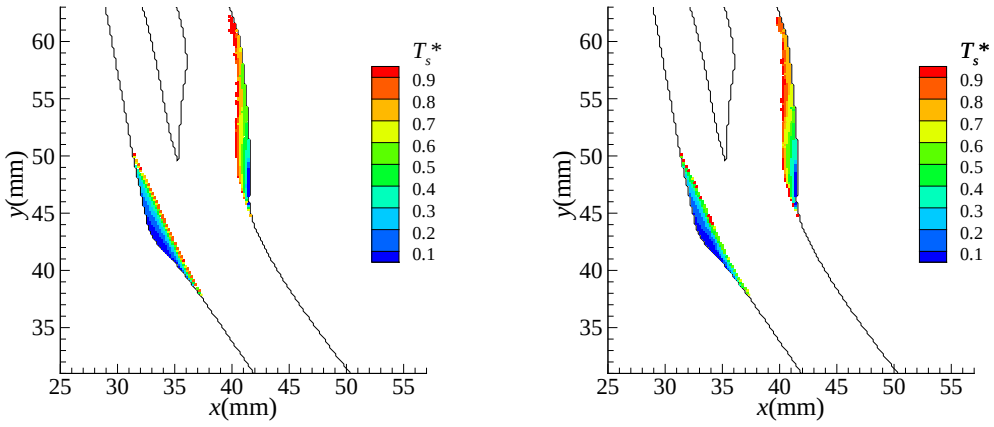

(a) $h = 0.1$ (b) $h = 0.3$

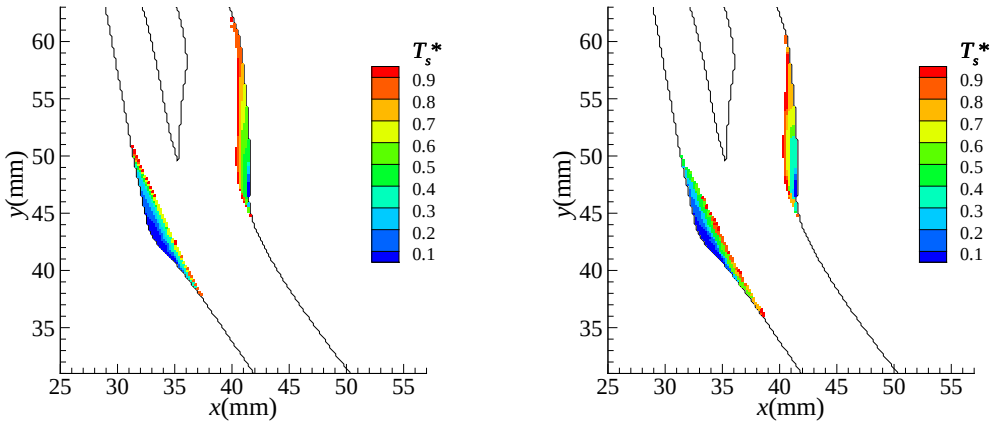

(c) $h = 0.5$ (d) $h = 0.7$

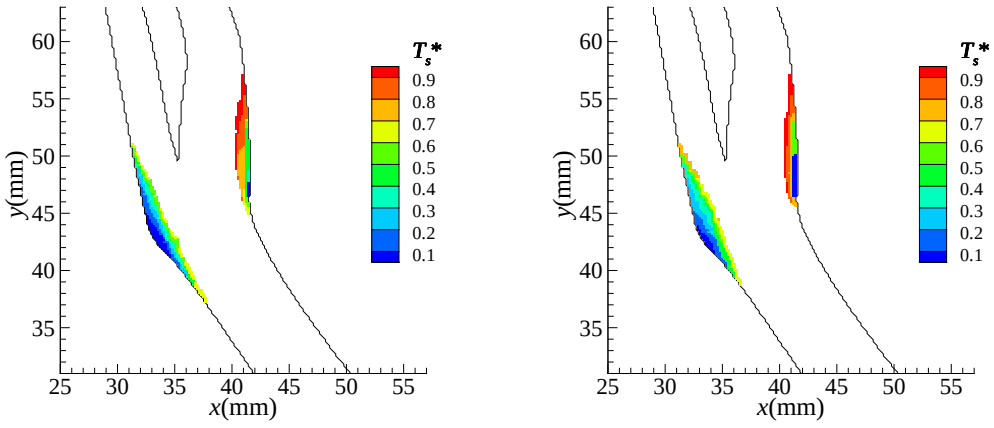

(e) $h = 0.9$ (f) $h = 1.0$

Figure 8.3: Stenosis development in terms of T_s^* for different values of h.

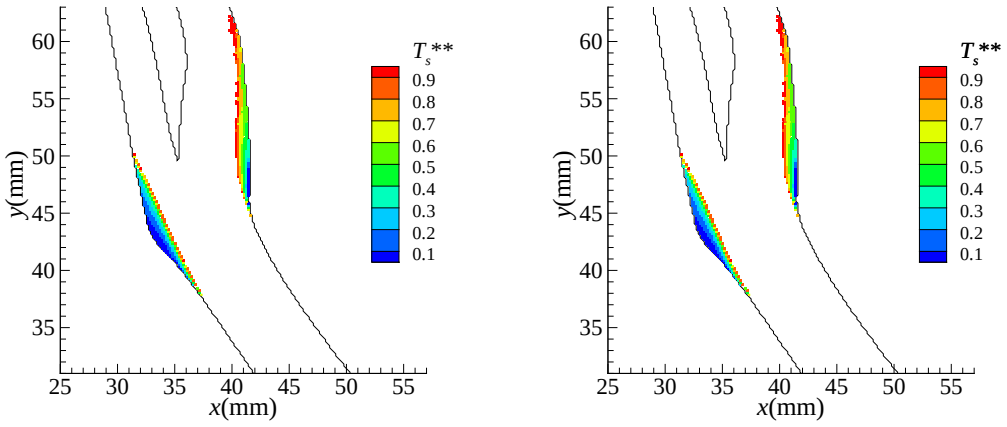

(a) $h = 0.1$ (b) $h = 0.3$

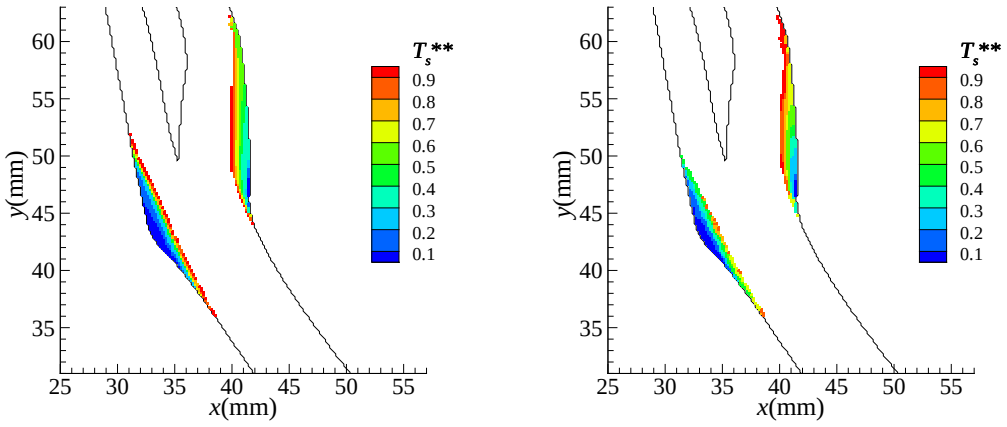

(c) $h = 0.5$ (d) $h = 0.7$

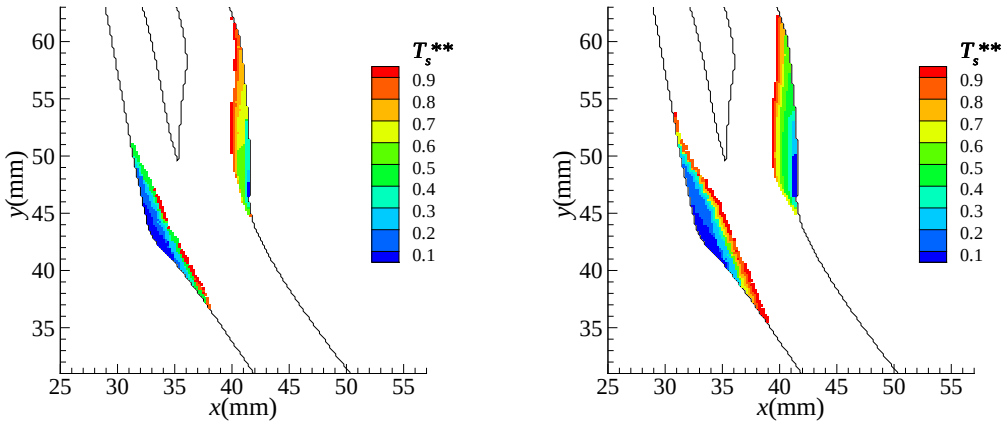

(e) $h = 0.9$ (f) $h = 1.0$

Figure 8.4: Stenosis development in terms of T_s^{**} for different values of h.

physical dimensions of h, e.g. as a fraction of the diameter.

The results in Figure 8.4 also indicates the similar behaviour of the model for the lower values of h. The stimulus for applying the normalisation T_s^{**} was to account for the different rate of stenosis development along the artery wall (in terms of T_s). It is clear from Figure 8.4 that this normalisation has not overcome the differences observed previously for the largest values of h. Thus it is clear that the limiting value observed in Figure 8.2 is a real phenomenon and that T_s and/or T_s^* are the appropriate measures for the evolution of the stenosis.

8.3 Applicable range of h

To better determine the cut-off value of h, ΔT_s^* is shown in Figure 8.5. This is calculated as the difference between the value of T_s^* found for $h = 0.5$ and that for $h = 0.1$, 0.3, 0.7, 0.9 and 1.0 in Figure 8.5 (a-e) respectively. Values are shown only for sites which were originally wet and which have been converted to dry sites in both simulations. While the differences are generally small in Figure 8.5 (a) and (b), there are a number of larger values. These are due to the stenosis developing in layers. There will be a number of sites close to the edge of each layer which will, at the end of the development of the layer, be wet for one value of h and dry for another - even when the difference between the geometry of the layers is so small as to have an insignificant effect on the wall geometry and the blood flow. Even though the difference between the stenosis development may be negligible between these cases, this explains the small number of points identified in Figure 8.5 (a) and (b) where ΔT_s^* is not small. These points do not overturn the view that the simulations with $h = 0.1$, 0.3 and 0.5 are effectively independent of h. Figure 8.5 (c) shows small, but slightly larger differences between the simulations. This suggests that $h = 0.5$ should be used as an upper limit, rather than $h = 0.7$. As expected Figure 8.5 (d) and (e) highlight the fact that $h = 0.9$ and 1.0

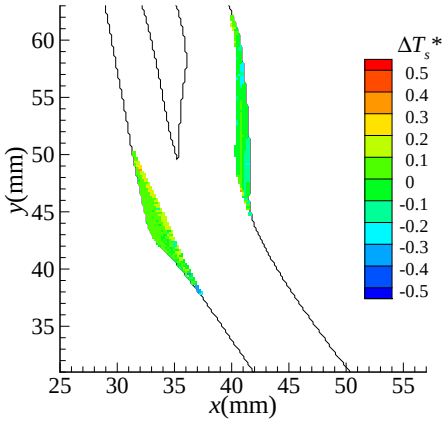

(a) $h = 0.1$

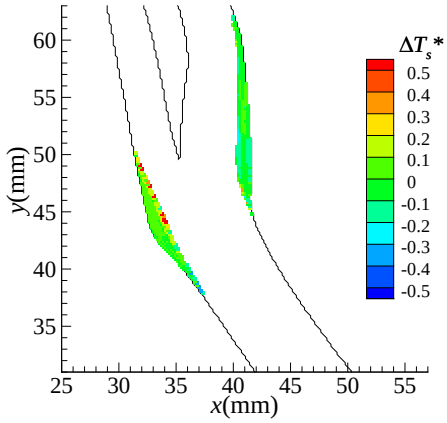

(b) $h = 0.3$

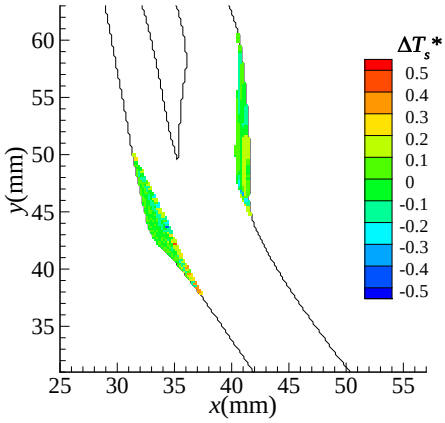

(c) $h = 0.7$

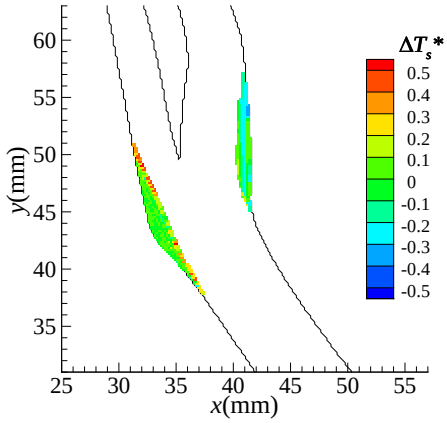

(d) $h = 0.9$

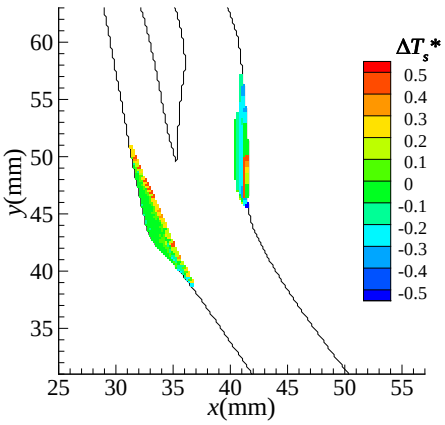

(e) $h = 1.0$

Figure 8.5: ΔT_s^* for different values of h.

are not suitable due to a lack of resolution.

8.4 Applicable range of w

The effect of w on the stenosis development was also considered. This is shown in Figure 8.6 for $w = 1$ and $w = 2$ for the case $h = 0.3$. Figure 8.6(a) and (b) depict

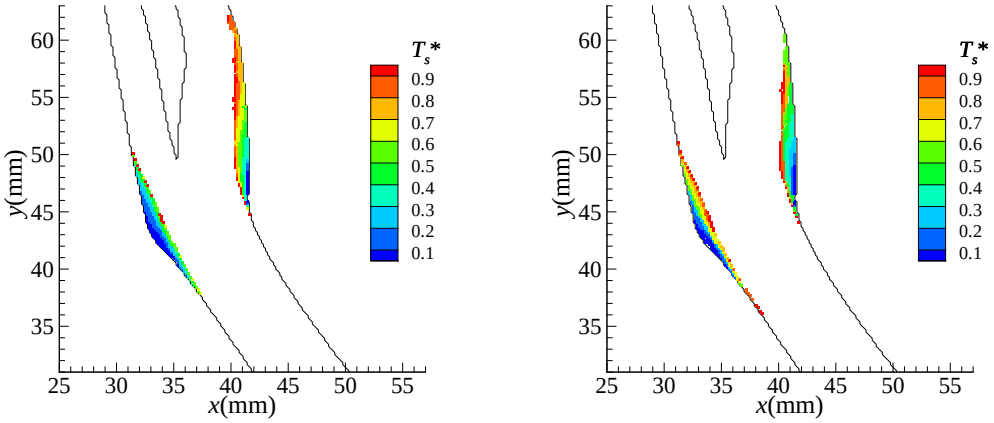

(a) $h = 0.3, w = 1$ (b) $h = 0.3, w = 2$

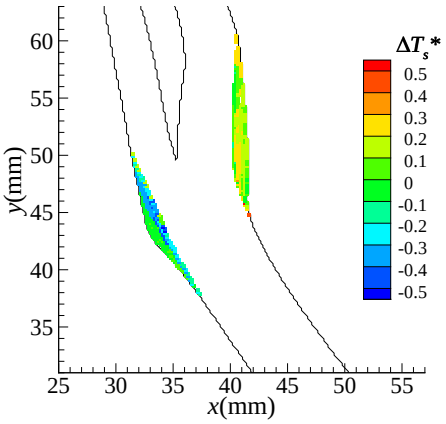

(c) $h = 0.3, \Delta T_s^* = T_s^*|_{w=2} - T_s^*|_{w=1}$

Figure 8.6: Comparison of $h = 0.3$ results for $w = 1$ and $w = 2$.

the evolution in terms of T_s^* and show a different behaviour for the two cases. These differences are highlighted in Figure 8.6(c) which shows the difference in T_s^* between $w = 1$ and $w = 2$, where the differences can be related to the layered

growth occurring at different rates. This behaviour is similar to that observed for the larger values of h and suggests that the resolution is not sufficient for $w = 2$ and that the model should be run with $w = 1$.

8.5 Flow profiles

The effect of the stenosis growth on the blood flow for a $T_s^* = 1$ stenosed geometry is shown, at the time of the peak velocity, Figure 8.7 and during the deceleration phase, Figures 8.8 and 8.9. The images on the left are for the healthy artery and the ones on the right are for the stenosed geometry at $T_s^* = 1$ with $h = 0.5$ and $w = 1$. Figure 8.7 depicts the velocity field at the peak in the cardiac cycle. The stenosed geometries show a higher velocity through both the internal and external carotid branches when compared to the healthy geometry, similarly to the 'high velocity jet' observed in the Doppler measurements of [197], as well as the PIV measurements of [198]. Vorticity, ($\boldsymbol{\omega}$) is determined by:

$$\boldsymbol{\omega} = \left(\frac{\partial u_y}{\partial x} - \frac{\partial u_x}{\partial y} \right) \tag{8.1}$$

and is presented in Figure 8.8 which shows significant vorticity developing in the healthy artery towards the bottom of both the ICA and ECA. This can be seen developing at the peak flow in Figure 8.8 (a) and fully developed flow in Figure 8.8 (c).

This is consistent with the MRI images and CFD results reported by [197–199]. It should be noted that [197–199] present results for a phantom; however, these were based on patient measurements and so provide a realistic geometry for a stenosed artery. Additionally, the authors considered a more severe stenosis on only one wall of the artery. The more severe stenosis results in an increased narrowing of the artery and so the jet nature of the flow is more pronounced. This

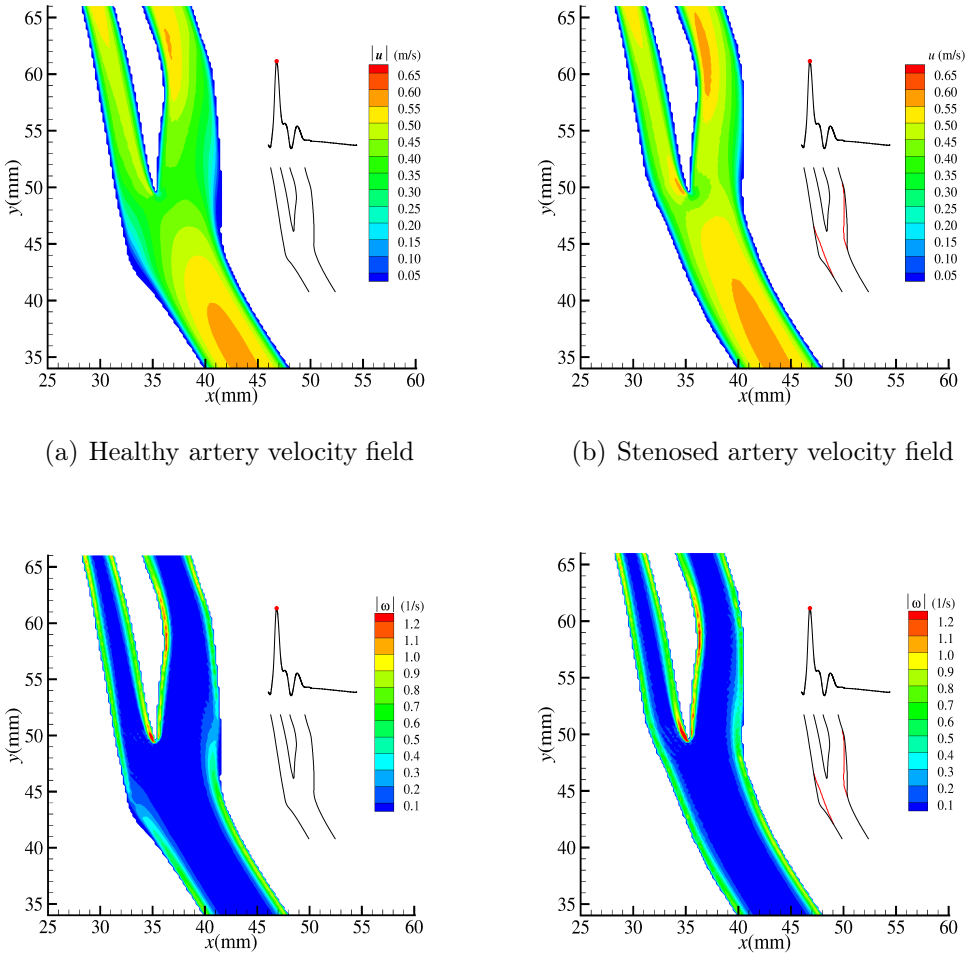

(a) Healthy artery velocity field

(b) Stenosed artery velocity field

(c) Healthy artery velocity field

(d) Stenosed artery vorticity field

Figure 8.7: Velocity (a and b) and vorticity ω, (c and d) for the healthy artery geometry (left column) and the stenosed geometry corresponding to $T_s^* = 1$ (right column) at peak flow. The driven pulse and the healthy geometry is also shown as an insert in each figure, where the pulse phase and the level of stenosis are depicted by the red dot and the red line respectively.

leads to vorticity/oscillations further from the bifurcation, which is not present here. Despite these differences, and the natural differences between individual artery geometries, the similarities suggest that the stenosis development model is predicting a realistic geometry for the stenosed artery.

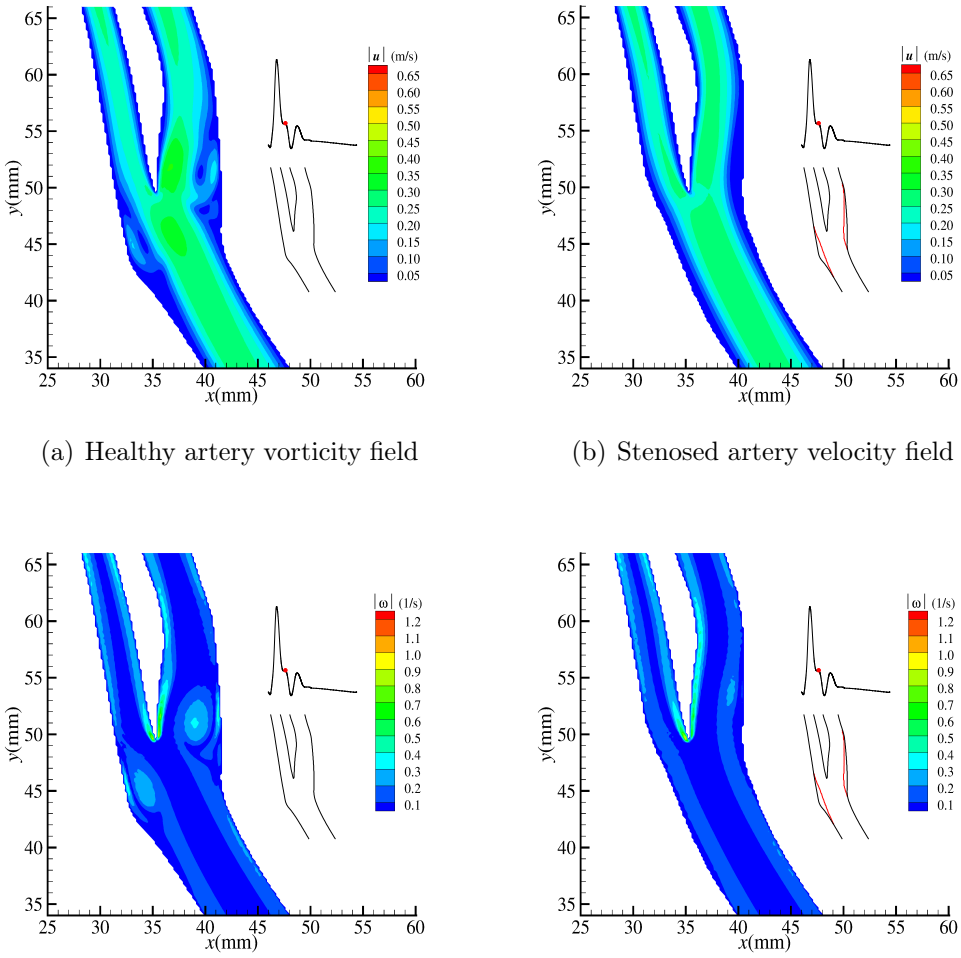

(a) Healthy artery vorticity field

(b) Stenosed artery velocity field

(c) Healthy artery vorticity field

(d) Stenosed artery velocity field

Figure 8.8: Velocity (a and b) and vorticity ω, (c and d) for the healthy artery geometry (left column) and the stenosed geometry corresponding to $T_s^* = 1$ (right column) during the deceleration phase of the cardiac pulse. The driven pulse and the healthy geometry is also shown as an insert in each figure, where the pulse phase and the level of stenosis are depicted by the red dot and the red line respectively.

8.6 Shear stress

Shear stress fields in Figures 8.9 reflect the regions of vorticity observed in Figures 8.8 (a) and (c) for the healthy artery, and their absence in the stenosed case. Figure 8.8 (b) also shows that, during peak flow, the region of highest shear stress

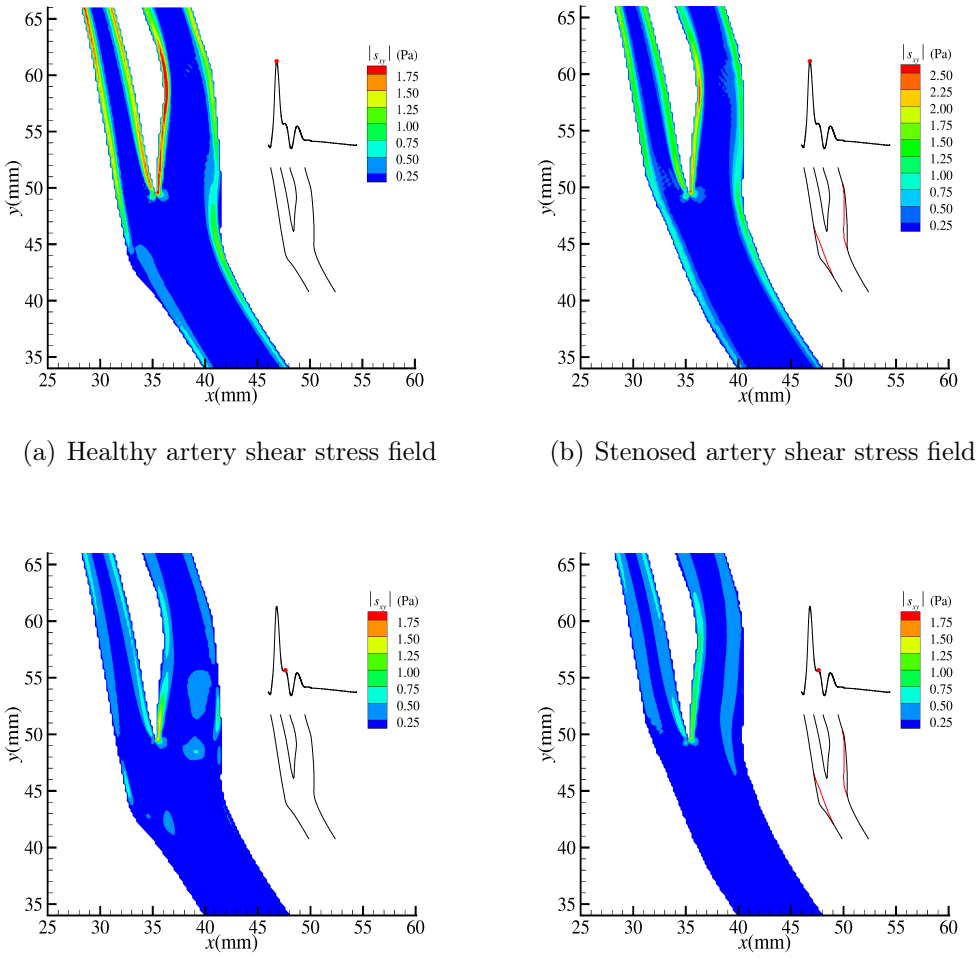

(a) Healthy artery shear stress field

(b) Stenosed artery shear stress field

(c) Healthy artery shear stress field

(d) Stenosed artery shear stress field

Figure 8.9: Shear stress (a and b) at the peak flow and during (c and d) the deceleration phase of the cardiac pulse for the healthy artery geometry (left column) and the stenosed geometry corresponding to $T_s^* = 1$ (right column). The driven pulse and the healthy geometry is also shown as an insert in each figure, where the pulse phase and the level of stenosis are depicted by the red dot and the red line respectively.

remains close to the wall in the stenosed region, in contrast to the behaviour for the healthy artery, shown in Figure 8.8 (a).

8.7 Conclusion

The stenosis development model has been evaluated for a range of the parameters h and w which are used to determine the extent of the stenosis growth at each stage. It was found that the model is effectively independent of h for $h \leq 0.5$, indicating that the model should be run in this range. A difference was also observed between w =1 and $w = 2$, suggesting that the model should be run with $w = 1$.

Different methods for describing the rate of development were also considered. The most appropriate measure was found to be T_s, the number of fluid sites converted to wall sites, or its normalised equivalent $T_s^* = T_s/T_{s\max}$.

Simulations were run within the identified range of h and w. The result showed similar features to experimental observations, suggesting the validity of the model.

Chapter 9

Effect of stenosis growth on the haemodynamics

The haemodynamics during stenosis development is studied for $h = 0.3$ and $w = 1$. This is done by considering how the flow changes with the development of the stenosis. In chapter 8 we saw that the stenosis occurs on the outer walls of the ECA and ICA in a series of layers which build up from the bottom tswowards the top of the artery. A layer can be comprised of a number of sub-layers. Table 9.1 displays in detail the development of the stenosis in terms of the number of consecutive site swaps on each wall. Also shown is the number of the periods N and total number of sites converted, T_s, at the time that the stenosis development jumps to the other wall. A layer is considered to be built up on either the ECA or ICA wall until a site swap occurs. A site swap is defined by more than four sites being converted on the opposite wall. Each layer in Table 9.1 is coloured according to:

- orange for $T_s \leq 20$ where there is no clear development on either wall
- yellow if the development is primarily on the ECA
- red if the development is primarily on the ICA.

Table 9.1: Details of the stenosis development on the ICA and ECA walls for $h = 0.3$ $w = 1$.

N	T_s	number of sites on ICA	number of sites on ECA
7	6	6	
25	14		8
26	15	1	
33	16		1
34	17	1	
45	19		2
53	20	1	
163	42		22
170	45	3	
287	68		23
288	69	1	
328	79		10
329	80	1	
510	119		39
512	121	2	
526	124		3
530	125	1	
542	127		2
547	128	1	
629	149		21
634	150	1	
786	185		35
792	186	1	
1056	238		52
1060	239	1	
1108	249		10
1463	322	73	
1579	344		22
1592	347	3	
1601	349		2
1607	350	1	
1621	353		3
1639	355	2	
1710	368		13
1765	381	13	
1855	408		27
2311	506	98	
2328	510		4
2332	511	1	
2348	513		2
3252	724	211	
3254	725		1
3335	739	14	

The details of each layer are summarised in Table 9.2, where each row corresponds to the formation of a layer. The geometry at the completion of each layer is

Table 9.2: Stenosis development in layers on the ICA and ECA for $h = 0.3$ $w = 1$

T	T_s	number of sites on ICA	number of sites on ECA
53	20	9	11
1108	249	12	217
1463	322	73	0
1710	368	6	40
1765	381	13	0
1855	408	0	27
3335	739	226	7

shown in Figure 9.1. The dot-dash line for $T_s = 20$ corresponds to the initial

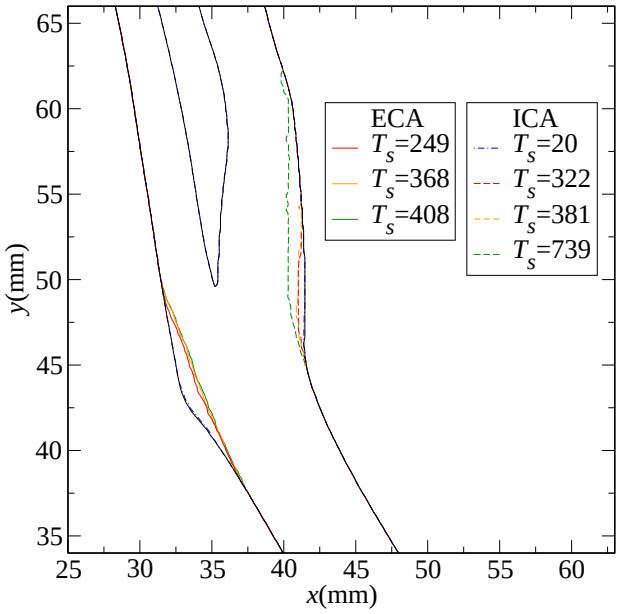

Figure 9.1: The development of the stenosis for $h = 0.3$ and $w = 1$. The stenosis geometry is shown at selected times corresponding to the final period during which each of the layer is developed.

phase during which no more than 8 sites are connected sequentially in a single wall. This line is barely distinguishable from the initial wall. The first ECA layer is formed by $T_s = 249$, as illustrated in the Tables 9.1 and 9.2. During its formation a number of sites are converted on the opposite wall. The first ICA

layer is formed by $T_s = 322$. Unlike the first ECA layer, this layer deposits in a continuous manner, as shown by Table 9.1. The second ECA layer is completed by $T_s = 368$ and the second ICA layer by $T_s = 381$. The third ECA layer is completed by $T_s = 408$ and the third ICA layer at $T_s = 739$ which corresponds to the end of the simulation. Figure 9.1 shows the development occurring on the ECA below the bifurcation, while in the ICA the stenosis occurs from slightly below the bifurcation and extends significantly in to the ICA.

9.1 Stenosis development and wall Haemodynamics

The haemodynamics in the wall regions are shown in Figures 9.2, 9.3, 9.4, in terms of $u^{(1)}$, WSS and $u_t^{(1)}$ on the ECA over the period of the pulse. This is shown for the healthy artery and also at the end of each layer development stage, as detailed in Table 9.2. Figures for $T_s = 20$ are not distinguishable from the healthy artery and so these are not included. The simulations of Figures 9.2, 9.3 and 9.4 (other than the magnitude) indicate that close to the wall the velocity is approximately tangential; and that the WSS, defined as WSS $= \mu(du_t/dn)$ is proportional to $u^{(1)}$. Figures 9.2, 9.3 and 9.4, parts (b)-(f) and the lower ($y < 38$mm) and upper ($y > 51$mm) regions of part (a) depict the presence of the velocity pulse shown in Figure 3.2. The region between $y = 38$mm and $y = 51$mm in part (a) corresponds to the vortex shown in Figure 7.1 which develops close to the peak velocity and is then transported down-stream by the blood. After the development of the first layer in the ECA, this vortex motion is no longer present. As shown in Figure 9.1, stenosis development on the ECA is limited after $T_s = 249$ which explains the similarity of parts (b)-(f).

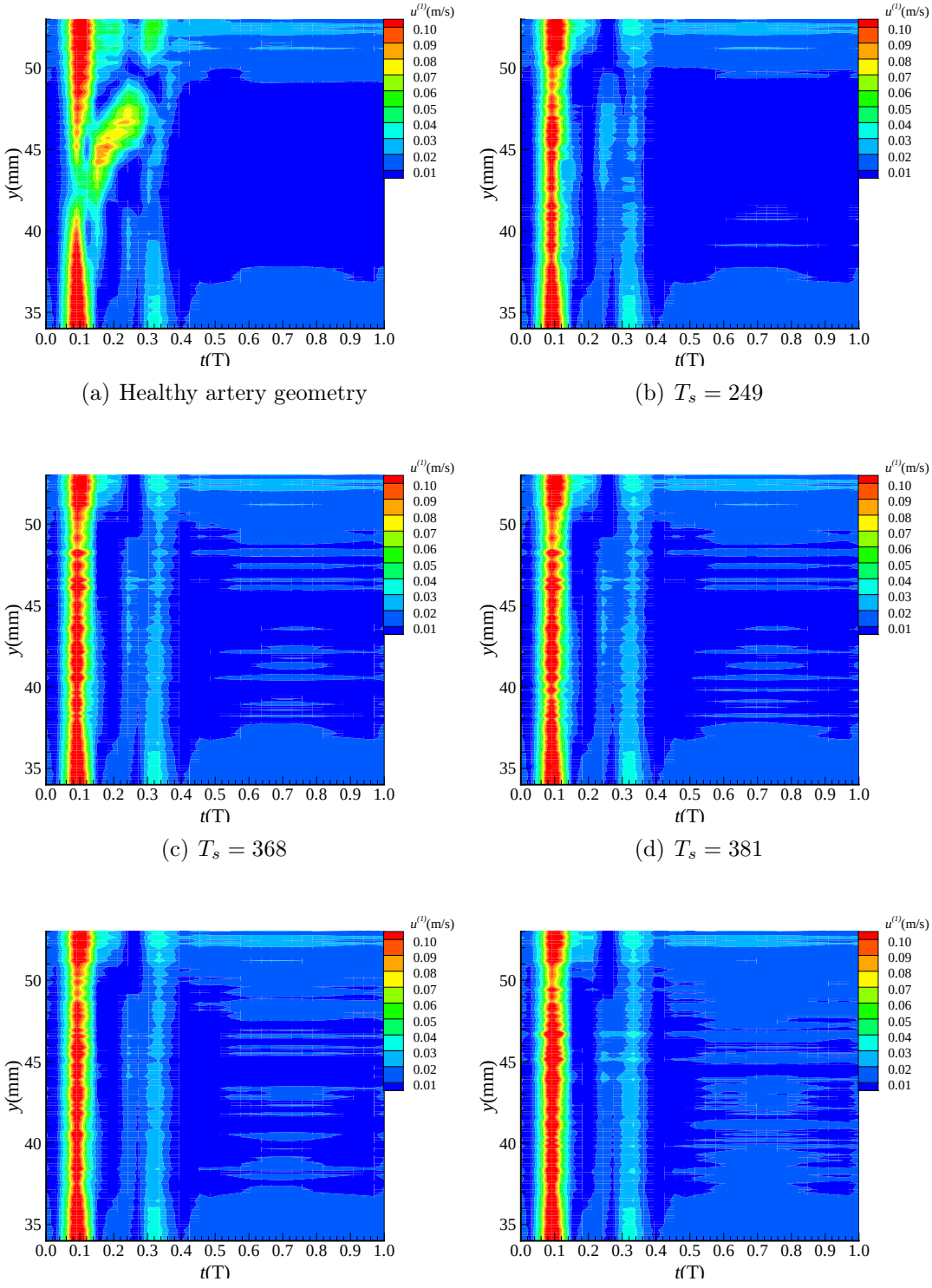

(a) Healthy artery geometry

(b) $T_s = 249$

(c) $T_s = 368$

(d) $T_s = 381$

(e) $T_s = 408$

(f) $T_s = 739$

Figure 9.2: Instantaneous $u^{(1)}$ on outer ECA over the cardiac pulse for (a) healthy artery, (b) $T_s = 249$, (c) $T_s = 368$, (d) $T_s = 381$, (e) $T_s = 408$ and (f) $T_s = 739$.

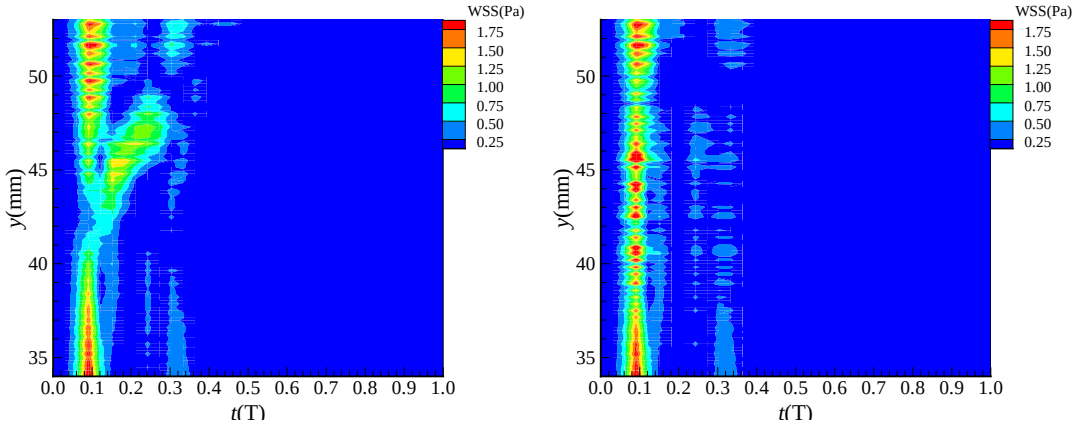

(a) Healthy artery geometry (b) $T_s = 249$

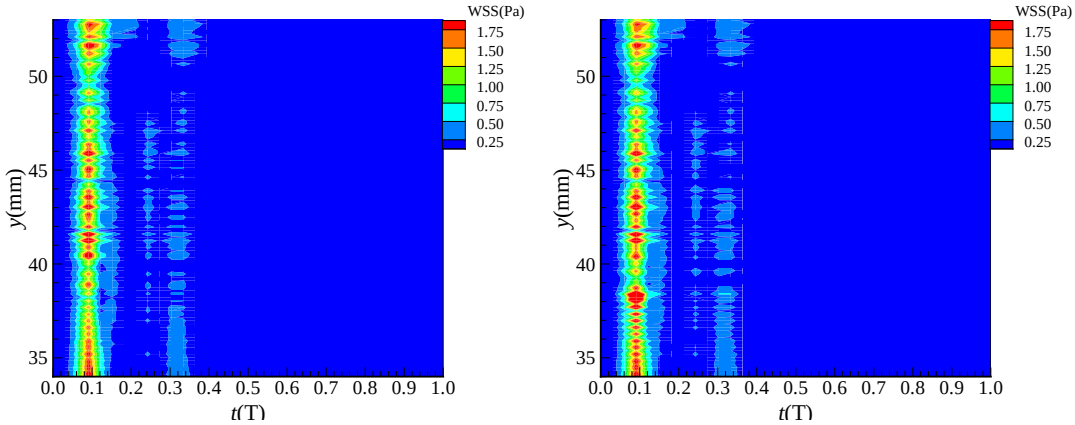

(c) $T_s = 368$ (d) $T_s = 381$

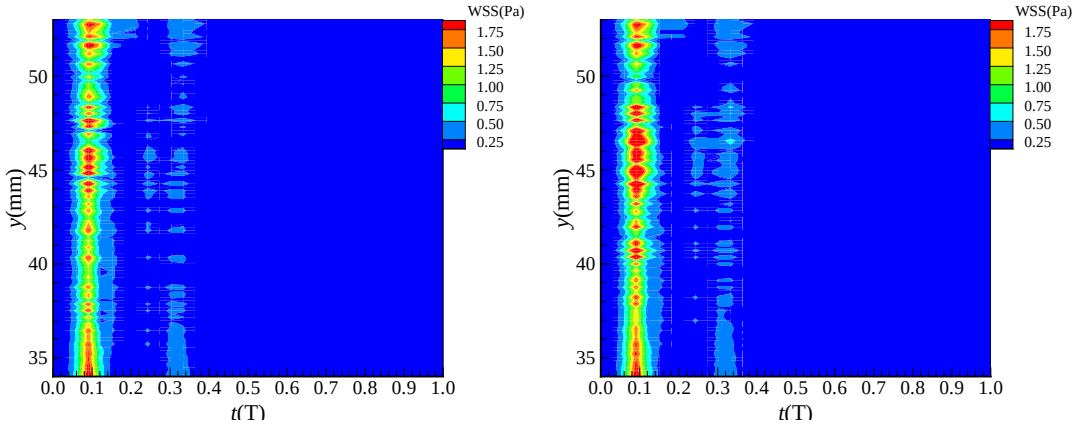

(e) $T_s = 408$ (f) $T_s = 739$

Figure 9.3: Instantaneous WSS on outer ECA over cardiac pulse for (a) healthy artery (b), $T_s = 249$, (c) $T_s = 368$, (d) $T_s = 381$, (e) $T_s = 408$ and (f) $T_s = 739$.

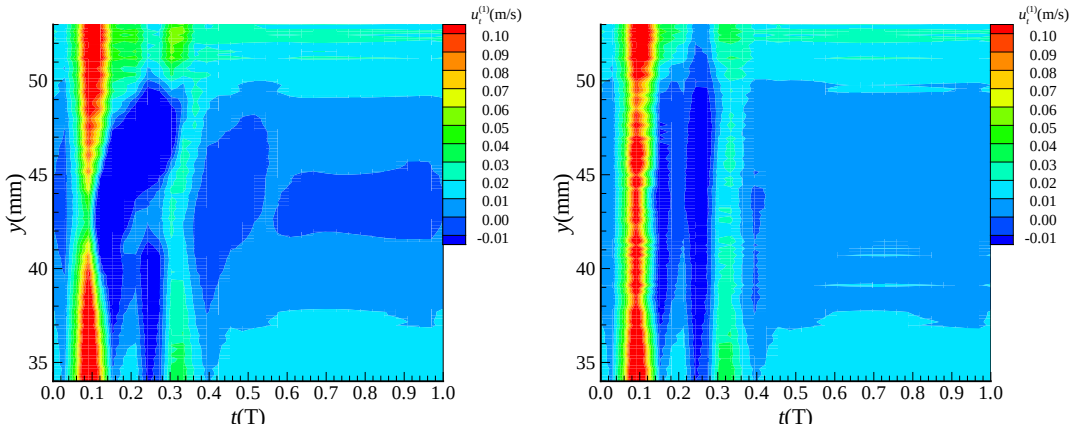

(a) Healthy artery geometry

(b) $T_s = 249$

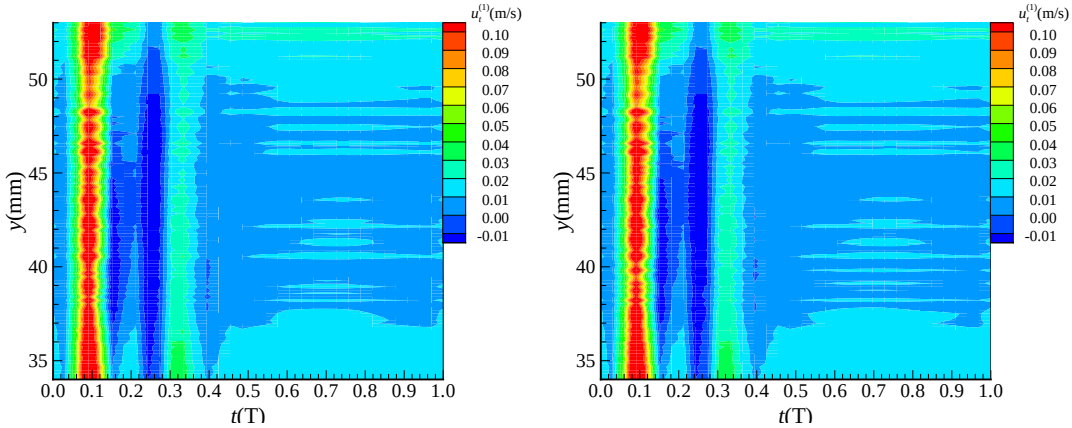

(c) $T_s = 368$

(d) $T_s = 381$

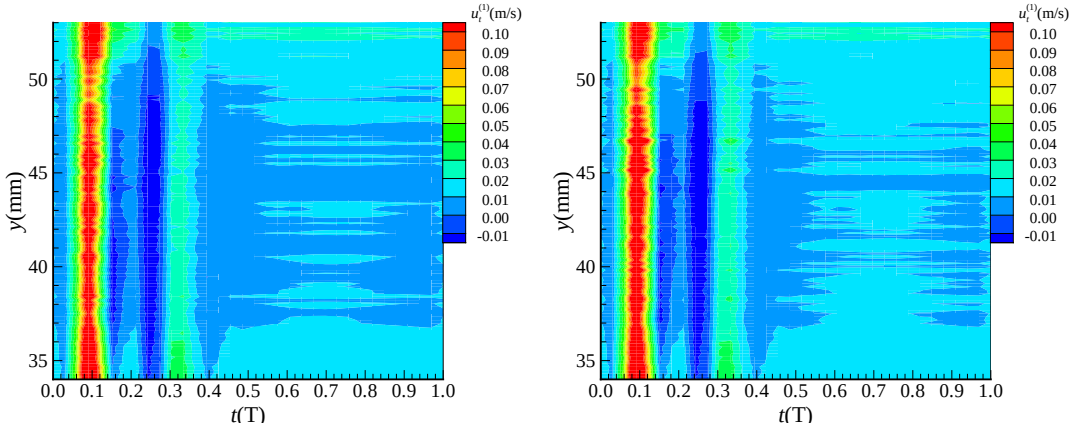

(e) $T_s = 408$

(f) $T_s = 739$

Figure 9.4: Instantaneous $u_t^{(1)}$ on outer ECA wall over cardiac pulse for (a) healthy artery, (b) $T_s = 249$, (c) $T_s = 368$, (d) $T_s = 381$, (e) $T_s = 408$ and (f) $T_s = 739$.

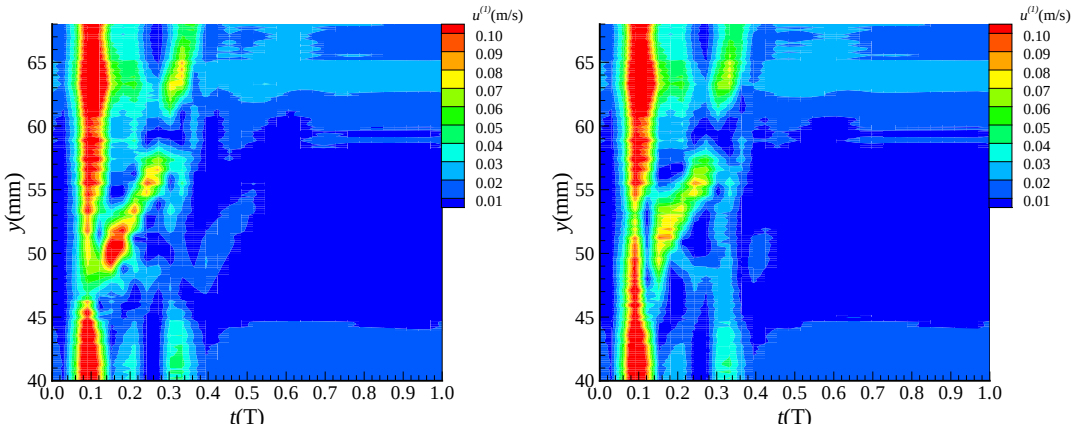

(a) Healthy artery geometry

(b) $T_s = 322$

(c) $T_s = 506$

(d) $T_s = 739$

Figure 9.5: Instantaneous $u^{(1)}$ on outer ICA wall over the cardiac pulse for (a) healthy artery, (b)$T_s = 322$, (c) $T_s = 506$ and (d) $T_s = 739$.

The haemodynamics are shown on the outer wall of the ICA in Figures 9.5, 9.6 and 9.7, over the period of the pulse. In Figures 9.5, 9.6 and 9.7, part (d) and the lower ($y < 45$mm) and upper ($y > 65$mm) regions of parts (a) - (c) the presence of the velocity pulse, shown in Figure 3.2, is depicted. The region between $y = 45$mm and $y = 65$mm in parts (a) - (c) corresponds to the vortex shown in Figure 7.1 which develops close to the peak velocity and is then transported downstream by the blood. At $T_s = 322$ (part (b)), after the formation of the first layer on the ICA, the effect of this vortex motion is only slightly reduced. By T_s

= 506, (part (c)), the effect is further reduced, but still significant. This indicates that the vortex is present on the ICA for longer into the stenosis development, when compared to the ECA. At $T_s = 739$ (part (d)) there is no clear evidence of the vorticity, which has been removed from the flow by the geometry change associated with the developing stenosis.

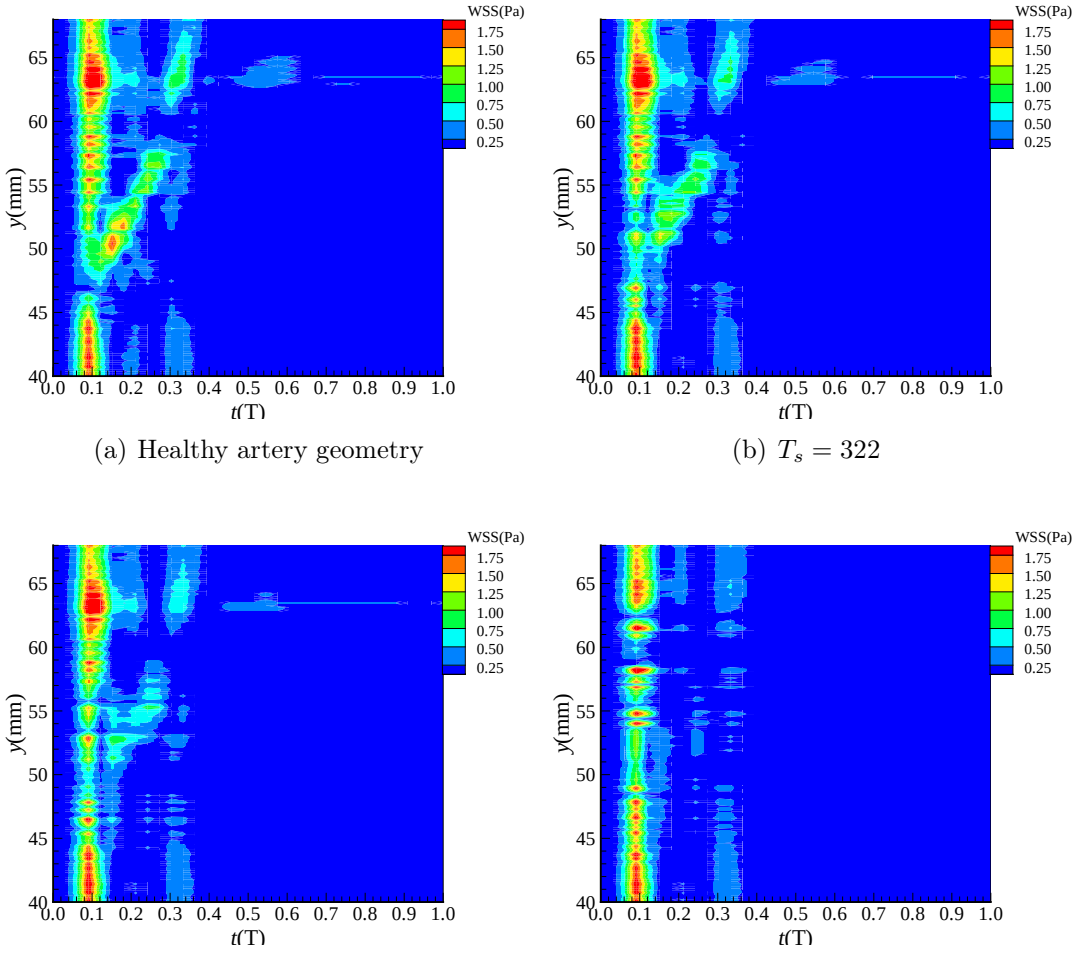

(a) Healthy artery geometry

(b) $T_s = 322$

(c) $T_s = 506$

(d) $T_s = 739$

Figure 9.6: Instantaneous WSS on outer ICA wall over the cardiac pulse for (a) healthy artery, (b)$T_s = 322$, (c) $T_s = 506$ and (d) $T_s = 739$.

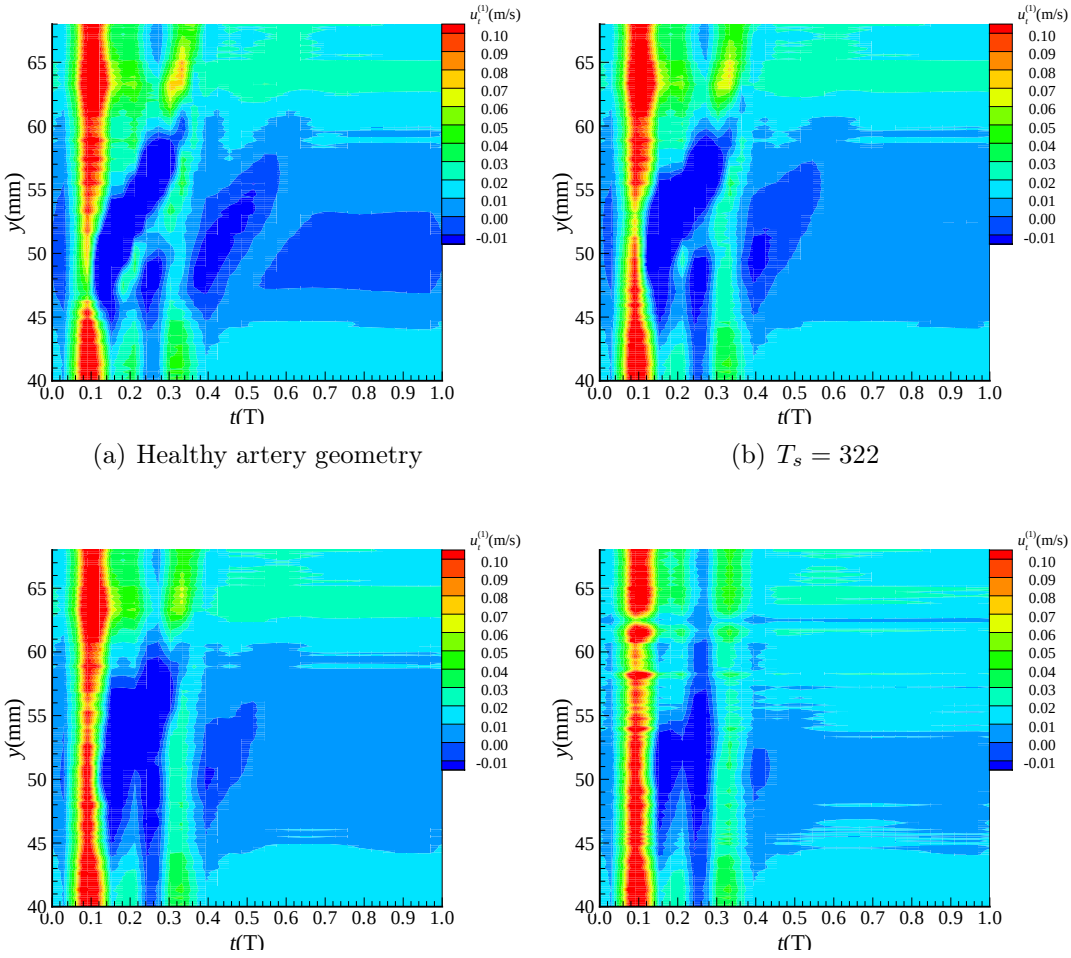

(a) Healthy artery geometry

(b) $T_s = 322$

(c) $T_s = 506$

(d) $T_s = 739$

Figure 9.7: Instantaneous $u_t^{(1)}$ at the outer ICA wall across the cardiac pulse for (a) healthy artery, (b)$T_s = 322$, (c) $T_s = 506$ and (d) $T_s = 739$.

9.2 Stenosis Development and time averaged wall haemodynamics

The effect of stenosis dependent on time averaged haemodynamic properties was also considered. The following quantities were considered:

$$\overline{u^{(1)}} = \frac{1}{T}\int_0^T u^{(1)} dt = \frac{1}{T}\int_0^T \left(\left(u_x^{(1)}\right)^2 + \left(u_y^{(1)}\right)^2\right)^{1/2} dt; \tag{9.1}$$

$$\overline{u_t^{(1)}} = \frac{1}{T}\int_0^T u_t^{(1)} dt; \tag{9.2}$$

$$\text{TAWSS} = \frac{1}{T}\int_0^T \text{WSS} dt; \tag{9.3}$$

OSI, defined by equation (5.1); RRT, defined by equation (5.2); the Reverse Flow Index, RFI, representing the fraction of the period where $u_t^{(1)}$ is negative; and O:WS = OSI/TAWSS. In terms of RRT, the constant of proportionality was found by normalising with respect to the value three diameters upstream from the bifurcation. Figures 9.10 and 9.11 show the quantities for the ICA. The white vertical lines drawn on the contour, represent the layer completion times shown in Figure 9.1 and Table 9.2. The dot-dash, the solid and the dashed lines correspond to the initial mixed layer for $T_s \leq 20$; ECA and ICA layers respectively. The non-vertical white lines indicate the upper and lower extremes of the stenosis on the wall. The black curve is a contour line for $u^{(1)}$ which has been smoothed by a double pass through a smoothing filter. Each pass of the filter shifts the value to halfway between its initial value and the average value of its neighbours. Although the black contour has been derived from smoothed data, none of the other data has been smoothed.

Figure 9.8 (a) shows for the ECA a region of low near-wall velocity, in the healthy artery ($T_s = 0$) in the range 38 mm $< y <$ 44 mm. During the initial mixed layer $T_s \leq 20$ the stenosis starts to develop on the ECA in this region. By $T_s = 20$ it has expanded downstream to approximately the upper extreme of the low-velocity region identified at $T_s = 0$. It also extends slightly upstream, but not to the level of the initial low-velocity region. For $20 \leq T_s \leq 249$ the stenosis develops predominantly on the ECA, see Table 9.2 and Figure 9.1. During this time the stenosis extends downstream, beyond the limits of the near-wall velocity region in the healthy artery. As the position of the stenosis extends, a region of low near-wall velocity extends on either side of the downstream tip. Once the stenosis

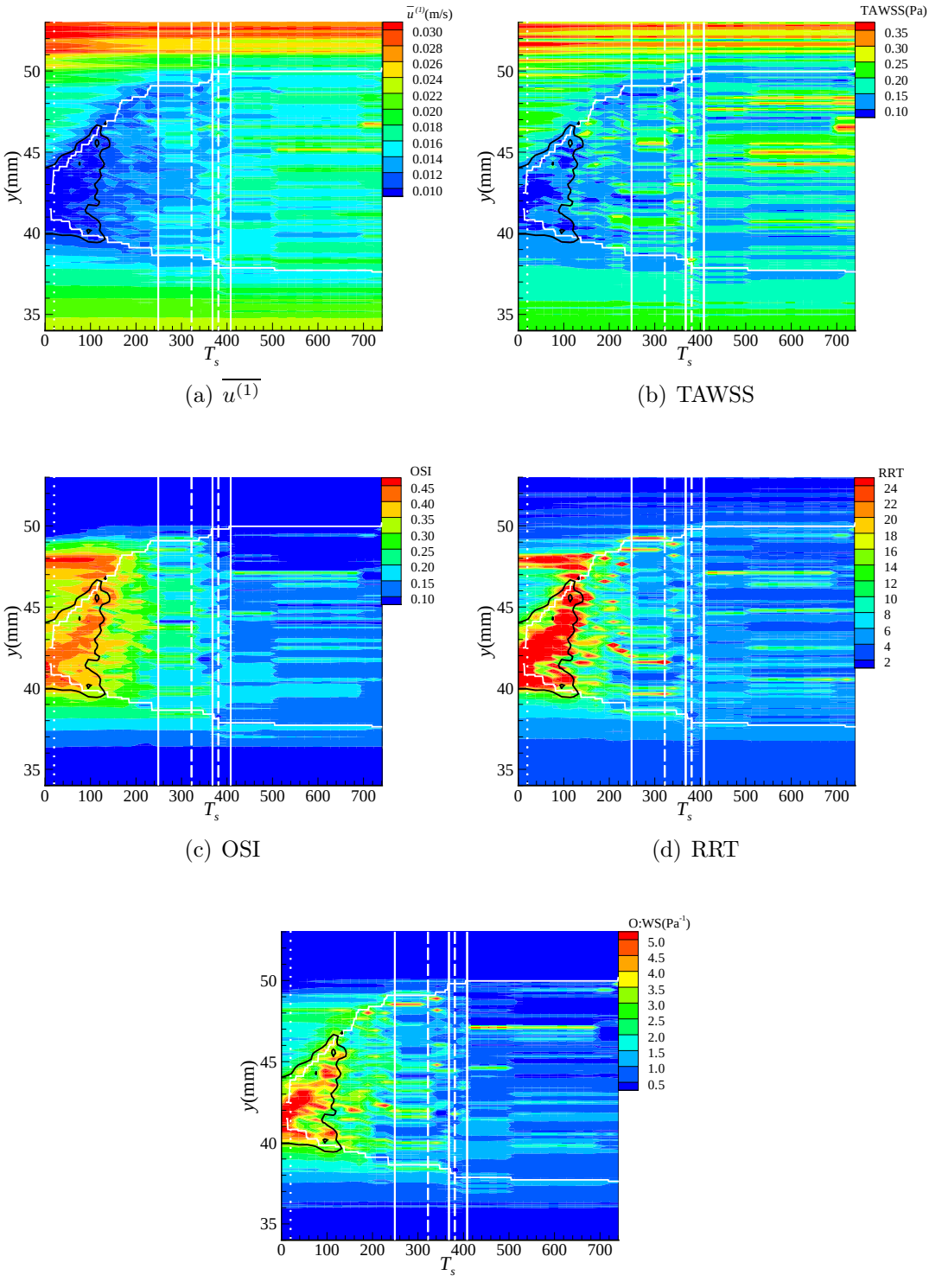

(a) $\overline{u^{(1)}}$ (b) TAWSS

(c) OSI (d) RRT

(e) O:WS

Figure 9.8: (a) $\overline{u^{(1)}}$, (b) TAWSS, (c) OSI, (d) RRT and (e) O:WS on the outer wall of the ECA over the development of the stenosis.

has developed through a particular y-position, the near-wall velocity gradually reduces to close to its original value, e.g. at $y = 47$ mm, $\overline{u^{(1)}}$ remains relatively constant until $T_s \simeq 100$. Then the near-wall velocity decreases to a minimum at $T_s \simeq 118$, close to when the stenosis reaches this point ($y = 47$ mm). The velocity then gradually increases and reaches a value close to its original for $T_s > 250$, as shown in Figure 9.8 (a). During the first ECA layer, the stenosis also expands upstream, although at a slower rate. By $T_s = 249$, it has developed to around the bottom of the initial low velocity region. We note that for $T_s < 150$, the white line representing the extent of the stenosis is similar to the black curve which is the low average velocity contour. The next layer $249 < T_s \leq 322$ develops solely on the ICA and this has no significant effect on $\overline{u^{(1)}}$ in the outer wall of the ECA. There are two further periods $322 \leq T_s \leq 368$ and $381 \leq T_s \leq 408$ where the stenosis develops on the ECA. During these periods the stenosis expands only slightly, but the effect on $\overline{u^{(1)}}$ is more significant in that by $T_s = 408$ the initial low average near-wall velocity, at $T_s = 0$, and the subsequent expanded region of low $\overline{u^{(1)}}$ are substantially removed and $\overline{u^{(1)}}$ is relatively constant for 35 mm $< y <$ 50 mm at $T_s = 739$.

The TAWSS in Figure 9.8 (b) demonstrates simillar behaviour as expected. Figures 9.8 (c), (d) and (e) show the OSI, RRT and O:WS, also on the ECA. These figures show considerable similarity to Figure 9.8 (a), except for the inverse relationship where the quantities plotted here are maximum where $\overline{u^{(1)}}$ was minimum. In particular the $\overline{u^{(1)}}$ contour (black curve), in each case encloses a region where the plotted quantity is large. Additionally, as the stenosis expands downstream, there is a region where each of OSI, RRT, O:WS reaches a maximum before dropping to close to its original value (although the value ultimately drops to a somewhat lower value). This is shown in Figure 9.8 (c), (d) and (e). At $T_s = 739$ the stenosis has developed in such a way that the areas of high OSI, RRT, O:WS are no longer evident.

There is one significant difference between Figures 9.8 (c), (d) and (e) and the time-averaged near-wall velocity and TAWSS plots (Figures 9.8 (a), and (b)). In the healthy case ($T_s = 0$), there are secondary peaks in OSI and RRT around $y = 48$mm. This is also evident in Figure 9.8 (e), but less prominent, because it is present in OSI, but not TAWSS. This secondary peak remains approximately constant until the developing stenosis reaches its location. Once the stenosis has developed past this point the OSI and RRT reduce in a simpler manner to the (increasing) $\overline{u^{(1)}}$ in Figure 9.8 (a).

At $T_s = 408$, the end of the third ECA layer, there is no more significant development of the stenosis on this wall. The upstream extent of the stenosis corresponds to the lower limit of low $\overline{u^{(1)}}$ and TAWSS / high OSI, RRT and O:WS regions observed at $T_s = 0$, for the healthy artery. Downstream the stenosis has extended beyond the initial low $\overline{u^{(1)}}$ and TAWSS to slightly beyond the upper limit of the healthy artery, secondary peak in OSI, RRT, O:WS. Figures 9.9 (a) and (b) show $\overline{u_t^{(1)}}$ and RFI. These are clearly inverse properties, with large RFI when there is a significant amount of reversed flow and $u_t^{(1)}$ is negative. Both figures indicate a significant trend of reverse flow in the healthy artery at $T_s = 0$ such that the average value of $\overline{u_t^{(1)}}$ is negative for 42mm $\leq y \leq$ 47mm. Comparing the contours in Figure 9.9 (a) with the black curve which was derived from a low $\overline{u^{(1)}}$ contour, it is clear that within the black contour $\overline{u_t^{(1)}}$ is small; however there is a region downstream of the black contour where $\overline{u_t^{(1)}}$ is equally small and predominantly negative. The upper limit of that low $\overline{u_t^{(1)}}$ region corresponds to the secondary part of OSI, RRT in Figures 9.8 (c) and (d) which was observed to be associated with the downstream limit of the stenosis progression. This is also related to the position of the vortex which forms in the healthy artery during the deceleration phase, as observed in Figure 7.1. Figures 9.10(a)-(e) and 9.11 (a), (b) show the same properties as Figures 9.8(a)-(e) and 9.9 (a), (b), but for ICA. Here the black, low $\overline{u^{(1)}}$, contour encloses a number of regions; however, a

larger region, encompassing the low $\overline{u^{(1)}}$ region, can be considered. Although the stenosis develops on the ICA in two main layers corresponding to $249 < T_s \leq 322$ and $408 < T_s \leq 739$, there is also some significant development for $T_s < 259$ as is evident on the Table 9.2 and Figure 9.10 (a). Although the stenosis extends for approximately 4mm along the ICA at $T_s = 259$, it represents a thin layer, see Figure 9.1, and has had little effect on the time averaged values on the outer ICA wall, see Figures 9.10(a)-(e) and 9.11 (a), (b). The stenosis development on the ICA shows many similar features with the development on the ECA:

1. Development starts in a region of low $\overline{u^{(1)}}$ (Figure 9.10(a))

2. The stenosis progresses only slightly upstream and is limited by the extent of the initial low $\overline{u^{(1)}}$ region.

3. The stenosis progresses significantly further upstream. A low $\overline{u^{(1)}}$ region develops around the downstream limit of the stenosis. This increases once the stenosis tip has moved through the region (although not as rapidly as for the ECA).

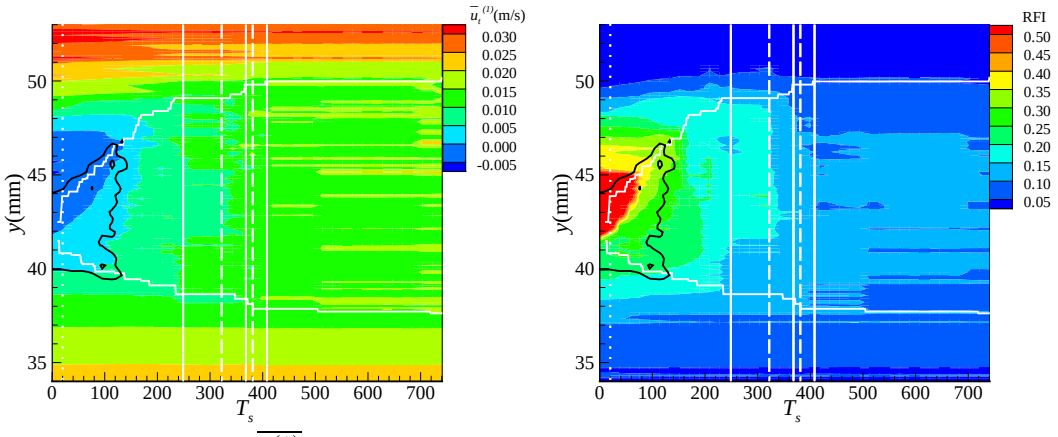

(a) $\overline{u_t^{(1)}}$ (b) RFI

Figure 9.9: (a) $\overline{u_t^{(1)}}$ and (b) RFI on the outer wall of the ECA over the development of the stenosis.

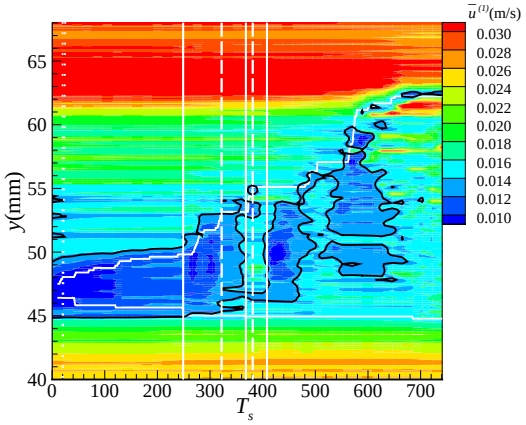

(a) $\overline{u^{(1)}}$

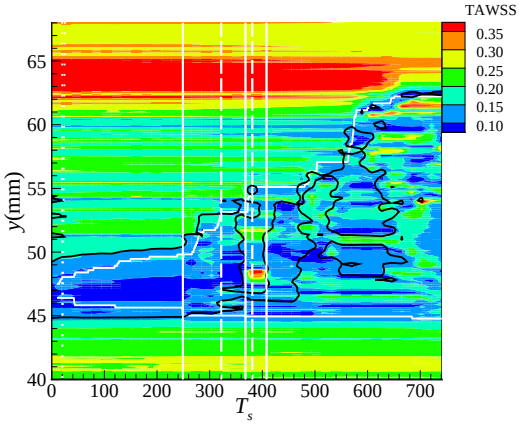

(b) TAWSS

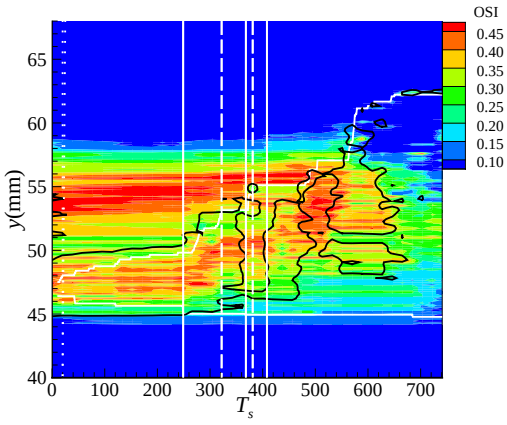

(c) OSI

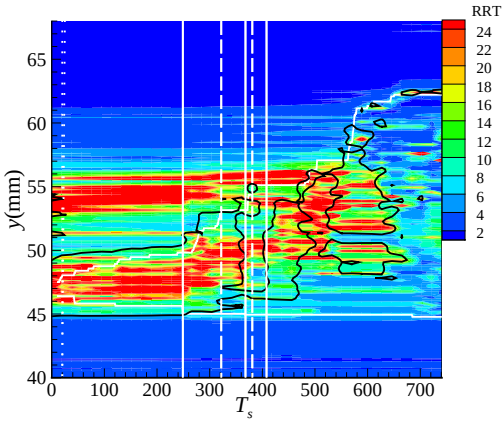

(d) RRT

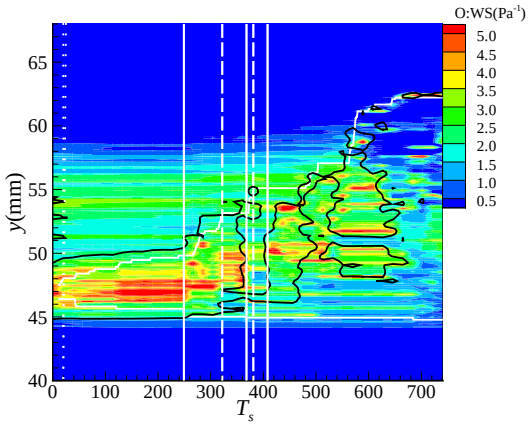

(e) O:WS

Figure 9.10: (a) $\overline{u^{(1)}}$, (b) TAWSS, (c) OSI, (d) RRT, (e) O:WS on the outer wall of the ICA over the development of the stenosis.

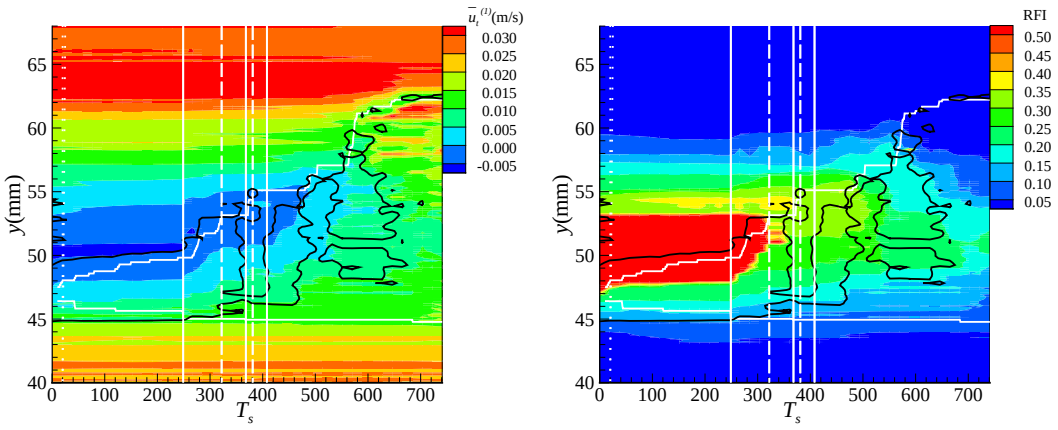

(a) $\overline{u_t^{(1)}}$ (b) RFI

Figure 9.11: (a)$\overline{u_t^{(1)}}$ and (b) RFI on the outer wall of the ICA over the development of the stenosis.

4. At $T_s = 739$, the initial low-average wall velocity region is no longer present.

5. The TAWSS (Figure 9.8(b)) replicates $\overline{u^{(1)}}$ (Figure 9.8(a)).

6. OSI (Figure 9.10(c)), RRT (Figure 9.10(d)) and O:WS (Figure 9.10(e)) displays the same features as $\overline{u^{(1)}}$ and TAWSS (in the inverse sense).

7. OSI (Figure 9.10(c)), RRT (Figure 9.10(d)) and O:WS (Figure 9.10(e)) also contain a secondary peak, downstream the region of low $\overline{u^{(1)}}$. This also corresponds to the vortex motion in this region, as shown in Figure 7.1.

8. There is a region of significant reverse flow downstream of the low $\overline{u^{(1)}}$ region indicated by negative values for $\overline{u_t^{(1)}}$ (Figure 9.11 (a)) and RFI (Figure 9.11 (b)).

One significant difference was observed between stenosis development on the ICA and the ECA. On the ICA, the stenosis develops downstream beyond the second peak in OSI and RRT. When this happens the rate of stenosis progression along the artery wall reduces. As the stenosis develops through this region it maintains a region of low $\overline{u^{(1)}}$ (Figure 9.10(a)), low TAWSS (Figure 9.10(b)), high OSI

(Figure 9.10(c)), high RRT (Figure 9.10(d)), high O:WS (Figure 9.10(e)) and low $\overline{u_t^{(1)}}$ (Figure 9.11 (a)). RFI is not high here (Figure 9.11 (b)) indicating, that although the velocities are reduced, the flow does not reverse.

Although the developing stenosis does not affect the geometry of the inner ICA or ECA walls, the near-wall flow is influenced by what is occurring on the outer walls. This is shown in Figures 9.12 (a),(b), (c) and (d), which depict $\overline{u^{(1)}}_{\mathrm{f}}$ and $\mathrm{RRT}_{\mathrm{f}}$, where $X_{\mathrm{f}}(y, T_s) = X(y, T_s)/X(y, 0)$. Figures 9.12 (a) and (b) are for

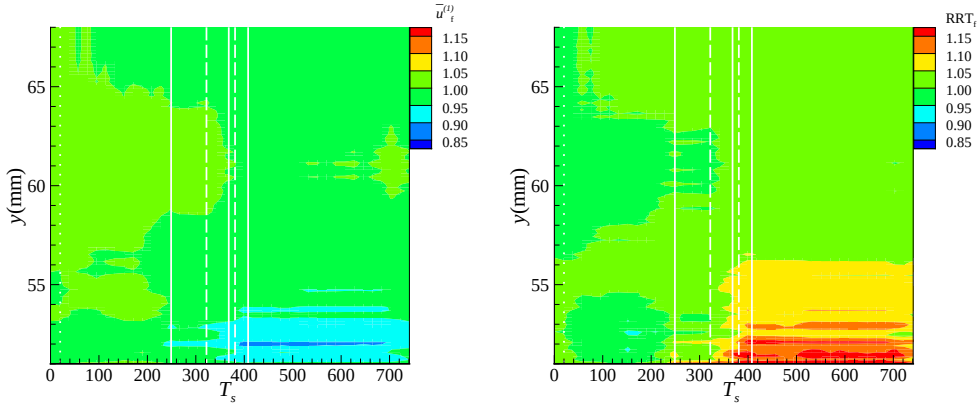

(a) $\overline{u_t^{(1)}}_{\mathrm{f}}$ for ECA (b) $\mathrm{RRT}_{\mathrm{f}}$ for ECA

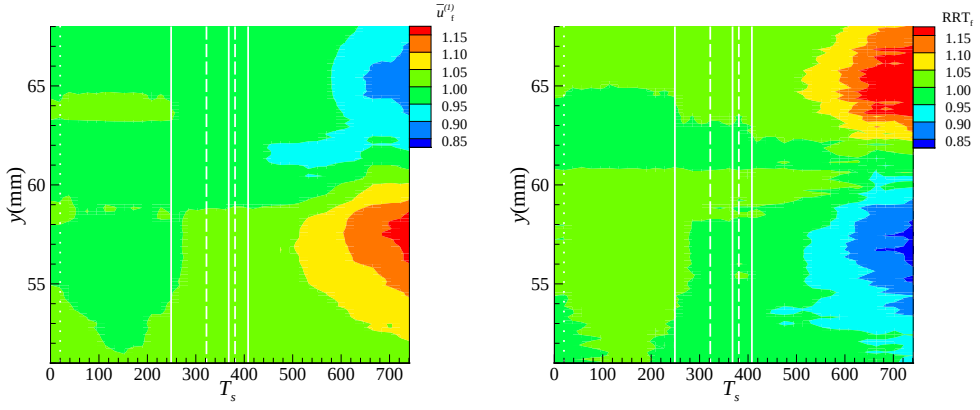

(c) $\overline{u_t^{(1)}}_{\mathrm{f}}$ for ICA (d) $\mathrm{RRT}_{\mathrm{f}}$ for ICA

Figure 9.12: (a) $\overline{u^{(1)}}_{\mathrm{f}}$ and (b) $\mathrm{RRT}_{\mathrm{f}}$ on the inner walls of the ECA and (c) and (d) on the inner walls of the ICA over the development of the stenosis.

the ECA. There is a slight increase of less than 3% in $\overline{u^{(1)}}$ on this wall, as the initial ECA layer is developing; however this is a temporary feature and is not

present at $T_s = 368$ when the stenosis in the ECA is almost completely developed. After this time, as the stenosis is developing predominantly on the ICA, there is a slightly more significant region where $\overline{u^{(1)}}$ is reduced by up to around 10 % for $y < 55$mm. $\mathrm{RRT_f}$ indicates the same features, but in an inverse sense.

On the ICA, figures 9.12 (c) and (d), there is little change until $T_s > 408$, corresponding to the final layer development on the ICA. It is during this time that substantial stenosis development occurs on the outer wall of the ICA, see Figure 9.1. This results in an increase of up to 15% in the near wall velocity in the lower part of the inner ICA wall ($y < 60$ mm). This represents an increased velocity due to the decrease in the artery diameter in this region (Figure 9.1). For $y > 60$ mm there is an equally large reduction in the near wall velocity, suggesting the stenosis development is producing a meandering jet in the ICA affecting the downstream haemodynamics. Similar features are observed in the RRT, but in a negative sense.

9.3 Conclusions

The stenosis growth model has been successfully applied to investigate how the haemodynamic properties at the wall change as the stenosis develops. The near wall velocity and the WSS on both the outer ICA and ECA walls were considered in the region where the stenosis develops. As the stenosis grows it fills in the region where low velocity and vortex motion is observed in the healthy artery. As the stenosis develops it was seen to progress mainly downstream - as this happens a region of low TA velocity and low TAWSS is observed around the downstream tip. The OSI and RRT show similar behaviour except that they have high values where $\overline{u^{(1)}}$ and TAWSS are low. In addition to peaking at the region of the wall where the stenosis is expanding, the OSI and RRT also identify an additional region where their values are initially high and which can be associated with the

region where vortex motion is observed in the healthy artery.

Although the stenosis did not develop on the inner walls of the ECA and the ICA, the near wall haemodynamics were also seen to be affected. This was particularly true of the ICA where the stenosis develops further into the artery. Here the near wall haemodynamics were consistent with a meandering jet-like flow developing with the stenosis.

Chapter 10

Alternative haemodynamic markers for stenosis development

The position on the artery wall where the stenosis development occurred was determined in chapter 9 by finding the position where the time averaged velocity magnitude calculated 1 lu from the wall, $u^{(1)}$, has its minimum value. In this chapter, we consider alternative markers, will develop based on the local haemodynamics, for determining the wall position where the stenosis forms. The additional selected criteria selected here, were $\overline{u^{(1)}}$; $\overline{\left|u_t^{(1)}\right|} = \int_0^T \left|u_t^{(1)}\right| dt/T$; TAWSS; RFI; SI, defined as the fraction of the period during which $u^{(1)}$ is less than 1% of the peak pulse velocity; RRT; TAD_{II}; OSI; and O:WS.

10.1 Stenosis development

The development of the stenosis is shown in Figures 10.1 and 10.2. In Figure 10.1 the development is seen to occur in layers, similar to that observed in Figure 9.1. Figure 10.2 shows the development in layers in terms of the normalised parameter T_s^* representing the number of sites converted from wet to dry, normalised by the length of each simulation: $T_s = 747$. All the simulations, except for the one

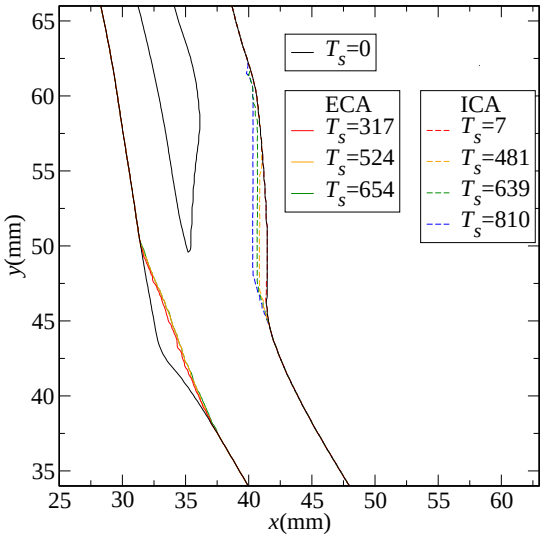

(a) $\overline{u^{(1)}}$

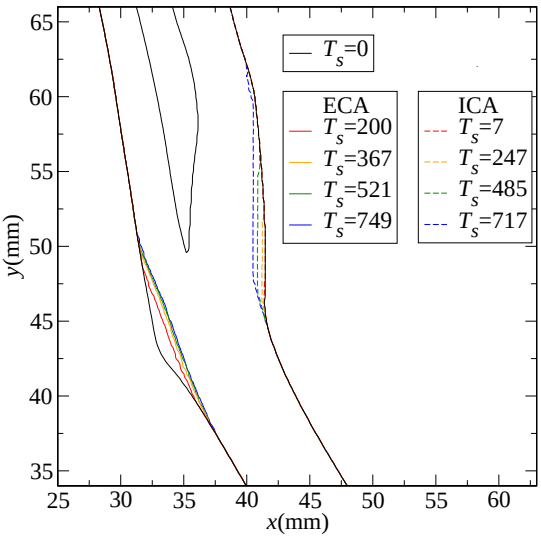

(b) $\left|\overline{u_t^{(1)}}\right|$

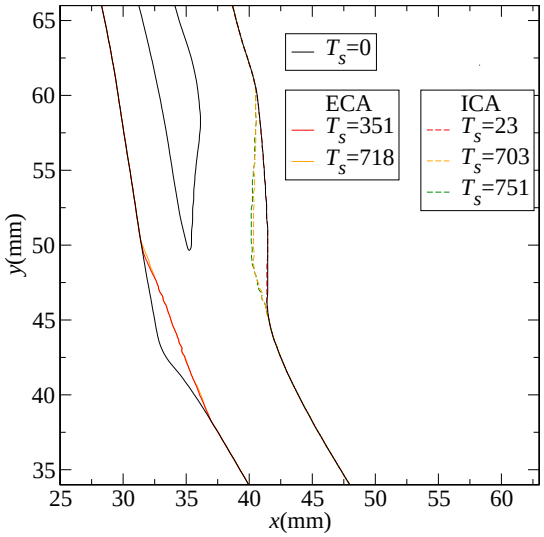

(c) TAWSS

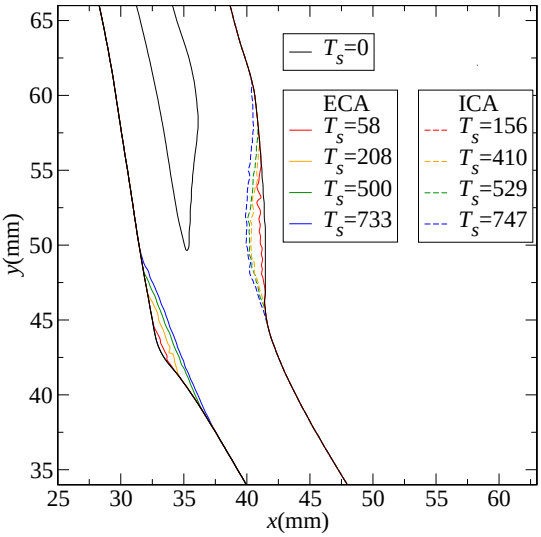

(d) RFI

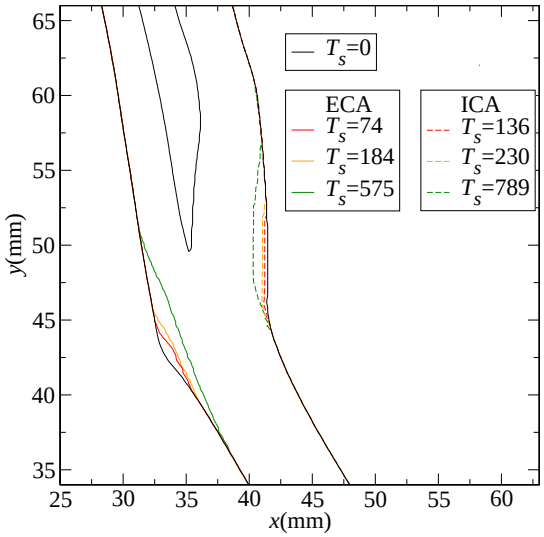

(e) SI

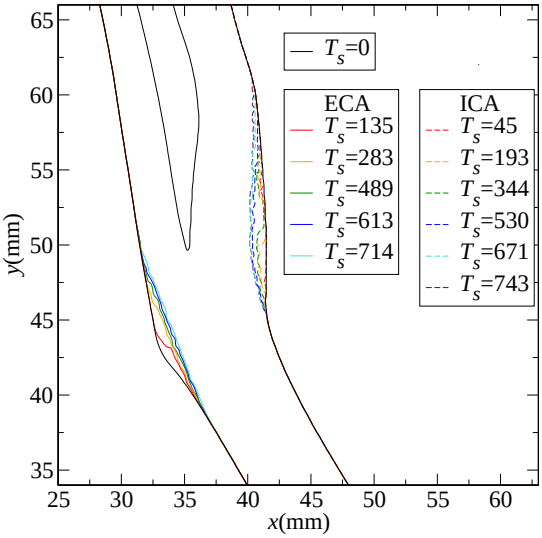

(f) RRT

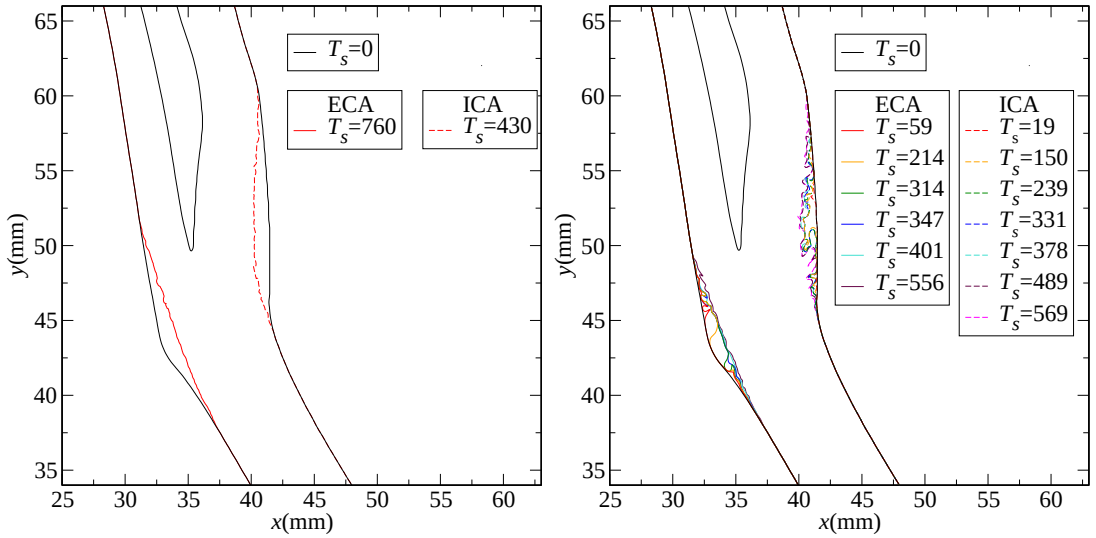

(g) TAD_{II}

(h) OSI

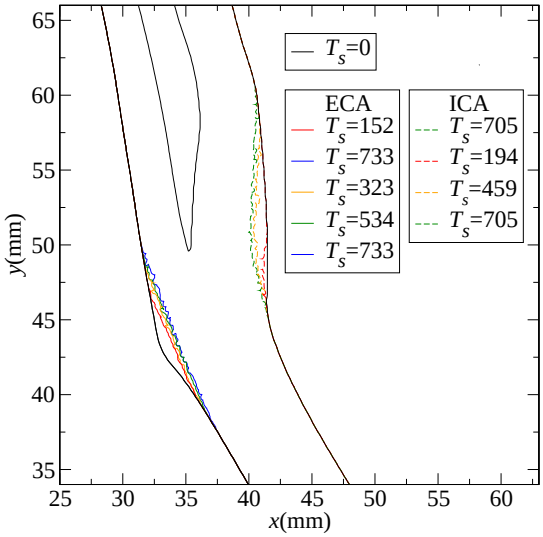

(i) O:WS

Figure 10.1: Stenosis development in layers when the position of the development is determined by for triggers (a) $\overline{u^{(1)}}$, (b) $\overline{|u_t^{(1)}|}$, (c) TAWSS, (d) RFI, (e) SI, (f) RRT, (g) TAD_{II} (h) OSI and (i) O:WS

based in the OSI, show a similar final geometry for the stenosed artery, which is consistent with that reported in the literature [193–196]. The simulation based on OSI is presented for a shorter time, due to the stenosis developing around the limits of the buffer region. Despite the general similarity, there are a number of differences: both in the shape of the final stenosis; and also its development. For

example, compared to the others, Figures 10.1 (e) and 10.2 (e) show the stenosis development extending further into the artery on the ECA and extending less far along the ICA. Figures 10.1 (g) and 10.2 (g) show that when TAD_{II} is used as a marker the formation occurs fully on the ICA before switching to the ECA. This is in contrast to the other cases where the development in the ECA occurs predominantly towards the start of the process.

To further investigate the differences between simulations Figure 10.3 shows ΔT_s^* defined as $T_{sX}^* - T_{sY}^*$, where T_{sX}^* is the value of T_s^* when $X = \overline{u^{(1)}}$ is the haemodynamic marker. T_{sY}^* is the haemodynamic marker for $Y \in \{\overline{u_t^{(1)}}$, TAWSS, RFI, SI, RRT,TA$D_{II}$, O:WS$\}$. OSI was not considered here since the behaviour in Figures 10.1 (h) and 10.2 (h) is very different to the other cases. Figures 10.3 (a) and (b) indicate that the markers $\overline{u^{(1)}}$, $\overline{|u_t^{(1)}|}$ and TAWSS are all enabling the stenosis to form in a very similar manner. The other parameters (RFI, SI, RRT, TAD_{II} and O:WS) cause the stenosis to develop in significantly different manner, compared to $\overline{u^{(1)}}$. Figure 10.4 shows ΔT_s^* for these parameters where $X =$ O:WS and $Y \in \{$RFI, SI, RRT and TA$D_{II}\}$. Considerable similarity is seen in Figure 10.4 (c) and to a lesser extent in Figure 10.4(a). This indicates that as a marker for stenosis development O:WS and RRT act in a very similar manner, with RFI also producing a similar outcome. The results in Figures 10.1, 10.2, 10.3, 10.4 indicating that using low time-averaged near-wall velocity, time-averaged tangential near-wall velocity and TAWSS to determine how and where the stenosis develops all give a virtually identical outcome, and so can be used interchangeably as markers for stenosis formation. The results obtained using RRT and the ratio O:WS also showed considerable similarity to each other and so these two markers can also be applied interchangeably. These two sets of markers act in, along with RFI, SI and TAD_{II}, although predicting different progression for the stenosis, all predict similar final geometries. OSI, on the other hand, predicts a significantly different process which is in contrast

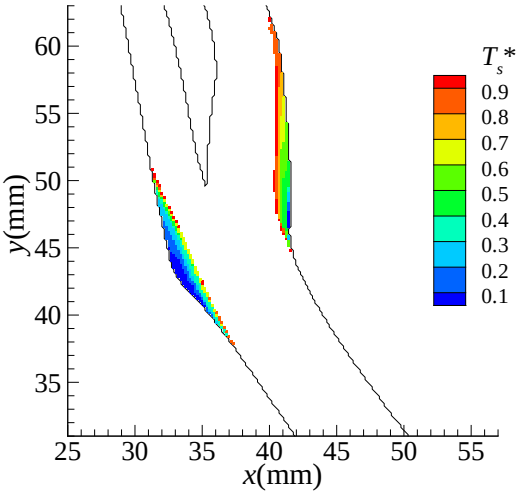

(a) $\overline{u^{(1)}}$

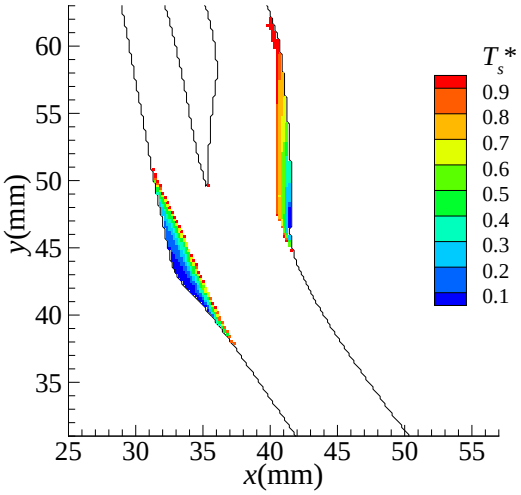

(b) $\overline{|u_t^{(1)}|}$

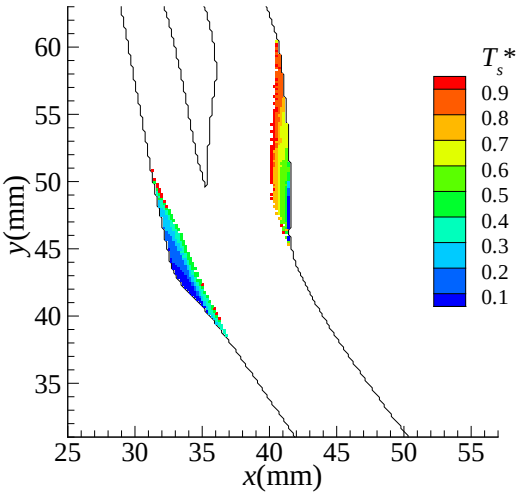

(c) TAWSS

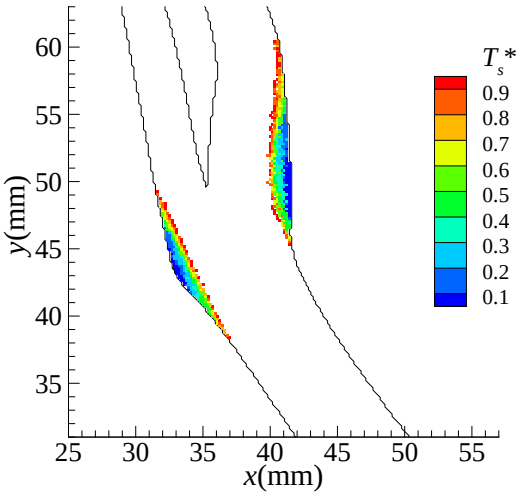

(d) RFI

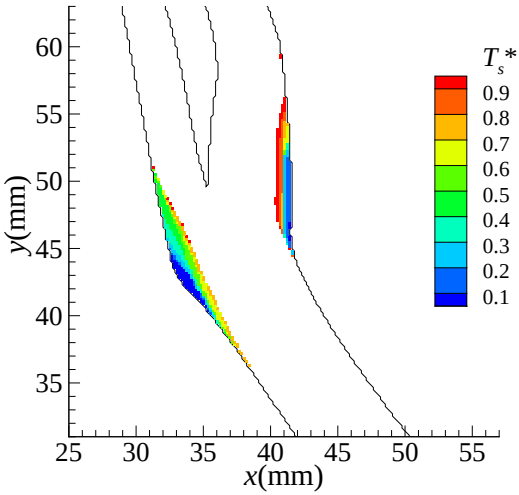

(e) SI

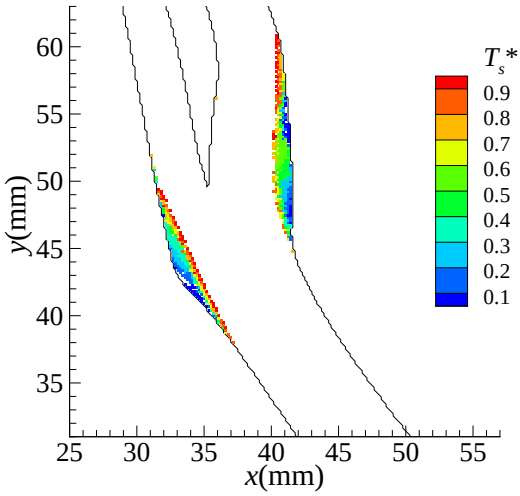

(f) RRT

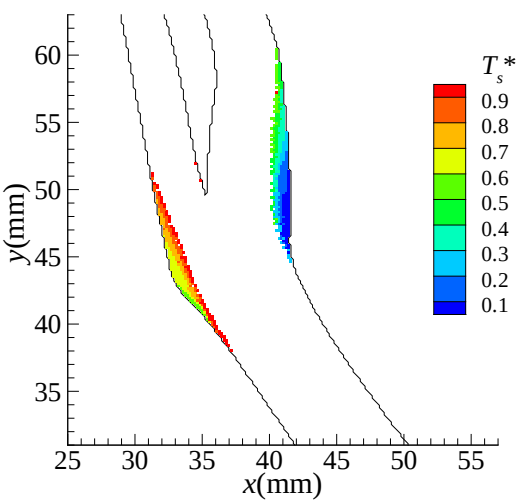

(g) TAD_{II}

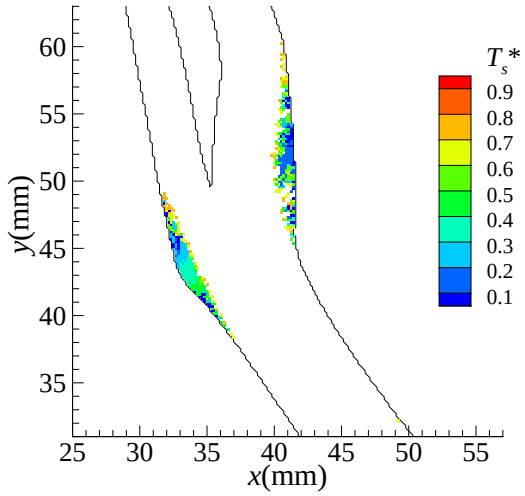

(h) OSI

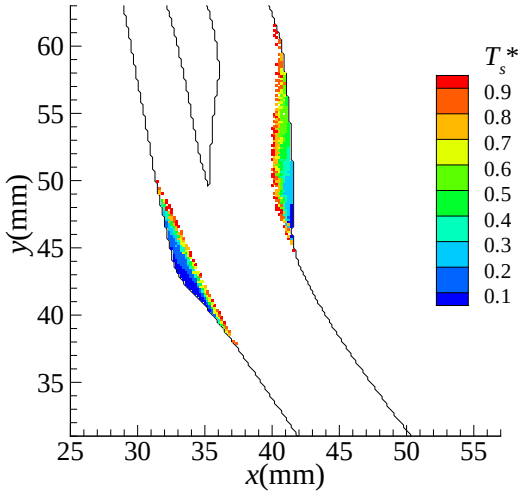

(i) O:WS

Figure 10.2: Stenosis development for markers (a) $\overline{u^{(1)}}$, (b) $\overline{|u_t^{(1)}|}$, (c) TAWSS, (d) RFI, (e) SI, (f) RRT, (g) TAD_{II}, (h) OSI and (i) O:WS

with observations in the literature [193–196]. This suggests that although the OSI can be considered important in determining where the stenosis will develop, it is not on its own a marker for stenosis development; and must be combined with other haemodynamic properties, such as TAWSS in a combined parameter such as O:WS. Since the OSI parameter does not predict a realistic stenosis, it will not be considered further in this chapter.

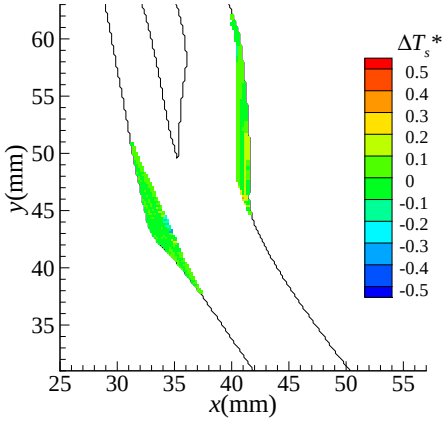

(a) $Y = \overline{|u_t^{(1)}|}$

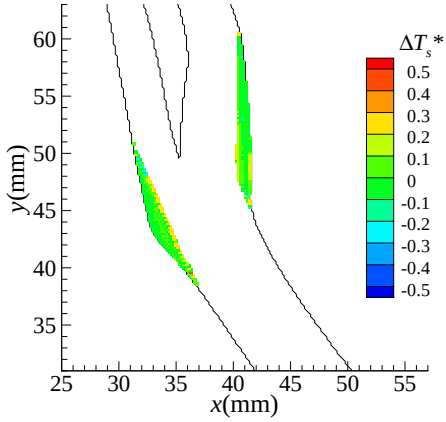

(b) $Y =$TAWSS

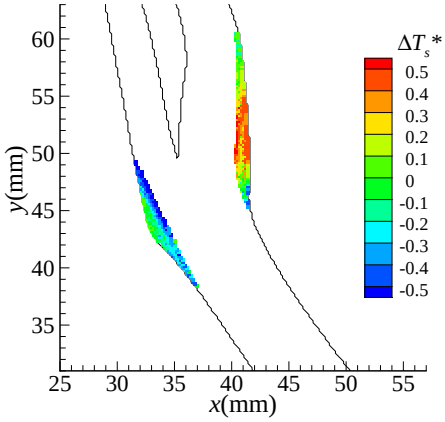

(c) $Y =$RFI

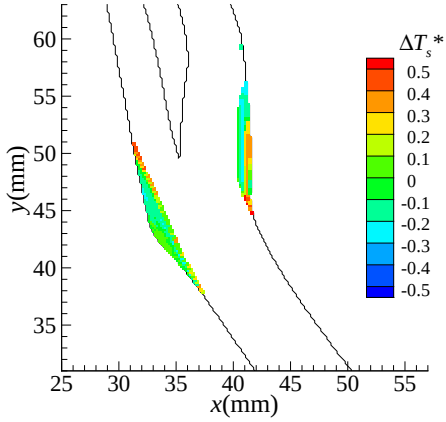

(d) $Y =$SI

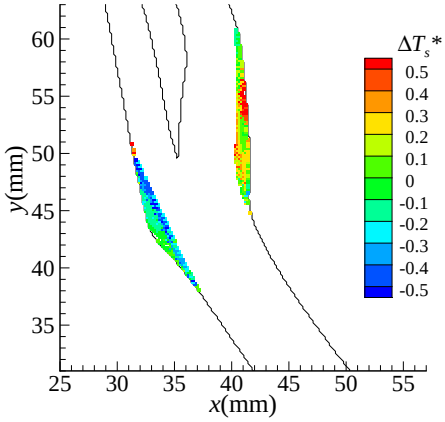

(e) $Y =$RRT

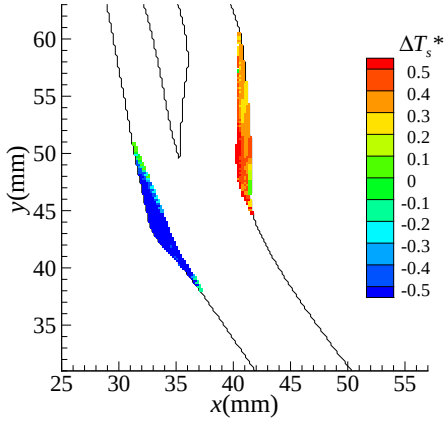

(f) $Y =$TAD_{II}

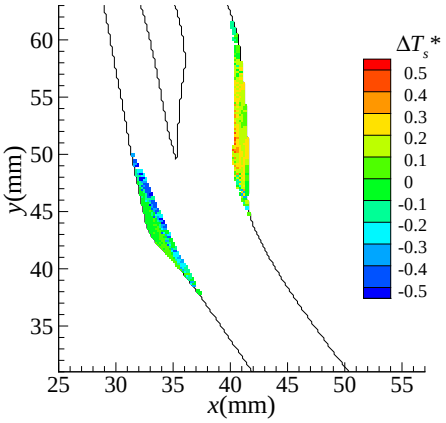

(g) Y =O:WS

Figure 10.3: ΔT_s^*, where $X = \overline{u^{(1)}}$ and (a) Y=$\overline{|u_t^{(1)}|}$, (b) Y = TAWSS, (c) Y = RFI, (d) Y = SI, (e) Y = RRT, (f) Y = TAD_{II} and (g) Y = O:WS.

10.2 Geometrical development

To further assess the effect of the different markers, Figure 10.5 shows the area converted from wall to dry on the ECA and ICA as a function of T_s^*. On both walls the curves for $\overline{u^{(1)}}$, $\overline{|u_t^{(1)}|}$, TAWSS are consistent with the first two being almost indistinguishable. The two curves for RRT and O:WS are also very consistent with each other. The curve for RFI is similar to the RRT/O:WS curves, while TAD_{II} and SI curves are somewhat different than the others.

Another useful way to characterise the stenosis development is through the diameter of the artery for a number of sections shown in Figure 10.6. In Figure 10.6 the black line shows the geometry of the healthy artery at $T_s^* = 0$ and the red curve the stenosed artery at $T_s^* = 1$, when $\overline{u^{(1)}}$ is used as a marker for the stenosis development.

The change in diameter along the sections is shown in Figure 10.7, for the different markers. The curves further highlight the strong similarity of $\overline{u^{(1)}}$, $\overline{|u_t^{(1)}|}$ and TAWSS. RRT and O:WS are again shown to be similar; RFI is somewhat

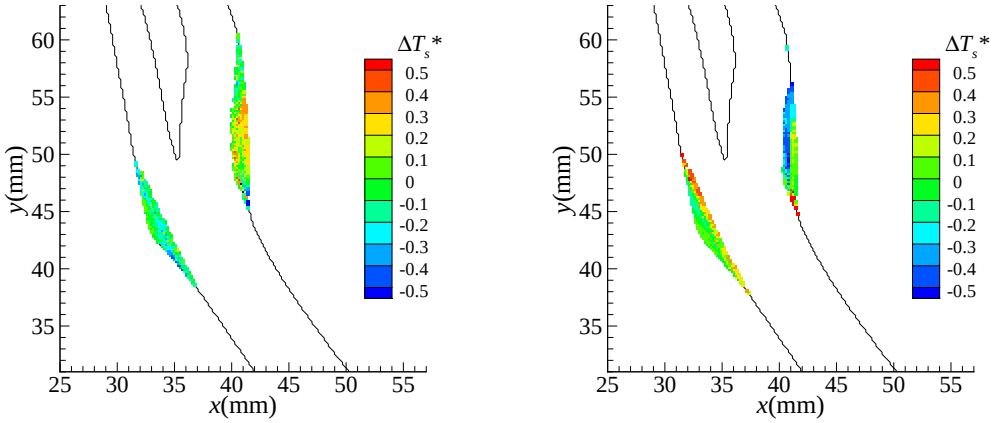

(a) Y =RFI (b) Y =SI

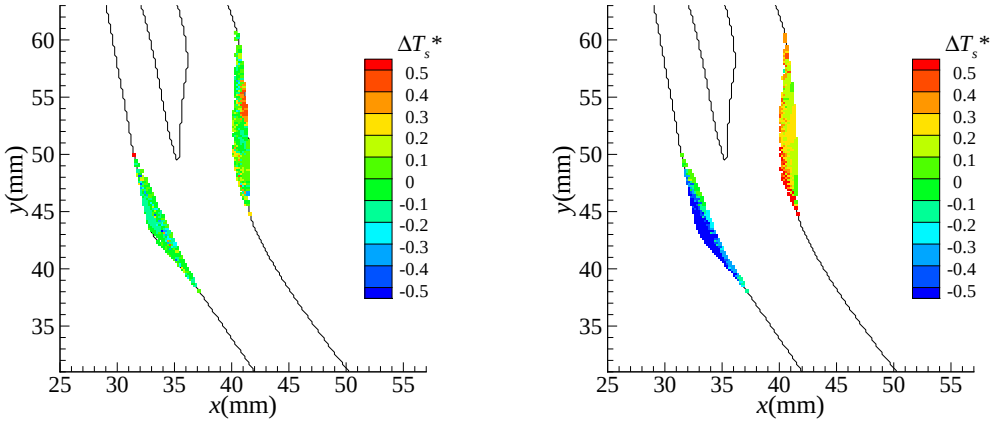

(c) Y =RRT (d) Y =TAD_{II}

Figure 10.4: ΔT_s^*, where X = O:WS, (a) Y = RFI, (b) Y = SI, (c) Y = RRT and (d) = Y = TAD_{II}

similar to RRT and O:WS in some regions, while in others difference can be observed. TAD_{II} and SI show a different development.

The effect of the different marker on the haemodynamics is investigated in Figures 10.8 - 10.10 for the ECA and Figures 10.11 - 10.13, for the ICA. The haemodynamic properties shown are $\overline{u^{(1)}}$ in Figures 10.8 and 10.11; RFI in Figures 10.9 and 10.12; and OSI in Figures 10.10 and 10.13. In each of these figures, results are presented for different markers: (a) $\overline{u^{(1)}}$, (b) O:WS, (c) RFI, (d) SI and (e) TAD_{II}. For Figures 10.8-10.13, the results obtained when $\overline{|u_t^{(1)}|}$ and

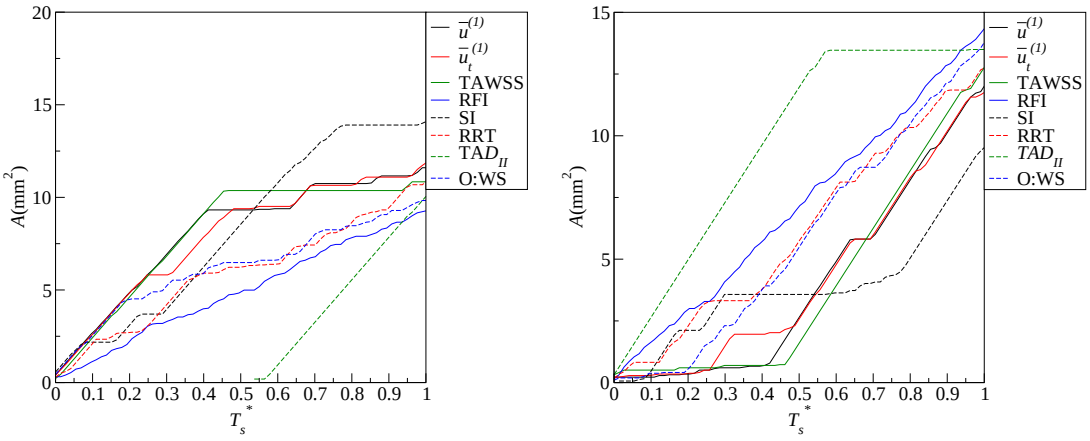

(a) ECA (b) ICA

Figure 10.5: Area removed from (a) the ECA and (b) the ICA by the developing stenosis for different markers

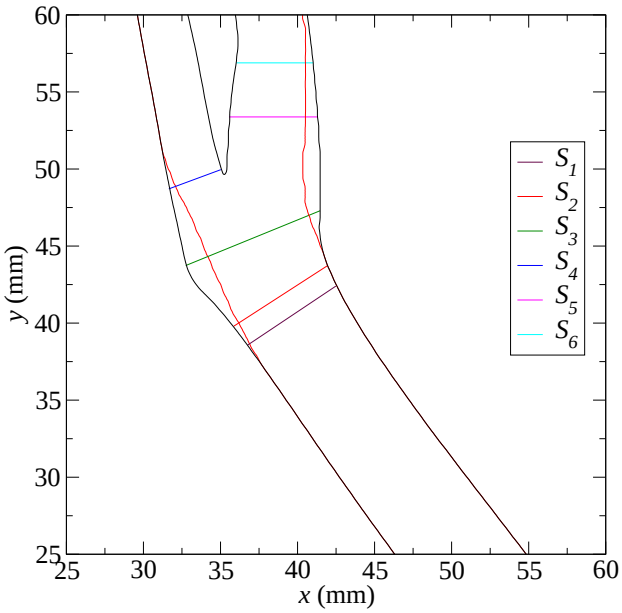

Figure 10.6: Artery sections

TAWSS were used as markers showed the same features when $\overline{u^{(1)}}$ was used (part (a)). Also, using RRT as a marker gave similar results to (O:WS) (part (b)). For this reason, results are not reported for $\overline{|u_t^{(1)}|}$, TAWSS or RRT. Comparing Figures 10.8 (a) and 10.8 (b), the same behaviour is observed up to $T_s^* \simeq 0.3$; after this the behaviour differs: in particular the low near-wall velocity region is maintained in Figure 10.8 (b) for much longer and is still fairly prominent at

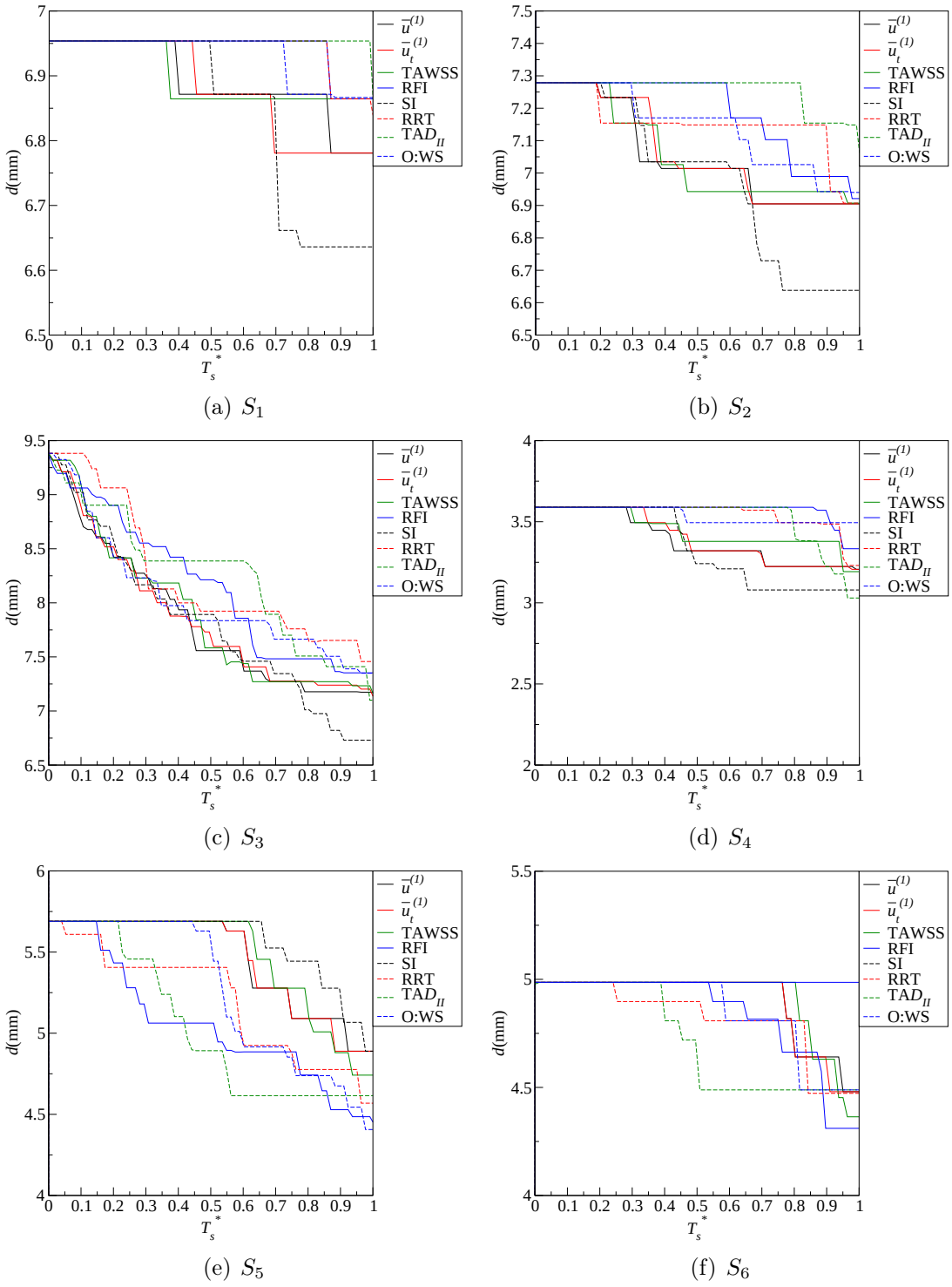

(a) S_1 (b) S_2

(c) S_3 (d) S_4

(e) S_5 (f) S_6

Figure 10.7: Change in artery diameter as the stenosis develops along the sections a) S_1, (b) S_2, (c) S_3, (d)S_4, (e) S_5 and (f) S_6, for alternative markers.

$T_s^* = 1$.

This is also evident when comparing Figures 10.9 (a) and (b) and Figures 10.10 (a) and (b) where the regions of significant RFI are similar for $T_s^* < 0.3$; however for $T_s^* > 0.3$ there are significant differences with considerably more reverse flow when O:WS is used as a marker - that is despite the marker acting to remove areas of low OSI (through enabling the stenosis to develop in such areas), albeit in conjunction with the TAWSS through O:WS. In each case differences are also observed when RFI, SI, and TAD_{II} are used as markers. Figure 10.8 (c) shows similar behaviour to Figure 10.8 (b) in that the low velocity region is maintained longer than in Figure 10.8 (a), but the averaged velocity alters more uniformly. Figure 10.8 (d) shows slightly different behaviour with the low averaged velocity region ending move abruptly at each y-position. Figure 10.8 (e) also shows a different behaviour, with the initial profile extending to around $T_s^* = 0.6$ before the low velocity region expands downstream. This is due to the stenosis only forming initially on the ICA, as seen in Figures 10.1 (g), 10.2 (g) and 10.5. Interestingly in Figure 10.1 (g), the stenosis expands further downstream ($y > 50$mm) when TAD_{II} is used as a marker, compared to Figure 10.1 (a) when $\overline{u^{(1)}}$ is used. This can be observed in Figure 10.8 (e) where the low average velocity region also reaches beyond $y = 50$mm, for $T_s^* > 0.9$. Here the low averaged velocity region appears to pierce through the higher velocity region in a similar way to that observed for the ICA in Figure 9.10 (b). The observations for the RFI, SI and TAD_{II} markers are consistent with Figures 10.9 and 10.10, which show regions of reversible and oscillatory flow associated with the low average-velocity region.

The behaviour of the haemodynamic wall properties on ICA in Figures 10.11 - 10.13 also demonstrate these same features. That is the $\overline{u^{(1)}}$, $\overline{|u_t^{(1)}|}$ and TAWSS marker plots are similar to each other, as are the RRT and O:WS marker plot - so again only marker $\overline{u^{(1)}}$ and O:WSS are presented for this group. When SI is

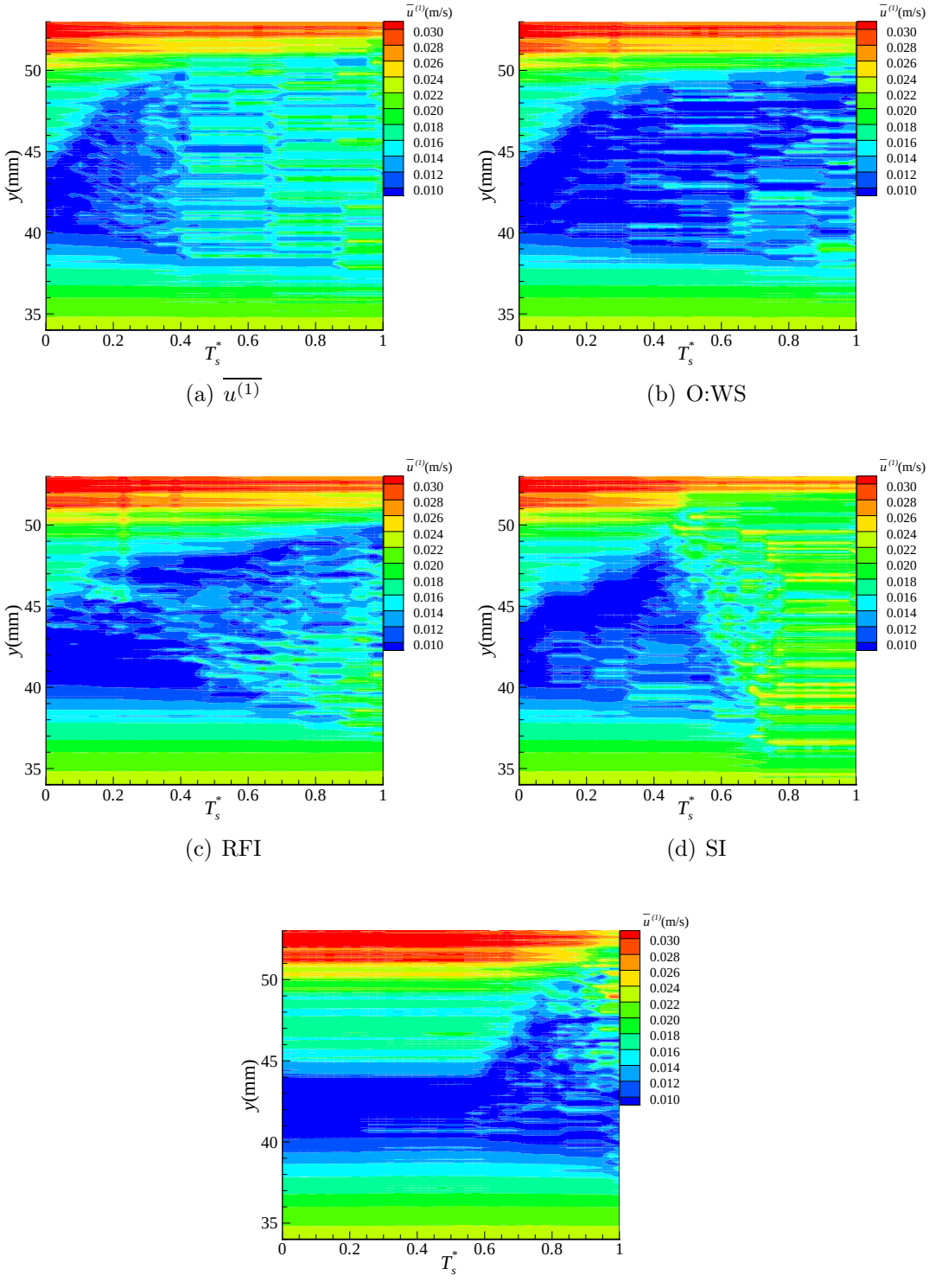

(a) $\overline{u^{(1)}}$ (b) O:WS

(c) RFI (d) SI

(e) TAD_{II}

Figure 10.8: $\overline{u^{(1)}}$ on outer wall of ECA, over the development of the stenosis when the applied marker is (a) $\overline{u^{(1)}}$, (b) O:WS, (c) RFI, (d) SI and (e) TAD_{II}.

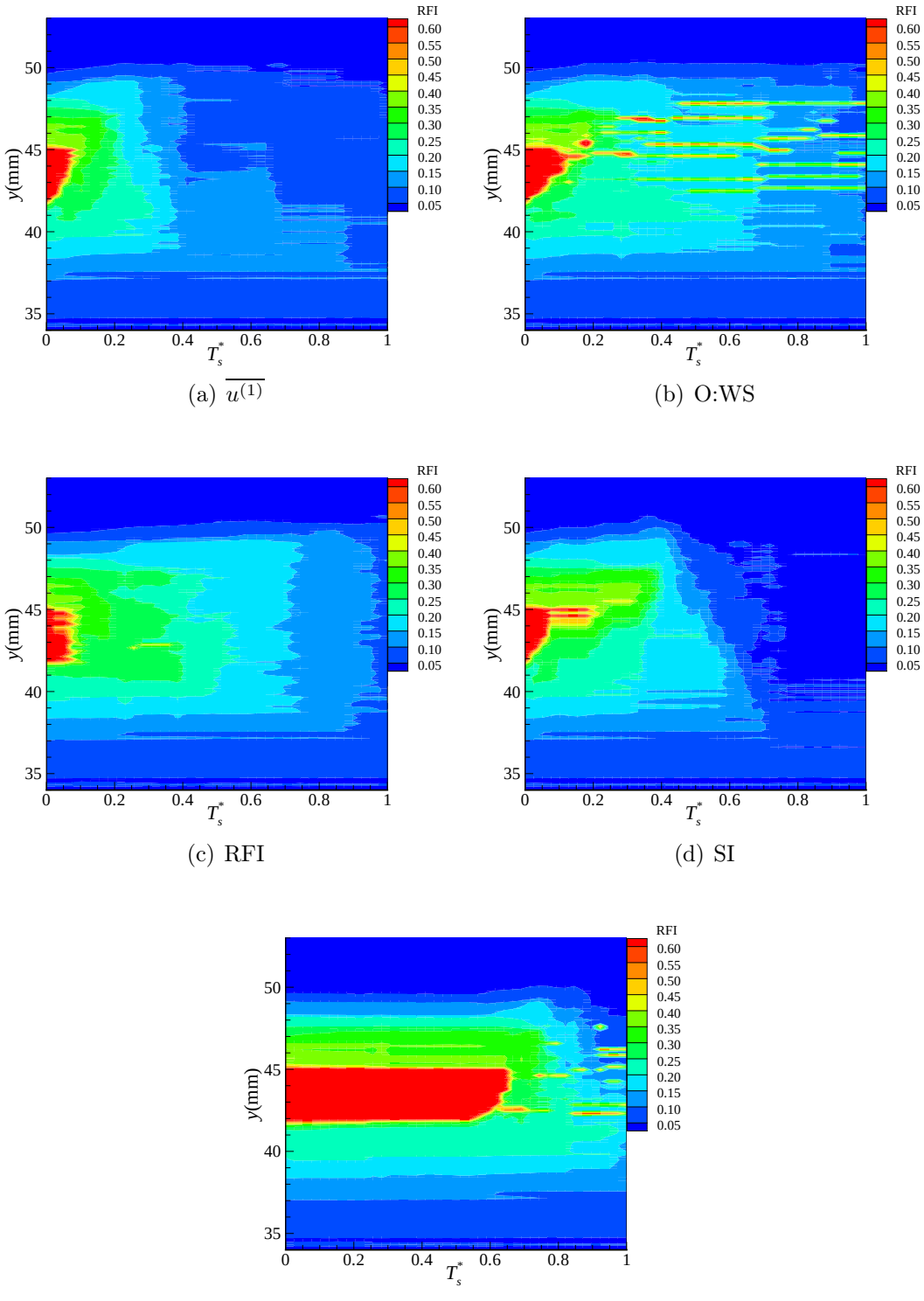

(a) $\overline{u^{(1)}}$ (b) O:WS

(c) RFI (d) SI

(e) TAD_{II}

Figure 10.9: RFI on outer wall of ECA, over the development of the stenosis when the applied marker is $\overline{u^{(1)}}$, (b) O:WS, (c) RFI, (d) SI and (e) TAD_{II}.

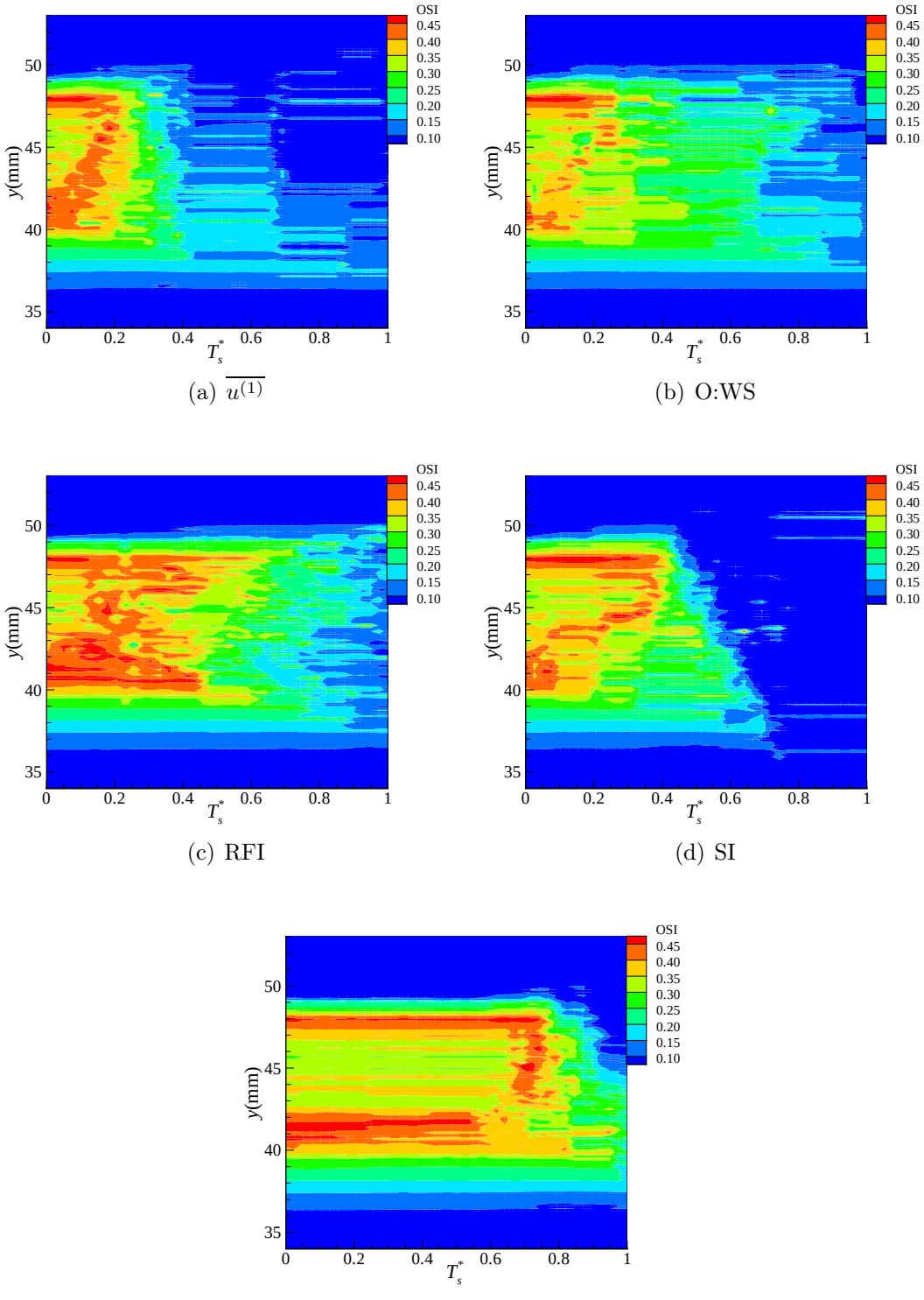

(a) $\overline{u^{(1)}}$ (b) O:WS

(c) RFI (d) SI

(e) TAD_{II}

Figure 10.10: OSI on outer wall of ECA over the development of the stenosis when the applied marker is (a) $\overline{u^{(1)}}$, (b) O:WS, (c) RFI, (d) SI and (e) TAD_{II}.

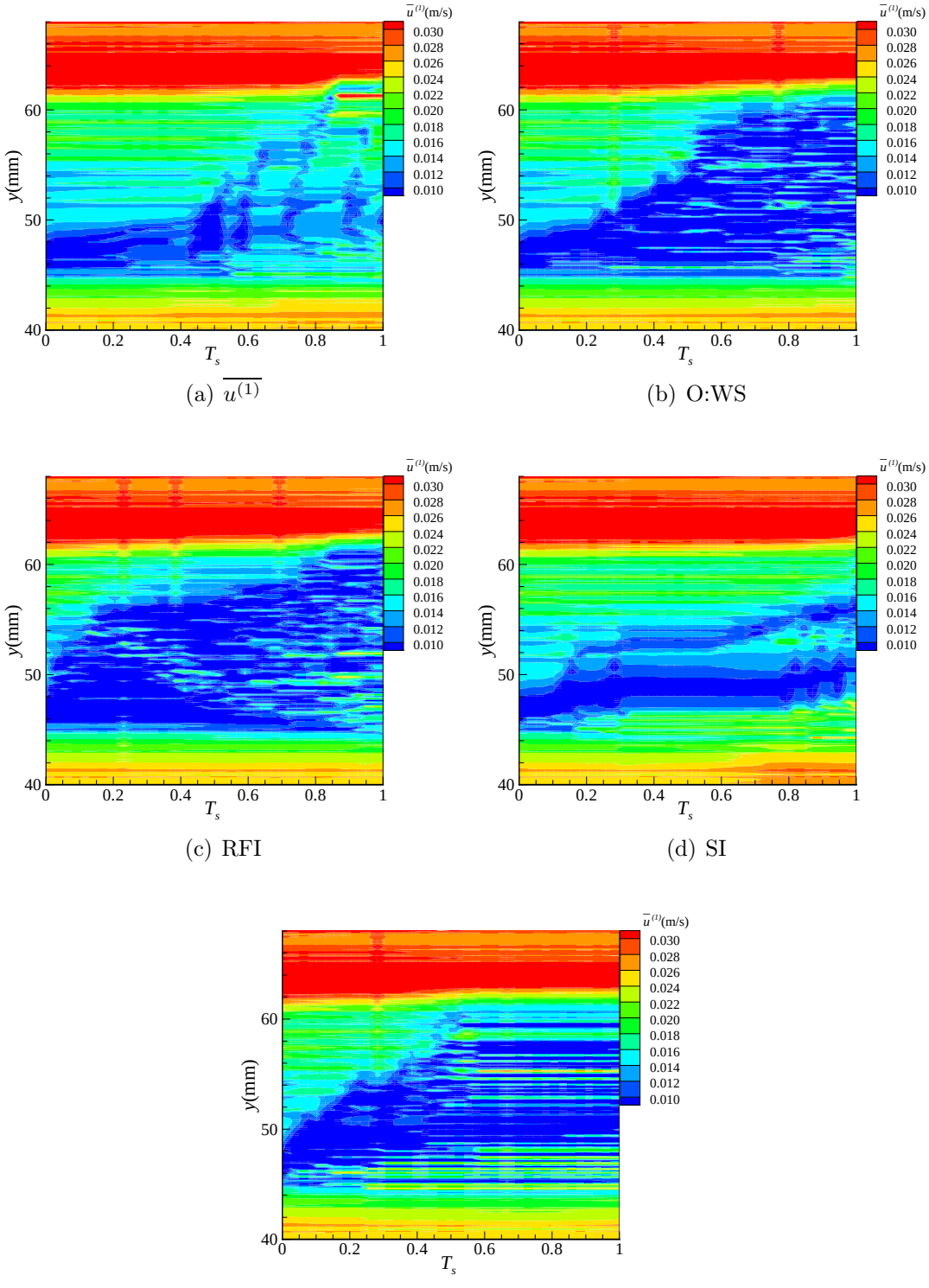

(a) $\overline{u^{(1)}}$

(b) O:WS

(c) RFI

(d) SI

(e) TAD_{II}

Figure 10.11: $\overline{u^{(1)}}$ on outer wall of ICA, over the development of the stenosis when the applied marker is (a) $\overline{u^{(1)}}$, (b) O:WS, (c) RFI, (d) SI and (e) TAD_{II}.

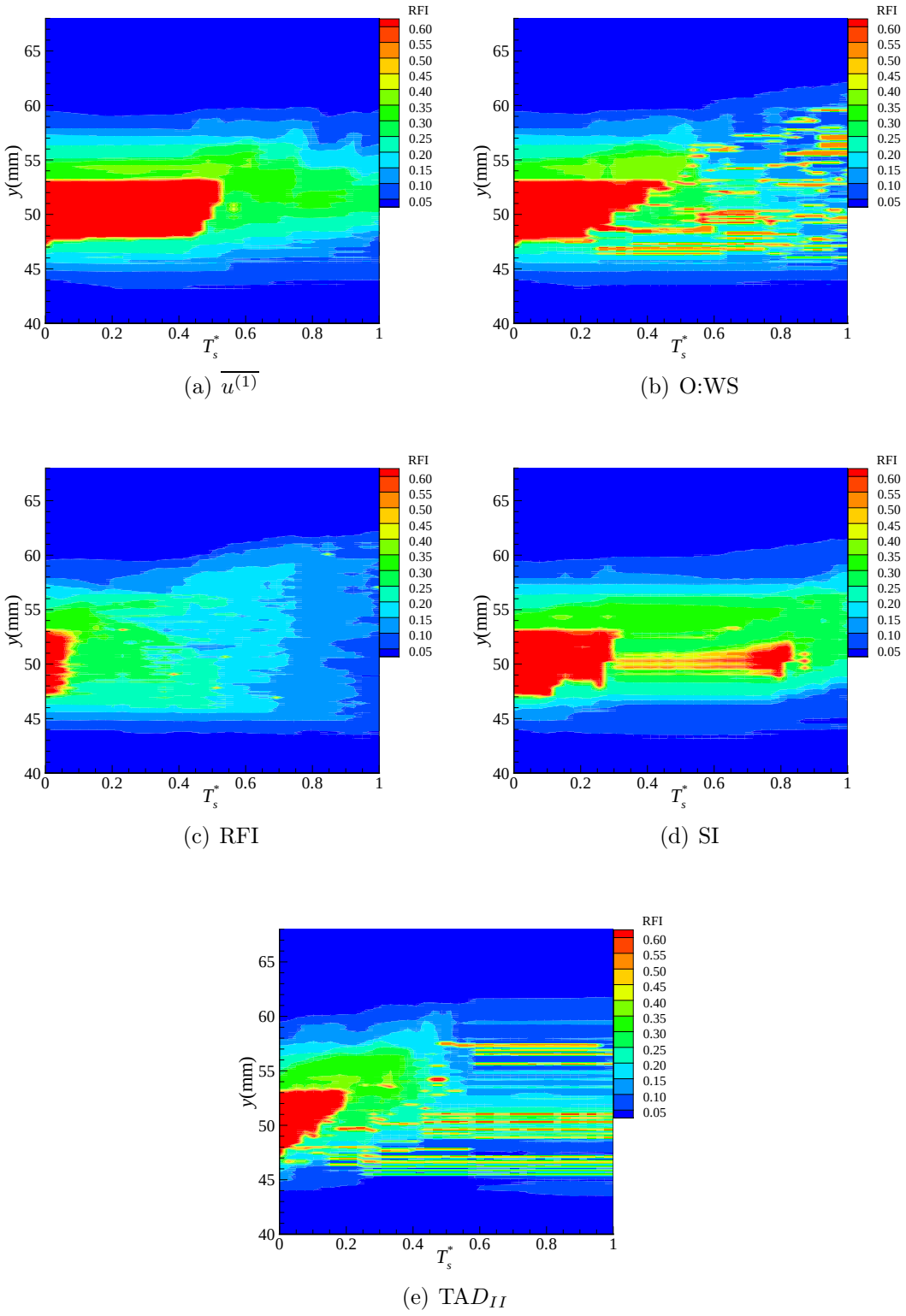

(a) $\overline{u^{(1)}}$ (b) O:WS

(c) RFI (d) SI

(e) TAD_{II}

Figure 10.12: RFI on outer wall of ICA, over the development of the stenosis when the applied marker is $\overline{u^{(1)}}$, (b) O:WS, (c) RFI, (d) SI and (e) TAD_{II}.

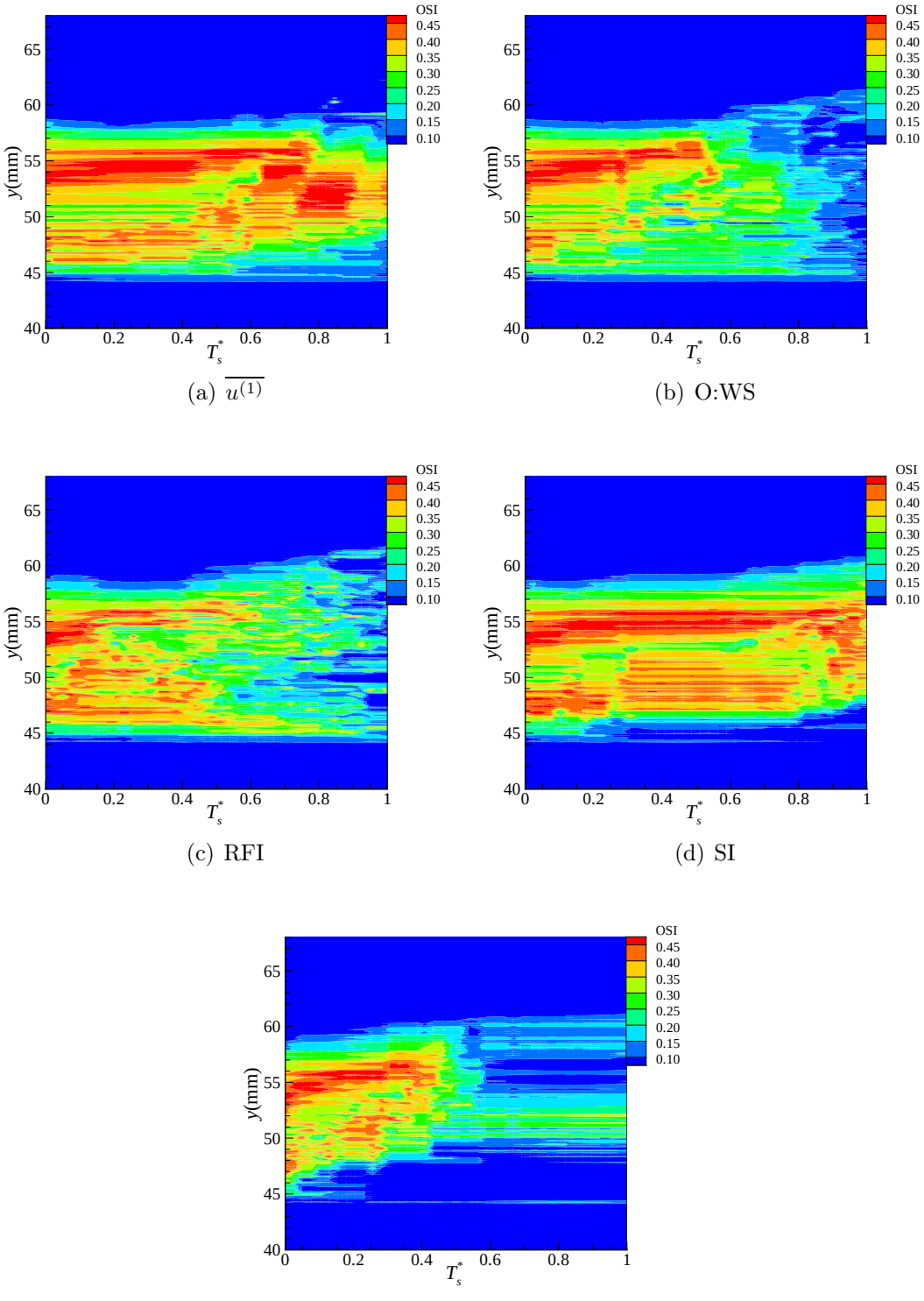

(a) $\overline{u^{(1)}}$ (b) O:WS

(c) RFI (d) SI

(e) TAD_{II}

Figure 10.13: OSI on outer wall of ICA over the development of the stenosis when the applied marker is (a) $\overline{u^{(1)}}$, (b) O:WS, (c) RFI, (d) SI and (e) TAD_{II}.

a marker, Figures 10.11 and 10.12 part (d), the behaviour is different: the low averaged velocity/inverse/ oscillatory flow is maintained throughout the development in a fairly uniform manner. In Figures 10.11 and 10.12 part (e) where TAD_{II} is the marker, the low time averaged velocity initially expands rapidly downstream (as the stenosis develops on the ICA - see from Figures 10.2 (g) and 10.5 (b)) and then the profile remains fixed for $T_s^* > 0.5$. By this time, the TA tangential velocity is positive (Figure 10.12 (e)), all the oscillatory and reversible flow is significantly reduced, Figures 10.13 and 10.12 part (e).

10.3 Conclusion

In terms of a marker for the stenosis development, the near-wall time averaged velocity $\overline{u^{(1)}}$, its tangential magnitude $\overline{|u_t^{(1)}|}$ and the TAWSS all produce very similar stenosis development and the resulting haemodynamic wall parameters are affected in a very similar manner. Markers RRT and O:WS also produced similar stenosis development and the associated haemodynamic parameters are similar to each other.

RFI, SI and TAD_{II} markers produce noticeable differences between each other and between the two sets of parameters described above ($\overline{u^{(1)}}$, $\overline{|u_t^{(1)}|}$, TAWSS, and RRT, O:WS). In each case the stenosis develops in a slightly different way and the near wall haemodynamic behaviour is also different. Despite the differences in formation, the form of the stenosis on both the ECA and ICA is similar for each of the markers and consistent with observations in the literature [193–196]. This suggests that each of these haemodynamic properties are good markers for stenosis development.

In contrast, when OSI is used as a marker, the stenosis is formed in a significantly different manner which is not consistent with literature observations. It can thereafter be concluded that OSI on its own is not a good marker for steno-

sis development. Low near wall velocity, as measured through $\overline{u^{(1)}}$ produced a realistic stenosis formation as did O:WS. Although differences were observed between the stenosis development when $\overline{u^{(1)}}$ and O:WS were used as markers, both produced results consistent with literature and so it is not possible to determine which marker is superior; however, the similarity suggests that considering OSI in conjunction with the TAWSS at least in terms of the O:WS parameter considered here, does not produce a significant advantage over using low TAWSS on its own, or indeed low near wall velocity.

Details of imaged stenosed geometries in the literature are varied, due to the natural differences between individuals. Additionally, images in the literature focus on particular stages of development, rather than following the progression of the disease. Thus it is not possible to differentiate between the differences observed here between the markers, although it is clear that the choice of marker can have a noticeable affect on the near-wall haemodynamics.

Chapter 11

Effect of non-Newtonian properties on stenosis development

11.1 Introduction

A number of studies have considered the non-Newtonian nature of the blood flow [43, 106, 107, 140–143, 145, 200–203]. Some have concluded that it makes little difference to the simulation results [107, 140, 141, 143, 200–202, 204]; while others suggest that the effect is important [43, 142, 203]. Here we consider how simulating the non-Newtonian nature of blood influences the stenosis development model described in Chapter 6. Two cases were considered; one using a Newtonian model and the second using the C-Y model described in Section 3.4.

11.2 Stenosis development

Results of the simulations are presented in Figures 11.1 and 11.2 when TAWSS and O:WS are used as markers respectively. In Chapter 10 it was noted that time averaged near-wall velocity, $\overline{u^{(1)}}$ and TAWSS were similar markers for stenosis development. This was also seen in Chapter 6 through the definition of $\overline{u^{(1)}}$.

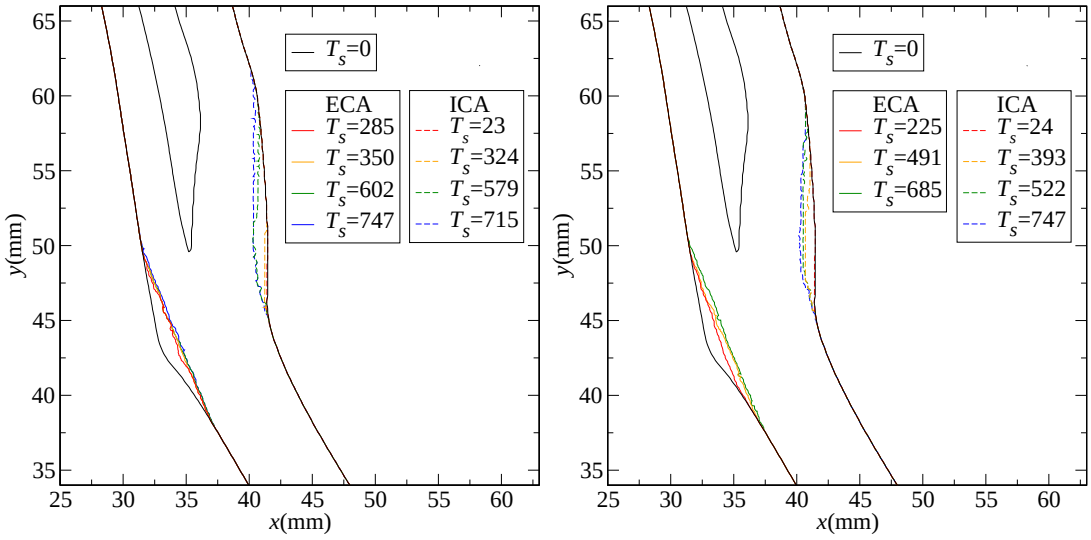

(a) Newtonian (b) C-Y

Figure 11.1: Layer development of the stenosis using TAWSS as a marker for (a) the Newtonian model and (b) the non-Newtonian C-Y model.

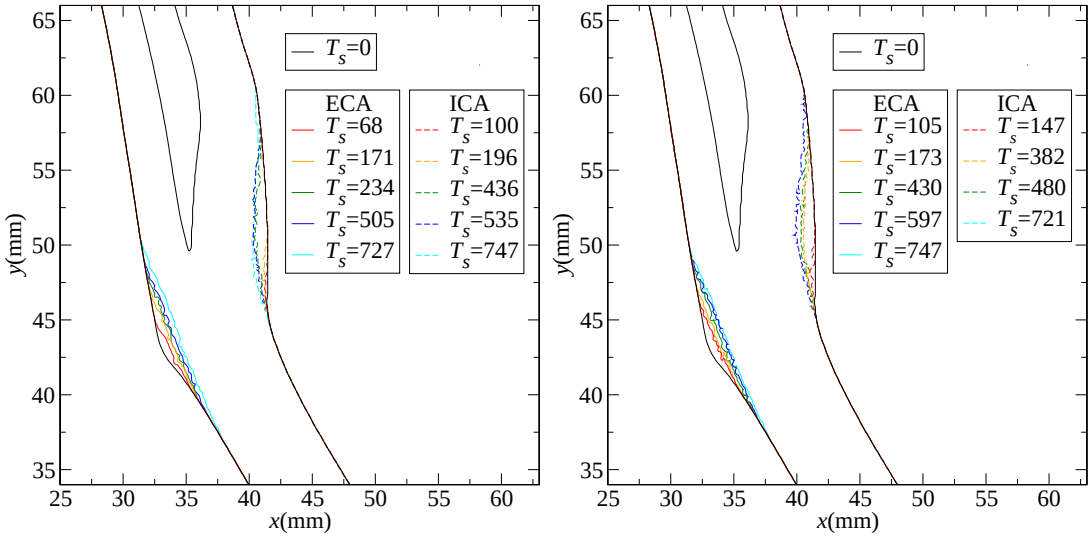

(a) Newtonian (b) C-Y

Figure 11.2: Layer development of the stenosis using O:WS as a marker for (a) the Newtonian model and (b) the non-Newtonian C-Y model.

In the non-Newtonian case this relationship no longer holds since the velocity gradient is no longer proportional to the TAWSS. Here TAWSS was preferred over the TA velocity since this incorporates the non-Newtonian nature of the blood in terms of the changed haemodynamics and also the variable viscosity

at the wall. In Figures 11.1 and 11.2 the overall formation of the stenosis is similar for both the Newtonian and the non-Newtonian models; however some differences can be observed. On the ECA, in Figure 11.1 the second, third and fourth layers do not significantly increase the stenosed region for the Newtonian case; while for the non-Newtonian case there is a significant difference between the first and last layers. Differences are also evident on the ICA where the second layer develops more significantly in the non-Newtonian model. However, these differences do not significantly affect the final stenosed geometry and are no

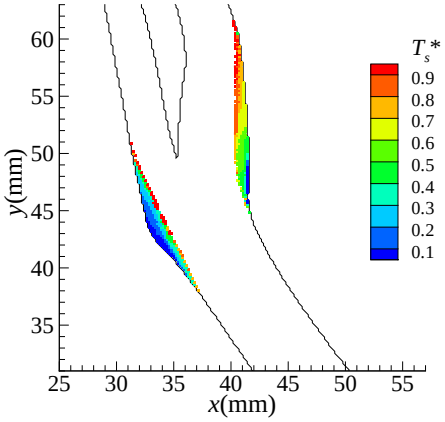

(a) Newtonian

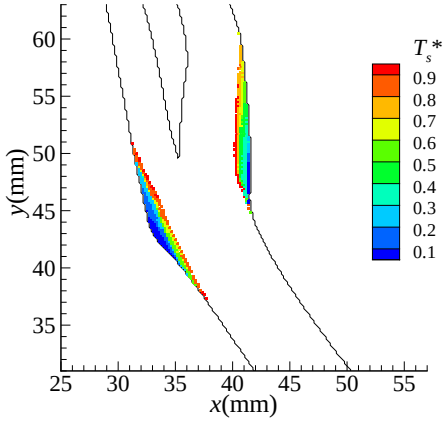

(b) C-Y

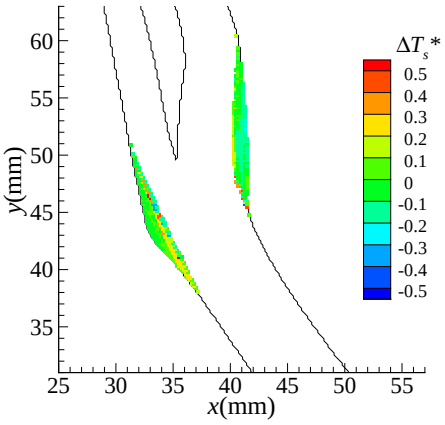

(c) Comparison

Figure 11.3: Stenosis development using TAWSS as a marker for (a) Newtonian model and (b) Non-Newtonian C-Y model and (c) their comparison.

greater than the differences between the two different markers (TAWSS in Figure 11.1 and O:WS in Figure 11.2). These differences are also evident in Figure 11.3, 11.4 which show, for markers TAWSS and O:WS respectively, the development of the stenosis for both the Newtonian and non-Newtonian models, and also a comparison between the two. Particularly in Figures 11.3(c) and 11.4(c) which show the differences $\Delta T_s^* = T_{sN}^* - T_{sCY}^*$ for the Newtonian and non-Newtonian model. The differences observed in Figures 11.3(c) and 11.4(c) are generally small; however are significantly larger than the differences observed in Figure 10.3(a)

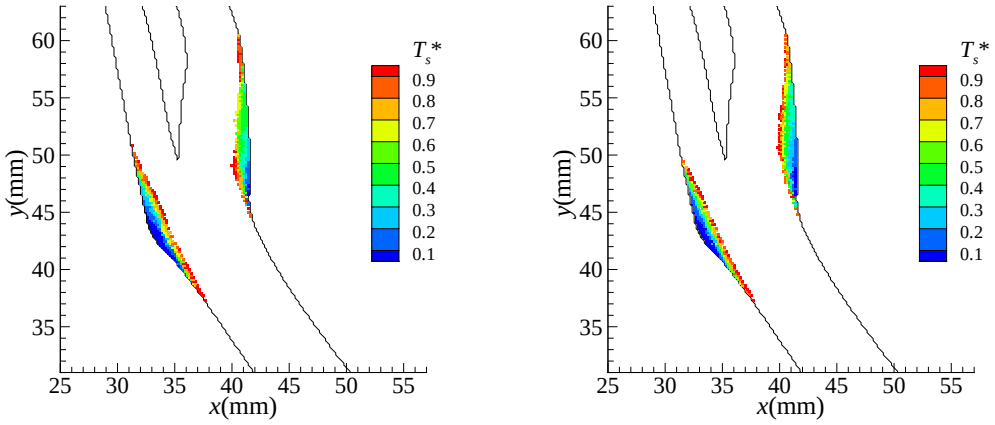

(a) Newtonian

(b) C-Y

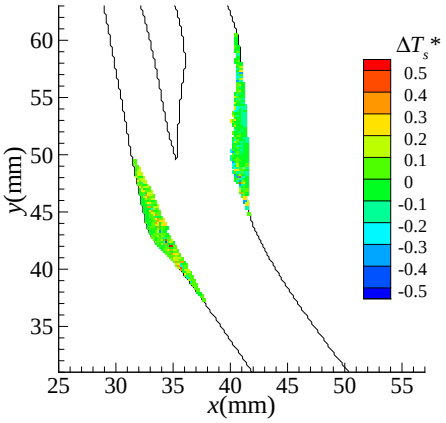

(c) Comparison

Figure 11.4: Stenosis development using O:WS as a marker for (a) Newtonian model and (b) Non-Newtonian C-Y model and (c) their comparison.

and (b). A red/orange line is present through the ECA side corresponding to the differences in the layers discussed for Figure 11.1 (a). There is also a light blue region near the wall for the ICA region in Figure 11.4 - this corresponds to the differences in layer 2 observed in Figure 11.1 (b). Figure 11.5 shows how the area

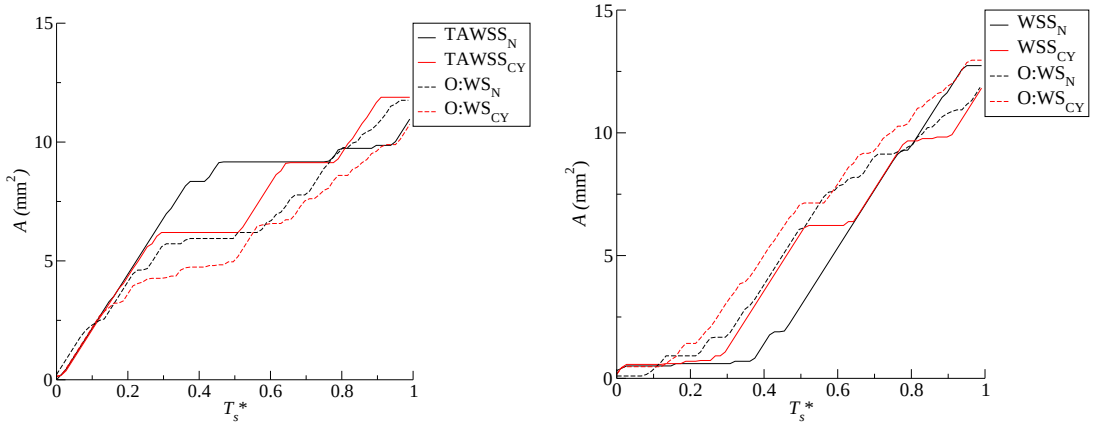

(a) A on ECA (b) A on ICA

Figure 11.5: Area removed from (a)the ECA and (b) the ICA by the developing stenosis using TAWSS and O:WS as markers for both the Newtonian and Non-Newtonian C-Y models.

in the ECA and ICA, corresponding to sites converted from fluid to wall, grows with T_s^*. Although the final level of stenosis development is seen to be similar in Figures 11.5 (a) and (b), there are noticeable differences for $0.2 \leq T_s^* < 0.6$ and $0.8 \leq T_s^* \leq 1$. The first of these is due to the differences observed in Figures 11.1, and 11.3 and 11.4 and the second, while smaller, again represents a difference in the development. Figure 11.6 shows differences in the rate at which the artery is being occluded on the artery sections shown in Figure 10.6. These differences are fairly small; but they do show the development being altered due to the non-Newtonian nature of the blood.

These observed changes in the artery geometry can potentially alter the haemodynamics in the artery. To investigate this the wall parameters, $\overline{u^{(1)}}$, $\overline{u_t^{(1)}}$, OSI, RRT and RFI, are shown in Figure 11.7 for the ECA and in Figure 11.8 for the ICA. Figures 11.7 (a) and (b), for the ECA, show initial changes in the

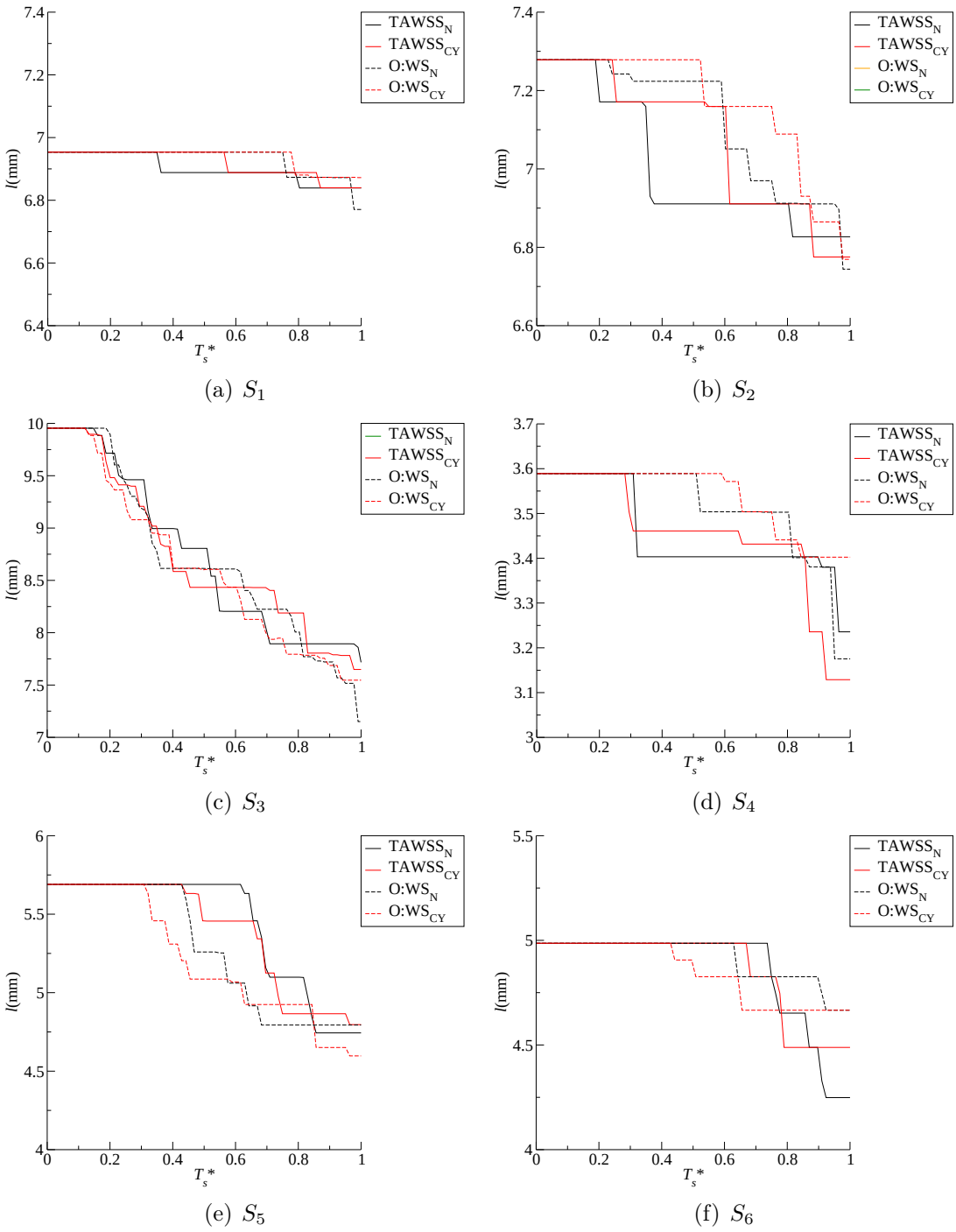

(a) S_1 (b) S_2

(c) S_3 (d) S_4

(e) S_5 (f) S_6

Figure 11.6: Change in artery diameter as the stenosis develops along the sections a) S_1, (b) S_2, (c) S_3, (d)S_4, (e) S_5 and (f) S_6 using TAWSS and O:WS as a marker for both the Newtonian and Non-Newtonian models.

near-wall velocity, with the low velocity region expanding in the downstream direction. Differences are observed for $T_s^* > 0.3$, where the non-Newtonian shows a region of lower velocity, particularly, in range A: 39mm $< y <$ 45mm. This region is also evident in Figures 11.7 (c) and (d) where an additional difference is also observed in that the initial region where $\overline{u_t^{(1)}}$ is negative- representing significant reversed flow during the period- which is initially present in range B 42mm $< y <$ 47mm, is maintained for a shorter time in the non-Newtonian case. The OSI and RRT are presented in Figures 11.7 (e) and (f) and 11.7 (g) and (h) respectively. A comparison of both show an increased value of both in range A for $0.25 < T_s^* < 0.5$ in the case of the non-Newtonian simulations. In range B the values of OSI and RRT are initially higher for the non-Newtonian simulations, but they reduce slightly sooner and less sharply at $T_s^* \simeq 0.2$. The RFI, shown in Figures 11.7 (i) and (j) displays the most significant differences between the Newtonian and non-Newtonian simulations in region B, for $T_s^* < 0.2$, RFI is significantly lower. In region A, the RFI is maintained at a slightly higher value in the non-Newtonian simulations for $0.43 < T_s^* < 0.6$.

This gives an effect of using a non-Newtonian model where the reverse flow in the region downstream of the stenosis development is significantly reduced in terms of the time averaged near-wall tangential velocity, $\overline{u_t^{(1)}}$, in Figure 11.7 (d); the percentage of the period where the flow is reversed, RFI in Figure 11.7 (i); as well as a small reduction in the time over which high values of OSI, Figure 11.7 (f), and RRT, Figure 11.7 (h) are maintained. Despite this picture of the overall reduction in reversal/oscillatory flow, Figures 11.7 (f) and (h) also show a slight increase in the magnitude of OSI and RRT in region A. Additionally around the upstream development of the stenosis, there is a difference in the near-wall velocity relative to the Newtonian case. Figure 11.8 shows the same haemodynamic properties in the ICA. Again, there is considerable similarity in the results from the Newtonian and non-Newtonian simulations. There are also

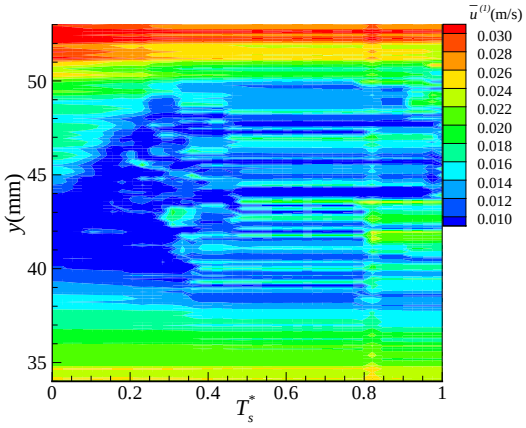

(a) $\overline{u^{(1)}}$ for Newtonian model

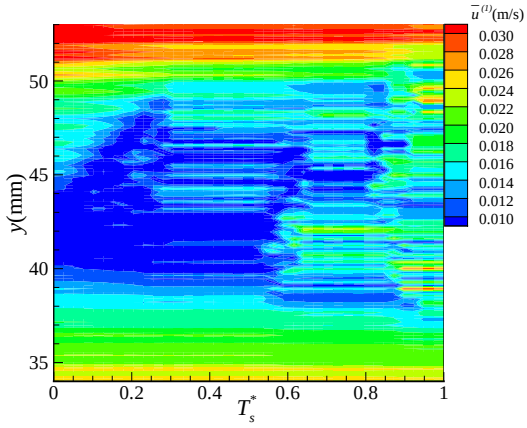

(b) $\overline{u^{(1)}}$ for C-Y model

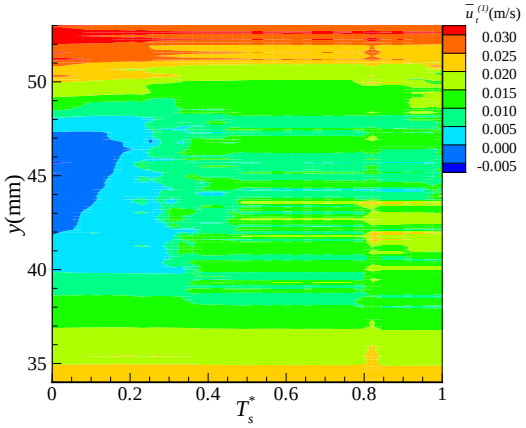

(c) $\overline{u_t^{(1)}}$ for Newtonian model

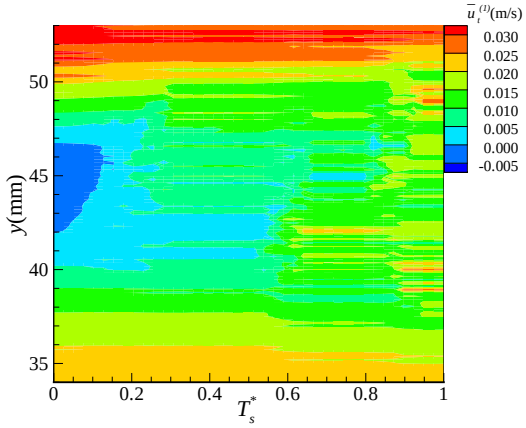

(d) $\overline{u_t^{(1)}}$ for C-Y model

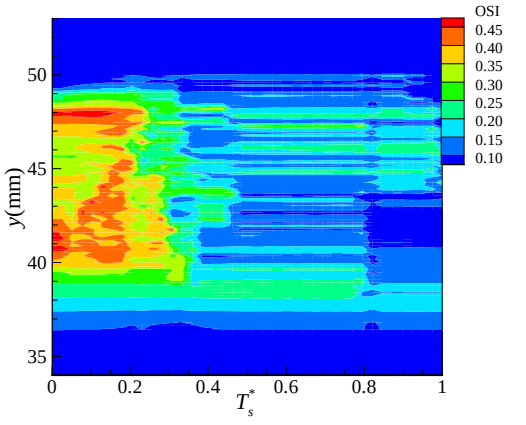

(e) OSI for Newtonian model

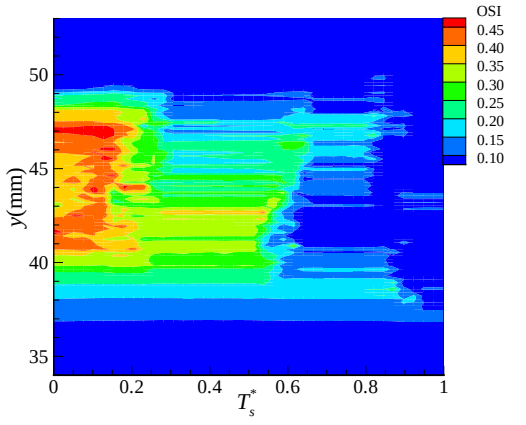

(f) OSI for C-Y model

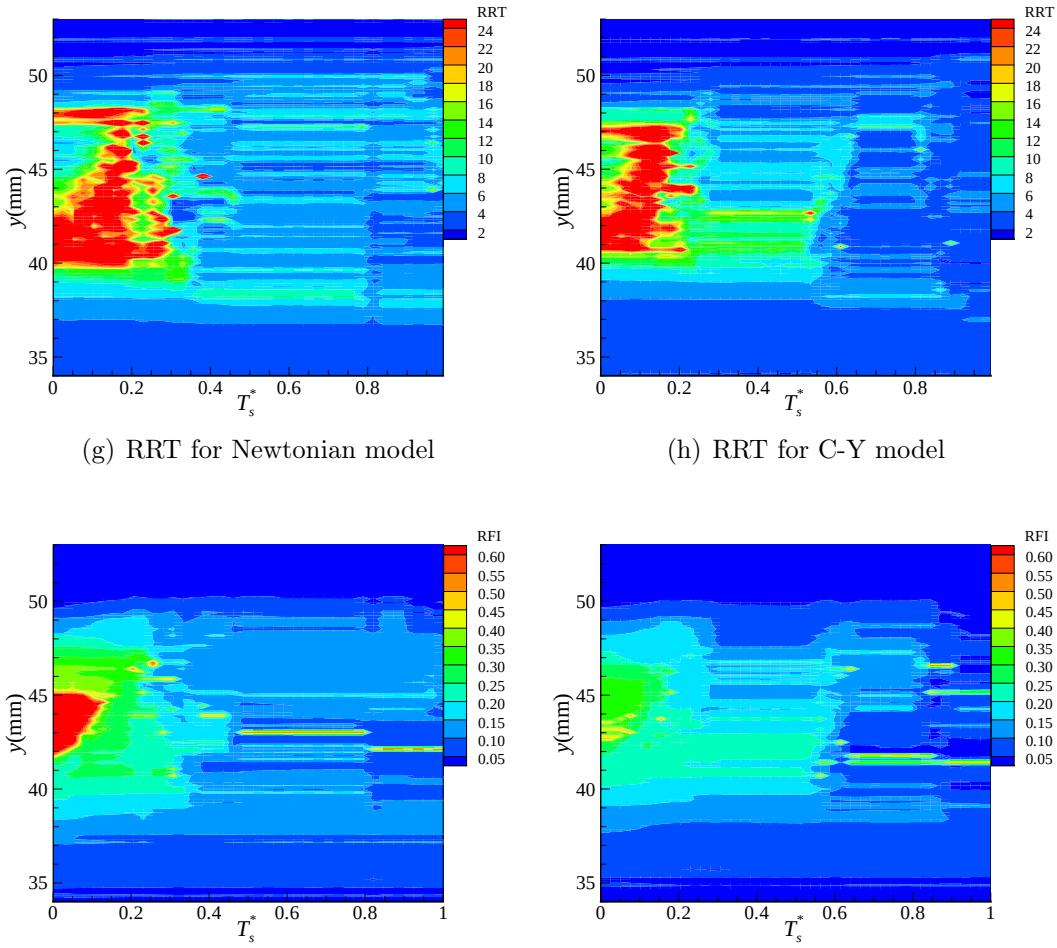

(g) RRT for Newtonian model

(h) RRT for C-Y model

(i) RFI for Newtonian model

(j) RFI for C-Y model

Figure 11.7: Near-wall haemodynamics over the development of the stenosis using TAWSS as a marker: (a) and (b) $\overline{u^{(1)}}$; (c) and (d) $\overline{u_t^{(1)}}$; (e) and (f) OSI; (g) and (h) RRT; and (i) and (j) RFI, on the outer wall of the ECA, using a Newtonian model (left column) and non-Newtonian C-Y model (right column).

a number of differences comparing Figures 11.8 (a) and (b), the time averaged near-wall velocity is somewhat lower for the non-Newtonian simulation, particularly for $T_s^* < 0.5$. In the same region in Figures 11.8 (c) and (d); both the magnitude and the extent of negative tangential near-wall flow are reduced for the non-Newtonian model. The magnitude of the OSI in Figures 11.8 (e) and (f) are similar between the Newtonian and non-Newtonian simulations; however the OSI reduces earlier for the non-Newtonian case, suggesting that the oscillatory

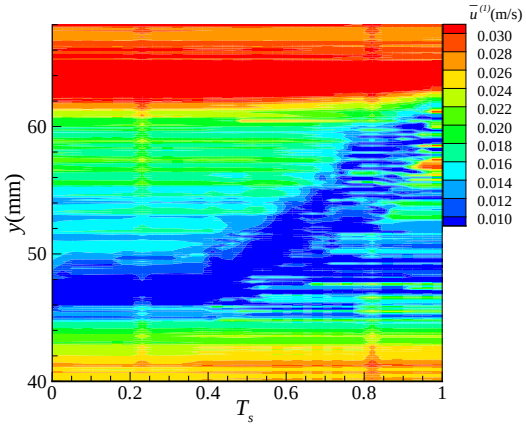

(a) $\overline{u^{(1)}}$ for Newtonian model

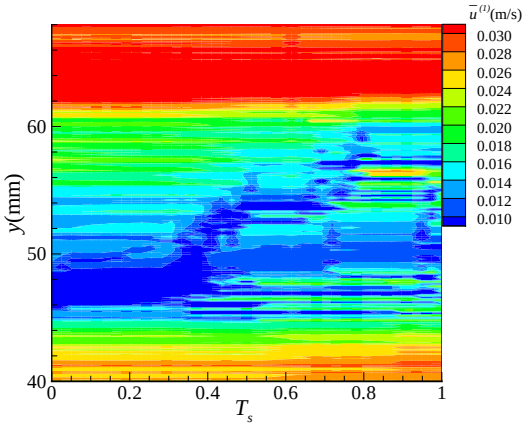

(b) $\overline{u^{(1)}}$ for C-Y model

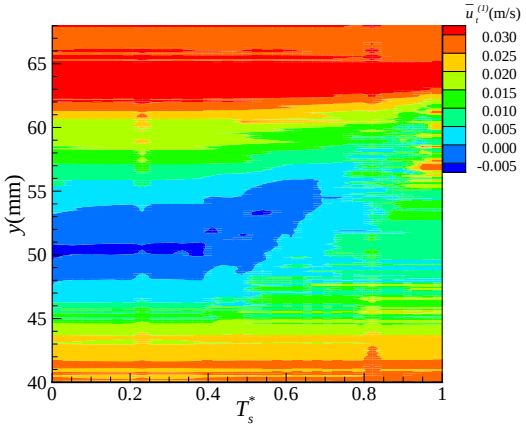

(c) $\overline{u_t^{(1)}}$ for Newtonian model

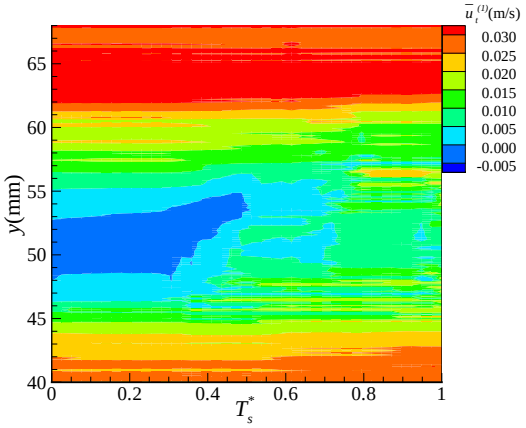

(d) $\overline{u_t^{(1)}}$ for C-Y model

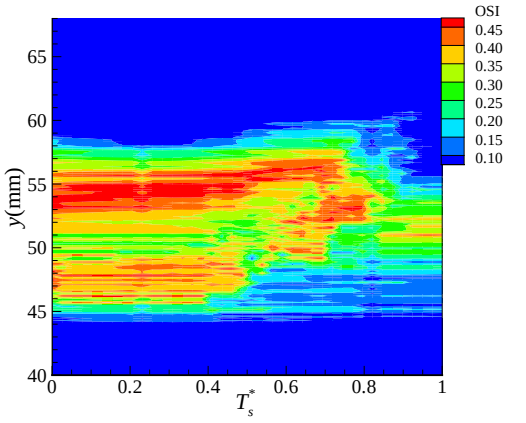

(e) OSI for Newtonian model

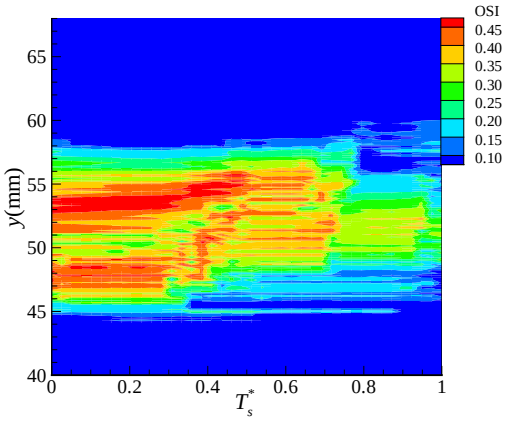

(f) OSI for C-Y model

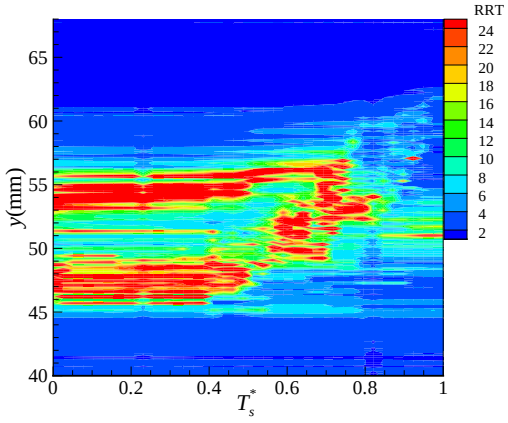

(g) RRT for Newtonian model

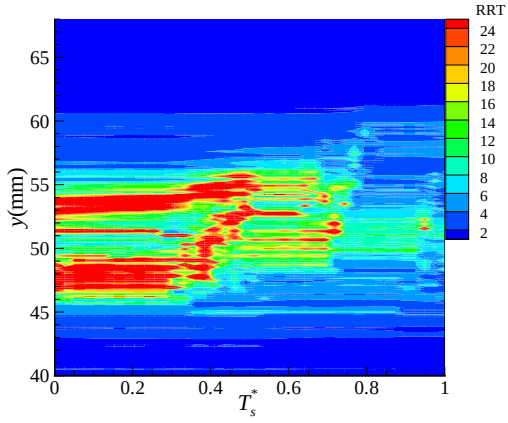

(h) RRT for C-Y model

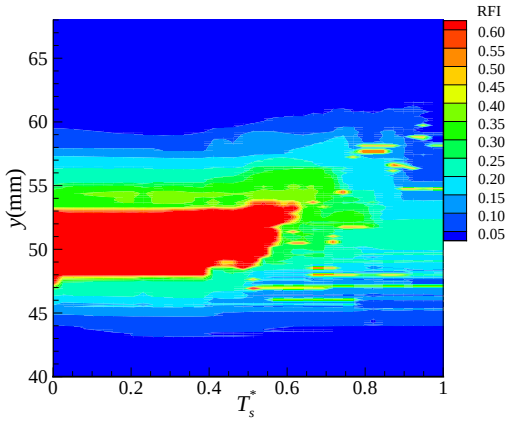

(i) RFI for Newtonian model

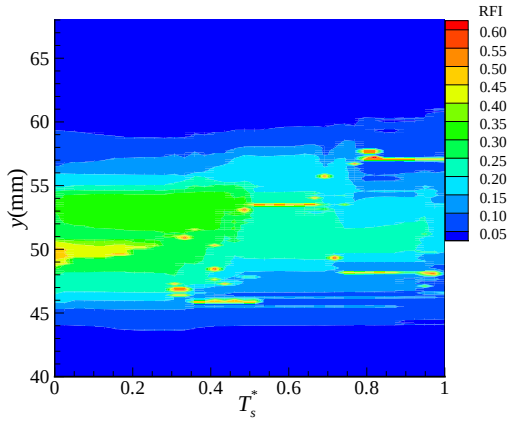

(j) RFI for C-Y model

Figure 11.8: Near-wall haemodynamics over the development of the stenosis using TAWSS as a marker: (a) and (b) $\overline{u^{(1)}}$; (c) and (d) $\overline{u_t^{(1)}}$; (e) and (f) OSI; (g) and (h) RRT; and (i) and (j) RFI, on the outer wall of the ICA, using a Newtonian model (left column) and non-Newtonian C-Y model (right column).

nature of the flow reduces more rapidly. This is mirrored in Figures 11.8 (g) and (h), where the magnitudes are similar, but the RRT reduces earlier for the non-Newtonian case. Figures 11.8 (i) and (j) show the most striking differences: they both show a similar region where reversible flow is occurring; however there is a marked difference in the percentage of the period where reversible flow occurs. In the Newtonian case there is a region 48mm $< y <$ 53mm, where the flow is reversed for over 60% of the period which is maintained until $T_s^* \simeq 0.6$. In the

non-Newtonian case reversible flow typically occurs for no more than 45% of the period and is typically around 30% of the period, for 48mm $< y <$ 53mm and $T_s^* < 0.6$.

11.3 Conclusion

The stenosis formed using both the Newtonian and Non-Newtonian model were fairly similar in terms of the final shape of the geometry; however small differences were observed both in the final geometry and the formation. Differences were also observed in the near wall haemodynamics between the two models. In both the ECA and the ICA the non-Newtonian model reduces the reversible flow in terms of both the special region where it occurs, and its magnitude. There is also a small reduction in the near-wall TA velocity and the oscillatory nature of the flow measured through the OSI.

Chapter 12

Conclusions

The lattice Boltzmann method was applied to model stenosis development in the carotid artery.

12.1 Stenosis model

The main aim of this thesis has been to develop a model to simulate the growth of a stenosis in the carotid artery, based on the local haemodynamics. To this end, a model was developed based on the time averaged near wall velocity. The model involved two lattice-based parameters and the model was evaluated to find a range for these parameters over which the stenosis developed in an independent manner. Using parameters in this range the model was able to replicate stenosed geometries similar to MRI images in the literature; with haemodynamics with the same features as have been observed in alternative CFD [199] and also in experimental results in a phantom [197–199].

12.2 Wall haemodynamics

After establishing the viability of the model, it was used to provide details of how the haemodynamics changes during stenosis development. The results indicated

how the instantaneous near wall velocity and WSS vary over a period at various stages of stenosis development. Time averaged wall quantities relating to the velocity, TAWSS, OSI, RRT, RFI and O:WS, the ratio of OSI:TAWSS, were considered in terms of how they change as the stenosis forms. As the stenosis develops it progresses mainly downstream in such a way that regions of low TA velocity, low TAWSS, high OSI and high RRT are maintained around the leading edge. As the stenosis grows it develops in the region where low velocity and vortex motion was observed in the healthy artery, thus reducing and eventually eliminating the vortex motion.

12.3 Haemodynamic markers

The original model used the position of minimum time averaged near-wall velocity as a marker for stenosis development. Alternative haemodynamic markers were considered. When the oscillatory shear index (OSI) was applied as a marker, the stenosis was found to develop in a significantly different manner to all the other markers considered, and was also different to literature examples of imaged arteries with different levels of stenosis. Regions of high OSI are known to occur in regions of the artery where autherosclerosis occurs. These two features are often considered to be related making OSI a marker for stenosis development. However, the simulations presented here indicate that OSI on its own is not a good marker for stenosis development. For all the other markers considered, the resulting geometry was comparable with literature observations [193–196], but with noticeable differences between some of the markers. Although differences were observed, none of the stenoses produced were non-realistic and so it was not possible to differentiate between the suitability of the different markers. Within these markers the time-averaged near-wall velocity magnitude, the time-average of the magnitude of the tangential component of this velocity and the TAWSS

were all found to act in an almost identical manner. Two other markers O:WS and RRT also produced very similar stenosis development.

12.4 Non-Newtonian model

Simulations were also run using the non-Newtonian C-Y model. This was done for two markers TAWSS and O:WS. In both cases differences were observed between the Newtonian and non-Newtonian models in terms of both the manner in which the stenosis developed and the near-wall haemodynamics. Although these variations in the quantities of measure were not large, they did indicate that including the non-Newtonian nature of blood, through the C-Y model, does have an influence on the modelling of the stenosis.

12.5 Future Directions

In this thesis, attention has primarily been given to modelling stenosis development in a human carotid artery. This has been due to the susceptibility of the carotid bifurcation to atherosclerosis. There are a number of other arteries which are similarly susceptible to this disease, in particular the human aorta. The comparison of haemodynamics between stenosed and stented arteries could be a further area for research.

The C-Y model has been used in this Thesis to simulate the non-Newtonian blood. This is a commonly used model for simulating the blood flow; however, it is not the only one and alternatives could be considered.

Development of a 3D model would enable the secondary flows in the artery to be assessed and their effect on stenosis development to be evaluated.

Appendix A

A.1 Hamiltonian of a system

At a microdynamic scale, a fluid can be resembled to a N-particle system, described by a Hamiltonian of the N-particle system, $H = H(\mathbf{x}, \mathbf{p}, t)$ [52], with $(\mathbf{x}, \mathbf{p})$ the coordinates of a 3N space in a momentum phase system such that $\mathbf{x} = (\mathbf{x}_1, ..., \mathbf{x}_N)$ are the 3N coordinates of a spatial system and $\mathbf{p} = (\mathbf{p}_1, ..., \mathbf{p}_N)$ are the 3N coordinates of a conjugate momentum system. H is the total energy of the system, sum of kinetic energy and the potential energy due to particles interactions. With respect to the Hamiltonian of the system, the motion of particles can be described by:

$$\dot{\mathbf{x}}_i = \frac{\partial H}{\partial \mathbf{p}_i} \tag{A.1}$$

where $\mathbf{p}_i$ is the momentum and $\mathbf{x}_i$ is the position in the 3-D space of the i particle, correspondingly with $i = 1, .., N$ and

$$\dot{\mathbf{p}}_i = \frac{\partial H}{\partial \mathbf{x}_i} \tag{A.2}$$

A.2 Collision integral

The $Q(f, f)$ is the collision integral describing the two particles situation accompanying their collision. It is set assuming that a two-particles system of input

velocities $(\mathbf{u}, \mathbf{u}_1)$ is moving after the collision with a pair of (output) velocities $(\mathbf{u}', \mathbf{u}_1')$. The differential cross-section $\sigma(\Omega)$ results from the two-particles collision. The $Q(f, f)$ is expressed as:

$$Q(f, f) = \int du \int d\Omega \sigma(\Omega) \left|\mathbf{u} - \mathbf{u}_1\right| \left[f(\mathbf{u}')f(\mathbf{u}_1') - f(\mathbf{u})f(\mathbf{u}_1)\right] \tag{A.3}$$

A.3 Summation properties

$$\Sigma_i e_{ix} e_{iy} = 6e^2 \delta_{xy}, \tag{A.4}$$

with δ_{xy} the Kronecher delta:

$$\delta_{xy} = \begin{cases} 1 & x = y \\ 0 & x \neq y \end{cases}$$

A.4 Chapman-Enskog expansion

The Chapman-Enskog expansion for a function p_i is written:

$$p_i = \Sigma_{n=0}^{\infty} \epsilon^{n+1} p_i^n = p_i^{(0)} + \epsilon p_i^{(1)} + \epsilon^2 p_i^{(2)} + ..., \tag{A.5}$$

with $\epsilon = t_c \dfrac{U}{L}$ the ratio of the free path to the characteristic length [21,52] called the Knudsen number. However after considering an integer n' such that $n' + m = n$, the p_i^n is equivalent to:

$$p_i^{(n)} = \Sigma_{m=0}^{(n-1)} \partial_t^{(m)} p_i^{(n-1-m)}. \tag{A.6}$$

However, in case of using the terms p_i^{eq} and p_i^{neq} we re-write the eq. A.5:

$$p_i = p_i^{eq} + p_i^{neq}, \tag{A.7}$$

with $p_i^{(eq)} = p_i^{(0)}$ and $p_i^{(neq)} = \epsilon p_i^{(1)} + \epsilon p_i^{(2)} + .. + \epsilon^{(n-1)} p_i^{(n-1)}$

Product rules may be used in the Chapman-Enskog expansion to write a derivative: $\frac{\partial \rho u_\alpha u_\beta}{\partial t_1}$.

Assuming that we have a distribution function $f_i = f_i\left(\mathbf{x}(a).t(a)\right)$, we can write the total differential of f_i in a as:

$$\frac{df_i}{da} = \left(\frac{\partial f_i}{\partial t}\right)\frac{dt}{da} + \left(\frac{\partial f_i}{\partial x_a}\right)\frac{dx_a}{da} - \frac{1}{\tau}\left(f_i - f_i^{(0)}\right). \tag{A.8}$$

A.5 Ethic Review

University of Portsmouth

Certificate of Ethics Review

Project Title:	Simulation of the Haemodynamic properties of the carotid artery
User ID:	656452
Name:	Aikaterini Stamou
Application Date:	26/11/2015 14:38:28

You must download your referral certificate, print a copy and keep it as a record of this review.

The FEC representative for the School of Engineering is Giles Tewkesbury

It is your responsibility to follow the University Code of Practice on Ethical Standards and any Department/School or professional guidelines in the conduct of your study including relevant guidelines regarding health and safety of researchers including the following:

- University Policy
- Safety on Geological Fieldwork

It is also your responsibility to follow University guidance on Data Protection Policy:

- General guidance for all data protection issues
- University Data Protection Policy

SchoolOrDepartment: ENG
PrimaryRole: Other
SupervisorName: Dr James M. Buick
HumanParticipants: No
PhysicalEcologicalDamage: No
HistoricalOrCulturalDamage: No
InvolvesAnimals: No
HarmfulToThirdParties: No
OutputsPotentiallyAdaptedAndMisused: No
Confirmation-ConsideredDataUse: Confirmed
Confirmation-ConsideredImpactAndMitigationOfPontentialMisuse: Confirmed
Confirmation-ActingEthicallyAndHonestly: Confirmed

Supervisor Review

As supervisor, I will ensure that this work will be conducted in an ethical manner in line with the University Ethics Policy.

Supervisor signature: James M. Buick
Date:

Certificate Code: F67A-DAD2-89FB-2424-E954-BA39-B404-FBE8 Page 1

Figure A.1: Ethical Committee Approval

FORM UPR16

Research Ethics Review Checklist

University of **Portsmouth**

Please include this completed form as an appendix to your thesis (see the Postgraduate Research Student Handbook for more information

Postgraduate Research Student (PGRS) Information			**Student ID:**	UP656452
PGRS Name:	Aikaterini Stamou			
Department:	Engineering	**First Supervisor:**	Dr James M. Buick	
Start Date: (or progression date for Prof Doc students)				

Study Mode and Route:	Part-time ☐	MPhil ☐	MD ☐
	Full-time ☒	PhD ☐	Professional Doctorate ☐

Title of Thesis:	Development and assessment of haemodynamic based numerical model for stenosis growth in the carotid artery.
Thesis Word Count: (excluding ancillary data)	42000

If you are unsure about any of the following, please contact the local representative on your Faculty Ethics Committee for advice. Please note that it is your responsibility to follow the University's Ethics Policy and any relevant University, academic or professional guidelines in the conduct of your study

Although the Ethics Committee may have given your study a favourable opinion, the final responsibility for the ethical conduct of this work lies with the researcher(s).

UKRIO Finished Research Checklist:
(If you would like to know more about the checklist, please see your Faculty or Departmental Ethics Committee rep or see the online version of the full checklist at: http://www.ukrio.org/what-we-do/code-of-practice-for-research/)

a) Have all of your research and findings been reported accurately, honestly and within a reasonable time frame?	YES ☒ NO ☐
b) Have all contributions to knowledge been acknowledged?	YES ☒ NO ☐
c) Have you complied with all agreements relating to intellectual property, publication and authorship?	YES ☒ NO ☐
d) Has your research data been retained in a secure and accessible form and will it remain so for the required duration?	YES ☒ NO ☐
e) Does your research comply with all legal, ethical, and contractual requirements?	YES ☒ NO ☐

Candidate Statement:

I have considered the ethical dimensions of the above named research project, and have successfully obtained the necessary ethical approval(s)

Ethical review number(s) from Faculty Ethics Committee (or from NRES/SCREC):	F67A-DAD2-B9FB-2424-E954-BA39-B404-FBE8

If you have *not* submitted your work for ethical review, and/or you have answered 'No' to one or more of questions a) to e), please explain below why this is so:

UPR16 – August 2015

Signed *(PGRS)*:	Aikaterini Stamou	**Date:** 21/01/16

Bibliography

[1] Ala Alwan. *Global status report on noncommunicable diseases 2010.* World Health Organization, 2011.

[2] The World Health Report. WHO publications, 2005.

[3] Agostino Gnasso, Concetta Irace, Claudio Carallo, Maria Serena De Franceschi, Corradino Motti, Pier Luigi Mattioli, and Arturo Pujia. In vivo association between low wall shear stress and plaque in subjects with asymmetrical carotid atherosclerosis. *Stroke*, 28(5):993–998, 1997.

[4] Peter H Stone, Ahmet U Coskun, Scott Kinlay, Maureen E Clark, Milan Sonka, Andreas Wahle, Olusegun J Ilegbusi, Yerem Yeghiazarians, Jeffrey J Popma, John Orav, et al. Effect of endothelial shear stress on the progression of coronary artery disease, vascular remodeling, and in-stent restenosis in humans in vivo 6-month follow-up study. *Circulation*, 108(4):438–444, 2003.

[5] Yiannis S. Chatzizisis, Ahmet Umit Coskun, Michael Jonas, Elazer R. Edelman, Charles L. Feldman, and Peter H. Stone. Role of endothelial shear stress in the natural history of coronary Atherosclerosis and vascular remodelingmolecular, cellular, and vascular behavior. *Journal of the American College of Cardiology*, 49(25):2379–2393, 2007.

[6] Yiannis S Chatzizisis, Ahmet U Coskun, Michael Jonas, Elazer R Edelman, Peter H Stone, and Charles L Feldman. Risk stratification of individual coronary lesions using local endothelial shear stress: a new paradigm for managing coronary artery disease. *Current Opinion in Cardiology*, 22(6):552–564, 2007.

[7] Colin G Caro. Discovery of the role of wall shear in Atherosclerosis. *Arteriosclerosis, Thrombosis, and Vascular Biology*, 29(2):158–161, 2009.

[8] L Goubergrits, K Affeld, J Fernandez-Britto, and L Falcon. Atherosclerosis and flow in carotid arteries with authentic geometries. *Biorheology*, 39(3-4):519–524, 2001.

[9] C. K. Zarins, Giddens D. P, B. K. Bharadvaj, V. S. Sottiurai, R. F. Mabon, and S. Glagov. Carotid bifurcation Atherosclerosis, quantitative correlation of plaque localisation with flow velocity profiles and wall shear stress. *Circulation Research*, 53:502–514, 1983.

[10] D.N. Ku, D.P. Giddens C.K. Zarins, and S. Glagov. Pulsatile flow and Atherosclerosis in the human carotid bifurcation: Positive correlation between plaque location and low and oscillating shear stress. *Arteriosclerosis*, 5(3):293–302, 1985.

[11] Caroline Cheng, Dennie Tempel, Rien van Haperen, Arjen van der Baan, Frank Grosveld, Mat JAP Daemen, Rob Krams, and Rini de Crom. Atherosclerotic lesion size and vulnerability are determined by patterns of fluid shear stress. *Circulation*, 113(23):2744–2753, 2006.

[12] Oguz K Baskurt and Herbert J Meiselman. Blood rheology and hemodynamics. In *Seminars in thrombosis and hemostasis*, volume 29, pages 435–450. Copyright© 2003 by Thieme Medical Publishers, Inc., 333 Seventh

Avenue, New York: Stratton Intercontinental Medical Book Corporation, c1974-, 2003.

[13] Shu Chien. Biophysical behavior of red cells in suspensions. *The red blood cell*, 2(4):1031–1133, 1975.

[14] Hiromi Sakai, Atsushi Sato, Naoto Okuda, Shinji Takeoka, Nobuji Maeda, and Eishun Tsuchida. Peculiar flow patterns of RBCs suspended in viscous fluids and perfused through a narrow tube (25 μm). *American Journal of Physiology-Heart and Circulatory Physiology*, 297(2):H583–H589, 2009.

[15] OK Başkurt, M Bor-Küçükatay, and Ö Yalçın. The effect of red blood cell aggregation on blood flow resistance. *Biorheology*, 36:447–452, 1999.

[16] DE Brooks, JW Goodwin, and GV Seaman. Interactions among erythrocytes under shear. *Journal of Applied Physiology*, 28(2):172–177, 1970.

[17] Yan Geng, Weien Yuan, Fei Wu, Jingle Chen, Mu He, and Tuo Jin. Formulating erythropoietin-loaded sustained-release PLGA microspheres without protein aggregation. *Journal of Controlled Release*, 130(3):259–265, 2008.

[18] KMD Hell, A Balzereit, U Diebold, and HD Bruhn. Importance of blood viscoelasticity in Arteriosclerosis. *Angiology*, 40(6):539–546, 1989.

[19] Shu Chien, Shunuchi Usami, Robert J Dellenback, and Magnus I Gregersen. Shear-dependent deformation of erythrocytes in rheology of human blood. *American Journal of Physiology–Legacy Content*, 219(1):136–142, 1970.

[20] Joaquim Peiró and Spencer Sherwin. Finite difference, finite element and finite volume methods for partial differential equations. In *Handbook of Materials Modeling*, pages 2415–2446. Springer, 2005.

[21] Sauro Succi. *The Lattice Boltzmann equation: for fluid dynamics and beyond*. Oxford University Press, 2001.

[22] MC Sukop. *DT Thorne, Jr. Lattice Boltzmann Modeling Lattice Boltzmann Modeling*. Springer, 2006.

[23] R Benzi, S Succi, and M Vergassola. The Lattice Boltzmann equation: theory and applications. *Phys Rep*, 222:145–197, dec 1992.

[24] S Chen and GD Doolen. Lattice Boltzmann method for fluid flows. *Annu. Rev. Fluid. Mech.*, 30:329–364, 1998.

[25] Olgierd Cecil Zienkiewicz, Robert Leroy Taylor, Olgierd Cecil Zienkiewicz, and Robert Lee Taylor. *The finite element method*, volume 3. McGraw-Hill London, 1977.

[26] Barna Aladar Szabo and Ivo Babuška. *Finite element analysis*. John Wiley & Sons, 1991.

[27] Jiri Blazek. *Computational Fluid Dynamics: Principles and Applications:(Book with accompanying CD)*. Elsevier, 2005.

[28] TJ Chung. *Computational Fluid Dynamics*. Cambridge University Press, 2010.

[29] James M. Buick, M. Atig, D. J. Skulina, D. M. Campbell, J. P. Dalmont, and J. Gilbert. Investigation of non-linear acoustic losses at the open end of a tube. *The Journal of the Acoustical Society of America*, 129(3):1261–1272, 2011.

[30] Amit Gupta and Ranganathan Kumar. Lattice Boltzmann simulation to study multiple bubble dynamics. *International Journal of Heat and Mass Transfer*, 51(21):5192–5203, 2008.

[31] Irina Ginzburg. A free-surface Lattice Boltzmann method for modelling the filling of expanding cavities by Bingham fluids. *Philosophical Transactions*

of the Royal Society of London A: Mathematical, Physical and Engineering Sciences, 360(1792):453–466, 2002.

[32] C Manwart, U Aaltosalmi, A Koponen, R Hilfer, and J Timonen. Lattice-Boltzmann and finite-difference simulations for the permeability for three-dimensional porous media. *Physical Review E*, 66(1):016702, 2002.

[33] Huabing Li, Haiping Fang, Zhifang Lin, ShiXiong Xu, and Shiyi Chen. Lattice Boltzmann simulation on particle suspensions in a two-dimensional symmetric stenotic artery. *Physical Review E*, 69(3):031919, 2004.

[34] J Boyd and J M Buick. Three-dimensional modelling of the human carotid artery using the Lattice Boltzmann method: I. Model and velocity analysis. *Physics in Medicine and Biology*, 53(20):5767–5779, 2008.

[35] Junfeng Zhang, Paul C. Johnson, and Aleksander S. Popel. Red blood cell aggregation and dissociation in shear flows simulated by Lattice Boltzmann method. *Journal of Biomechanics*, 41(1):47 – 55, 2008.

[36] MM Dupin, I Halliday, CM Care, and LL Munn. Lattice Boltzmann modelling of blood cell dynamics. *International Journal of Computational Fluid Dynamics*, 22(7):481–492, 2008.

[37] B Min Yun, LP Dasi, CK Aidun, and AP Yoganathan. Computational modelling of flow through prosthetic heart valves using the entropic Lattice-Boltzmann method. *Journal of Fluid Mechanics*, 743:170–201, 2014.

[38] Masaaki Tamagawa and Sumiaki Matsuo. Predictions of thrombus formation using Lattice Boltzmann method (modeling of adhesion force for particles to wall). *JSME International Journal Series C*, 47(4):1027–1034, 2004.

[39] Masaaki Tamagawa, Hiroaki Kaneda, Miki Hiramoto, and Sho Nagahama. Simulation of thrombus formation in shear flows using lattice Boltzmann method. *Artificial Organs*, 33(8):604–610, 2009.

[40] SE Harrison, SM Smith, J Bernsdorf, DR Hose, and PV Lawford. Application and validation of the Lattice Boltzmann method for modelling flow-related clotting. *Journal of Biomechanics*, 40(13):3023–3028, 2007.

[41] Jörg Bernsdorf, Sarah E Harrison, Stephen M Smith, Patricia V Lawford, and D Rodney Hose. Applying the Lattice Boltzmann technique to biofluids: A novel approach to simulate blood coagulation. *Computers & Mathematics with Applications*, 55(7):1408–1414, 2008.

[42] Gilead Moiseyev and Pinhas Z. Bar-Yoseph. No need for particle tracing: From accumulating fluid properties to novel blood coagulation model in the Lattice Boltzmann method. *Journal of Biomechanics*, 43(5):864 – 870, 2010.

[43] H Karimpour and E Javdan. Simulation of stenosis growth in the carotid artery by Lattice Boltzmann method. *Journal of Mechanics in Medicine and Biology*, 14(02), 2014.

[44] J Goodfellow. *Molecular Dynamics*. Macmillan Press, 1991.

[45] S Chapman and TG Cowling. *The Mathematical Theory of Non-uniform Gases: An Account of the Kinetic Theory of Viscosity, Thermal Conduction and Diffusion in Gases*. Cambridge Mathematical Library. Cambridge University Press, 1970.

[46] Bruce E Poling, John M Prausnitz, John P O'connell, et al. *The properties of gases and liquids*, volume 5. McGraw-Hill New York, 2001.

[47] WG Vincenti, CH Kruger, and Jr. *Introduction to Physical Gas Dynamics*. John Wiley and Sons, New York, 1965. 376.

[48] J Dupuy and A Dianoux. *Microscopic Structure and Dynamics of Liquids*. Plenum Press, 1978.

[49] Joel Koplik and Jayanth R Banavar. Molecular dynamics of interface rupture. *Physics of Fluids A: Fluid Dynamics (1989-1993)*, 5(3):521–536, 1993.

[50] Wei Kang. Molecular dynamics simulations and microscopic hydrodynamics of nanoscale liquid structures. *https://smartech.gatech.edu/*, 2008.

[51] S Harris. *An Introduction to the Theory of the Boltzmann Equation*. Holt, Rimehart and Winston INC., 1970.

[52] S Wolfram. Universality and complexity in cellular automata. *Physica D*, 10:1–35, 1984.

[53] NN Bogoliubov. Problems of a Dynamical Theory in Statistical Physics [in Russian], gostekhizdat, moscow (1946). *English transl., North-Holland, Amsterdam*, 1962.

[54] C Cercignani and K Lanckau. The Boltzmann equation and its applications. New York etc., Springer-Verlag 1988. xiii. 455 pp., 51 figs., dm 98,–. isbn 3–540-96637-4 (Applied Mathematical Sciences 67). *ZAMM-Journal of Applied Mathematics and Mechanics/Zeitschrift für Angewandte Mathematik und Mechanik*, 69(11):423–423, 1989.

[55] A Ya Ender and IA Ender. Polynomial expansions for the isotropic Boltzmann equation and invariance of the collision integral with respect to the choice of basis functions. *Physics of Fluids (1994-present)*, 11(9):2720–2730, 1999.

[56] VI Kolobov, RR Arslanbekov, VV Aristov, AA Frolova, and SA Zabelok. Unified solver for rarefied and continuum flows with adaptive mesh and algorithm refinement. *Journal of Computational Physics*, 223(2):589–608, 2007.

[57] Robert T Glassey. *The Cauchy problem in kinetic theory*. SIAM, 1996.

[58] Hare Krishna and Pramendra Singh Pundir. Discrete Maxwell distribution. *Interstat*, 2007.

[59] George E Uhlenbeck and Leonard S Ornstein. On the theory of the Brownian motion. *Physical review*, 36(5):823, 1930.

[60] P. L. Bhatnagar, E. P. Gross, and M. Krook. A model for collision processes in gases. I: small amplitude processes in charged and neutral one-component system. *Physical Review*, 94:511–525, 1954.

[61] John Von Neumann, Arthur W Burks, et al. Theory of self-reproducing automata. *IEEE Transactions on Neural Networks*, 5(1):3–14, 1966.

[62] Howard Gutowitz. *Cellular automata: theory and experiment*, volume 45. MIT press, 1991.

[63] Tommaso Toffoli and Norman Margolus. *Cellular automata machines: a new environment for modeling*. MIT press, 1987.

[64] J Hardy, Y Pomeau, and de Pazzis O. Time evolution of a two-dimensional model system. I. Invariant states and time correlation functions. *Journal of Mathematical Physics*, 14:1746–1759, 1973.

[65] J Hardy, O De Pazzis, and Yves Pomeau. Molecular dynamics of a classical lattice gas: Transport properties and time correlation functions. *Physical Review A*, 13(5):1949, 1976.

[66] Uriel Frisch, Brosl Hasslacher, and Yves Pomeau. Lattice-gas automata for the Navier-Stokes equation. *Physical Review Letters*, 56(14):1505, 1986.

[67] U. Frisch, D. d' Humières, B. Hasslacher, P. Lallemand, Y. Pomeau, and J.-P. Rivet. Lattice gas Hydrodynamics in two and three dimensions. *Complex Systems*, 1:649–707, 1987.

[68] J. M. Buick. *Lattice Boltzmann Methods in Interfacial Wave Modelling*. PhD thesis, The University of Edinburgh, 1997.

[69] Bruce M Boghosian, Jeffrey Yepez, Francis J Alexander, and Norman H Margolus. Integer lattice gases. *Physical Review E*, 55(4):4137, 1997.

[70] GR McNamara and G Zanetti. Use of the Boltzmann Equation to Simulate Lattice-Gas Automata. *Phys Rev Lett*, 61(20):2332–2335, 1988.

[71] YH Qian, D D'Humiéres, and P Lallemand. Lattice BGK Models for Navier-StokesEquation. *EPL Europhysics Letters*, 17(6):479–484, 1992.

[72] PL Bhatnagar, EP Gross, and M Krook. A Model for Collision Processes in Gases. I. Small Amplitude Processes in Charged and Neutral One-Component Systems. *Phys Rev*, 94(3):511–525, May 1954.

[73] DH Rothman and S Zaleski. *Lattice-gas cellular automata: simple models of complex hydrodynamics*, volume 5. Cambridge University Press, 2004.

[74] Y. H. Qian, D. d'Humières, and P. Lallemand. Lattice BGK models for Navier-Stokes equation. *Europhysics Letters*, 17(6):479–484, 1992.

[75] Xiaoyi He and Li-Shi Luo. Lattice Boltzmann model for the incompressible navier–stokes equation. *Journal of statistical Physics*, 88(3-4):927–944, 1997.

[76] TS Lee, Haibo Huang, and C Shu. An axisymmetric incompressible Lattice Boltzmann model for pipe flow. *International Journal of Modern Physics C*, 17(05):645–661, 2006.

[77] Z. Guo, C. Zheng, and B. Shi. An extrapolation method for boundary conditions in Lattice Boltzmann method. *Physics of Fluids*, 14(6):2007–2010, 2002.

[78] J. Boyd, J.M. Buick, J.A. Cosgrove, and P. Stansell. Application of the Lattice Boltzmann model to simulated stenosis growth in a two-dimensional carotid artery. *Physics and Medicine in Biology*, 50:4783–4796, 2005.

[79] J Boyd and J M Buick. Comparison of Newtonian and non-Newtonian flows in a two-dimensional carotid artery model using the Lattice Boltzmann method. *Physics in Medicine and Biology*, 52(20):6215–6228, 2007.

[80] J Boyd and JM Buick. Changes in velocity profiles in a two dimensional carotid artery geometry in response to changes in velocity waveforms and a simulated stenosis growth: A Lattice Boltzmann Simulation. *International Journal of Mathematics and Computers in Simulation*, 1(2):160–166, 2007.

[81] Jonas Latt. *Hydrodynamic limit of Lattice Boltzmann equations*. PhD thesis, University of Geneva, 2007.

[82] Gennady Samoradnitsky and Murad S Taqqu. *Stable non-Gaussian random processes: stochastic models with infinite variance*, volume 1. CRC Press, 1994.

[83] J. M. V. A. Koelman. A simple Lattice Boltzmann scheme for Navier-Stokes fluid flow. *Europhysics Letters*, 15(6):603–607, 1991.

[84] Shiyi Chen and Gary D. Doolen. Lattice Boltzmann Method for fluid flows. *Annual Review of Fluid Mechanics*, 30(1):329–364, 1998.

[85] A. Artoli. Mesoscopic computational haemodynamics. Technical report, University of Amsterdam, October 2003.

[86] Q. Zou and X. He. On pressure and velocity flow boundary conditions and bounceback for the Lattice Boltzmann bgk model. *Physics of Fluids*, 9:1591–1609, 1997.

[87] D. P. Ziegler. Boundary conditions for Lattice Boltzmann simulations. *Journal of Statistical Physics*, 71 (5/6):1171–1177, 1993.

[88] Anthony JC Ladd. Numerical simulations of particulate suspensions via a discretized Boltzmann equation. Part 1. Theoretical foundation. *Journal of Fluid Mechanics*, 271:285–309, 1994.

[89] Anthony JC Ladd. Numerical simulations of particulate suspensions via a discretized Boltzmann equation. Part 2. Numerical results. *Journal of Fluid Mechanics*, 271:311–339, 1994.

[90] T. Inamuro, M. Yoshino, and F. Ogino. A non-slip boundary condition for Lattice Bolltzmann simulations. *Physics of Fluids*, 7:2928–38, 1996.

[91] I. Ginzbourg and P. M. Adler. Boundary condition analysis for three-dimensional Lattice Boltzmann model. *Le Journal de physique*, 4:191–214, 1994.

[92] David R Noble, Shiyi Chen, John G Georgiadis, and Richard O Buckius. A consistent hydrodynamic boundary condition for the Lattice Boltzmann method. *Physics of Fluids (1994-present)*, 7(1):203–209, 1995.

[93] M. Neal. *A Study of the Brass Instrument Lip Reed Mechanism using Artificial Lips and Lattice Boltzmann Flow Simulations*. PhD thesis, University of Edinburgh, Edinburgh, Scotland, 2002.

[94] J. Boyd, J.M. Buick, J.A. Cosgrove, and P. Stansell. Application of the Lattice Boltzmann method to arterial flow simulation: Investigation of boundary conditions for complex arterial geometries. *Australasian Physical and Engineering Sciences in Medicine*, 27(4):147–152, 2004.

[95] C K Zarins, D P Giddens, B K Bharadvaj, V S Sottiurai, R F Mabon, and S Glagov. Carotid bifurcation Atherosclerosis. quantitative correlation of plaque localization with flow velocity profiles and wall shear stress. *Circulation Research*, 53(4):502–514, 1983.

[96] David N Ku, Don P Giddens, Christopher K Zarins, and Seymour Glagov. Pulsatile flow and Atherosclerosis in the human carotid bifurcation. positive correlation between plaque location and low oscillating shear stress. *Arteriosclerosis, Thrombosis, and Vascular Biology*, 5(3):293–302, 1985.

[97] D.W. Holdsworth, C.J.D. Norley, R. Frayne, D.A. Steinman, and B.K. Rutt. Characterisation of common carotid artery blood-flow waveforms in normal human subjects. *Jounal of Physiological Measurements*, 20:219–240, 1999.

[98] Womersley's theory for pulsating flow in straight rigid tubes. Retrieved 6 May 2004 from http://bio-e.epfl.ch/jahia/enginename/filemanager/site/igbm/pid /14287/. 2004.

[99] Malcolm M Cross. Rheology of non-Newtonian fluids: a new flow equation for pseudoplastic systems. *Journal of Colloid Ccience*, 20(5):417–437, 1965.

[100] Pierre J Carreau. Rheological equations from molecular network theories. *Transactions of The Society of Rheology (1957-1977)*, 16(1):99–127, 1972.

[101] KY Yasuda, RC Armstrong, and RE Cohen. Shear flow properties of concentrated solutions of linear and star branched polystyrenes. *Rheologica Acta*, 20(2):163–178, 1981.

[102] Kazunori Yasuda. A multi-mode viscosity model and its applicability to non-Newtonian fluids. *Journal of Textile Engineering*, 52(4):171–173, 2006.

[103] Aharonov E and Rothman DH. Non-Newtonian flow (through porous media): A Lattice-Boltzmann method. *Geophysical Research Letters*, 20(8):679–682, 1993.

[104] H. B. Li, H. Fang, Z. Lin, S. X. Xu, and S. Chen. Lattice Boltzmann simulation on particle suspensions in a two-dimensional symmetric stenotic artery. *Physical Review E*, 69(3):031919, 2004.

[105] A. M. Artoli, A. G. Hoekstra, and P. M. A. Sloot. Accuracy of 2D pulsatile flow in the Lattice Boltzmann BGK method. In P. M. A. Sloot, C. J. Kenneth Tan, J. J. Dongerra, and A. G. Hoekstra, editors, *Proceedings of the International Conference in Computational Science (ICCS) 2002*, pages 361–370, Amsterdam, Holland, 2002.

[106] DS Sankar and U Lee. Two-fluid Casson model for pulsatile blood flow through stenosed arteries: A theoretical model. *Communications in Nonlinear Science and Numerical Simulation*, 15(8):2086–2097, 2010.

[107] Chen-Hao Wang and Jeng-Rong Ho. A Lattice Boltzmann approach for the non-Newtonian effect in the blood flow. *Computers & Mathematics with Applications*, 62(1):75–86, 2011.

[108] Gr Seminara and P Hall. Centrifugal instability of a Stokes layer: linear theory. In *Proceedings of the Royal Society of London A: Mathematical, Physical and Engineering Sciences*, volume 350, pages 299–316. The Royal Society, 1976.

[109] Philip Hall. The linear stability of flat Stokes layers. In *Proceedings of the Royal Society of London A: Mathematical, Physical and Engineering Sciences*, volume 359, pages 151–166. The Royal Society, 1978.

[110] F. Abraham, M. Behr, and M. Heinkenschloss. Shape optimisation in steady blood flow: A numerical study of non-Newtonian effects. *Computer Methods in Biomechanics and Biomedical Engineering*, 8(2):127–137, 2005.

[111] Javad Alinejad and Keivan Fallah. Lattice-Boltzmann simulation of red blood cell and drug delivery inside the carotid artery. 2015.

[112] Koohyar Vahidkhah and Nasser Fatouraee. Numerical simulation of red blood cell behavior in a stenosed arteriole using the immersed boundary–Lattice Boltzmann method. *International Journal for Numerical Methods in Biomedical Engineering*, 28(2):239–256, 2012.

[113] Junfeng Zhang, Paul C Johnson, and Aleksander S Popel. An immersed boundary Lattice Boltzmann approach to simulate deformable liquid capsules and its application to microscopic blood flows. *Physical Biology*, 4(4):285, 2007.

[114] Junfeng Zhang. Effect of suspending viscosity on red blood cell dynamics and blood flows in microvessels. *Microcirculation*, 18(7):562–573, 2011.

[115] Chenghai Sun, Cristiano Migliorini, and Lance L Munn. Red blood cells initiate leukocyte rolling in postcapillary expansions: a Lattice Boltzmann analysis. *Biophysical Journal*, 85(1):208–222, 2003.

[116] Cristiano Migliorini, YueHong Qian, Hudong Chen, Edward B Brown, Rakesh K Jain, and Lance L Munn. Red blood cells augment leukocyte rolling in a virtual blood vessel. *Biophysical journal*, 83(4):1834–1841, 2002.

[117] Alfons G Hoekstra, Jos vanâĂŹt Hoff, AM Artoli, and Peter MA Sloot. Unsteady flow in a 2D elastic tube with the LBGK method. *Future Generation Computer Systems*, 20(6):917–924, 2004.

[118] H. Fang, Z. Wang, Z. Lin, and M. Liu. Lattice Boltzmann method for simulating the viscous flow in large distensible blood vessels. *Physical Review E*, 65:051925:1–11, 2002.

[119] Jörg Bernsdorf, Sarah E Harrison, Stephen M Smith, Patricia V Lawford, and D Rodney Hose. Numerical simulation of clotting processes: A Lattice Boltzmann application in Medical Physics. *Mathematics and Computers in Simulation*, 72(2):89–92, 2006.

[120] Xing He, Gary Duckwiler, and Daniel J Valentino. Lattice Boltzmann simulation of cerebral artery hemodynamics. *Computers & Fluids*, 38(4):789–796, 2009.

[121] Marco D Mazzeo and Peter V Coveney. HemeLB: A high performance parallel Lattice-Boltzmann code for large scale fluid flow in complex geometries. *Computer Physics Communications*, 178(12):894–914, 2008.

[122] Derek Groen, James Hetherington, Hywel B Carver, Rupert W Nash, Miguel O Bernabeu, and Peter V Coveney. Analysing and modelling the performance of the hemeLB Lattice-Boltzmann simulation environment. *Journal of Computational Science*, 4(5):412–422, 2013.

[123] Mohamed A Itani, Ulf D Schiller, Sebastian Schmieschek, James Hetherington, Miguel O Bernabeu, Hoskote Chandrashekar, Fergus Robertson, Peter V Coveney, and Derek Groen. An automated multiscale ensemble simulation approach for vascular blood flow. *Journal of Computational Science*, 2015.

[124] Caixia Chen, Hudong Chen, David Freed, Richard Shock, Ilya Staroselsky, Raoyang Zhang, A Ümit Coşkun, Peter H Stone, and Charles L Feldman. Simulation of blood flow using extended Boltzmann kinetic approach. *Physica A: Statistical Mechanics and its Applications*, 362(1):174–181, 2006.

[125] L Axner, AG Hoekstra, A Jeays, P Lawford, R Hose, and MAP Sloot. Simulation of time harmonic blood flow in the Mesenteric artery: comparing finite element and Lattice Boltzmann methods. *Biomedical Engineering Online*, 8(23), 2009.

[126] AM Artoli, D Kanhai, HCJ Hoefsloot, AG Hoekstra, and PMA Sloot. Lattice BGK simulations of flow in a symmetric bifurcation. *Future Generation Computer Systems*, 2004.

[127] Maciej Matyka, Zbigniew Koza, and Łukasz Mirosław. Wall orientation and shear stress in the Lattice Boltzmann model. *Computers & Fluids*, 73:115–123, 2013.

[128] T Fukui and K Morinishi. Numerical simulation of blood flows in a vessel with valves based on virtual-flux methods. In *V European Conference on Computational Fluid Dynamics ECCOMAS CFD*, 2010.

[129] R. G. Belleman and P. M. A. Sloot. Simulated vascular reconstruction in a virtual operating theatre. In H. U. Lemke, M. W. Vannier, K. Inamura, A. G. Farman, and K. Doi, editors, *Proceedings of CARS 2001*, pages 928–944, 2001.

[130] M. Krafczyk, J. Tölke, E. Rank, and M. Schulz. Two-dimensional simulation of the fluid-structure interaction using Lattice-Boltzmann methods. *Journal of Computational Structure*, 79:20–31, 2001.

[131] M. Krafczyk, M. Cerrolaza, M. Schulz, and E. Rank. Analysis of 3d transient blood flow passing through and artificial aortic valve by Lattice-Boltzmann methods. *Journal of Biomechanics*, 31:453–462, 1998.

[132] EG Flekkøy. Lattice Bhatnagar-Gross-Krook models for miscible fluids. *Physical Review E*, 47(6):42–47, 1993.

[133] Taha Sochi. Non-Newtonian rheology in blood circulation. *arXiv preprint arXiv:1306.2067*, 2013.

[134] Russell Ross. The pathogenesis of Atherosclerosis: a perspective for the 1990s. *Nature*, 362:801 – 809, 1993.

[135] AR Pries, TW Secomb, and P Gaehtgens. Biophysical aspects of blood flow in the microvasculature. *Cardiovascular Research*, 32(4):654–667, 1996.

[136] Roe E Wells Jr and Edward W Merrill. Influence of flow properties of blood upon viscosity-hematocrit relationships. *Journal of Clinical Investigation*, 41(8):1591, 1962.

[137] Hua-bing Li, Xiao-yang Lu, Hai-ping Fang, and Zhi-fang Lin. Simulation of multi-particle suspensions in a quasi-two-dimensional symmetric stenotic artery with Lattice Boltzmann method. *Progress in Computational Fluid Dynamics, an International Journal*, 5(1-2):65–74, 2004.

[138] Shu Chien. Biophysical behavior of red cells in suspensions. *The Red Blood Cell*, 2(4):1031–1133, 1975.

[139] Juan Mejia, Rosaire Mongrain, and Olivier F Bertrand. Accurate prediction of wall shear stress in a stented artery: Newtonian versus non-Newtonian models. *Journal of Biomechanical Engineering*, 133(7):074501, 2011.

[140] J Boyd, JM Buick, and S Green. Analysis of the Casson and Carreau-Yasuda non-Newtonian blood models in steady and oscillatory flows using the Lattice Boltzmann method. *Physics of Fluids*, 19:093–103, 2007.

[141] D Wang and J Bernsdorf. Lattice Boltzmann simulation of steady non-Newtonian blood flow in a 3D generic stenosis case. *Comput Math Appl*, 58(5):1030–1034, 2009.

[142] Mahmud Ashrafizaadeh and Hani Bakhshaei. A comparison of non-Newtonian models for Lattice Boltzmann blood flow simulations. *Computers & Mathematics with Applications*, 58(5):1045–1054, 2009.

[143] Yanhong Liu. A Lattice Boltzmann model for blood flows. *Applied Mathematical Modelling*, 36(7):2890–2899, 2012.

[144] Ouared R and Chopard B. Lattice Boltzmann Simulations of Blood Flow: Non-Newtonian Rheology and Clotting Processes. *Journal of Statistical Physics*, 121(1–2):209–221, 2005.

[145] Karthik Mukundakrishnan, Portonovo S Ayyaswamy, and David M Eckmann. Finite-sized gas bubble motion in a blood vessel: Non-Newtonian effects. *Physical Review E*, 78(3):036303, 2008.

[146] SC Fu, WWF Leung, and RMC So. A Lattice Boltzmann and immersed boundary scheme for model blood flow in constricted pipes: Part 1–steady flow. *Commun. Comput. Phys.*, 14(1):126–152, 2013.

[147] SC Fu, WWF Leung, and RMC So. A Lattice Boltzmann method based numerical scheme for microchannel flows. *Journal of Fluids Engineering*, 131(8):081401, 2009.

[148] SC Fu and RM C. So. Modeled Lattice Boltzmann equation and the constant-density assumption. *AIAA journal*, 47(12):3038–3042, 2009.

[149] SC Fu, RMC So, and WWF Leung. A Lattice Boltzmann and immersed boundary scheme for model blood flow in constricted pipes: Part 2-pulsatile flow. *Communications in Computational Physics*, 14(1):153–173, 2013.

[150] Xiuying Kang. Assessment of the pulsatile wall shear stress in the stenosed and recanalized carotid bifurcations by the Lattice Boltzmann method. *Computers & Fluids*, 97:156–163, 2014.

[151] XiuYing Kang. Lattice Boltzmann method simulating hemodynamics in the three-dimensional stenosed and recanalized human carotid bifurcations. *Science China Physics, Mechanics & Astronomy*, 58(1):1–8, 2015.

[152] Justin T Saunders, Vijay Nambi, James A de Lemos, Lloyd E Chambless, Salim S Virani, Eric Boerwinkle, Ron C Hoogeveen, Xiaoxi Liu, Brad C Astor, and Thomas H Mosley. Cardiac troponin T measured by a highly sensitive assay predicts coronary heart disease, heart failure, and mortality in the Atherosclerosis risk in communities study. *Circulation*, 123(13):1367–1376, 2011.

[153] Christopher JL Murray and Alan D Lopez. Alternative projections of mortality and disability by cause 1990–2020: Global burden of disease study. *The Lancet*, 349(9064):1498–1504, 1997.

[154] Thomas A Gaziano. Cardiovascular disease in the developing world and its cost-effective management. *Circulation*, 112(23):3547–3553, 2005.

[155] Feng J He, Sonia Pombo-Rodrigues, and Graham A MacGregor. Salt reduction in england from 2003 to 2011: its relationship to blood pressure, stroke and ischaemic heart disease mortality. *BMJ open*, 4(4):e004549, 2014.

[156] Erling Falk. Pathogenesis of Atherosclerosis. *Journal of the American College of Cardiology*, 47(8s1):C7–C12, 2006.

[157] Christopher K Zarins and Charles A Taylor. Hemodynamic factors in Atherosclerosis. *Vascular surgery: a comprehensive review*, pages 97–110, 1998.

[158] Agostino Gnasso, Claudio Carallo, Concetta Irace, Vitaliano Spagnuolo, Giuseppina De Novara, Pier Luigi Mattioli, and Arturo Pujia. Association between intima-media thickness and wall shear stress in common carotid arteries in healthy male subjects. *Circulation*, 94(12):3257–3262, 1996.

[159] Louis R Caplan and Richard Baker. Extrancranial occlusive vascular disease: does size matter? *Stroke*, 11(1):63–66, 1980.

[160] Peter Libby, Yoshihisa Okamoto, Viviane Z Rocha, and Eduardo Folco. Reviews-Inflammation in Atherosclerosis: Transition from theory to practice. *Circulation Journal*, 74(2):213, 2010.

[161] Kristopher S Cunningham and Avrum I Gotlieb. The role of shear stress in the pathogenesis of Atherosclerosis. *Laboratory Investigation*, 85(1):9–23, 2005.

[162] Per Grøttum, Aud Svindland, and Lars Wallrøe. Localization of atherosclerotic lesions in the bifurcation of the main left coronary artery. *Atherosclerosis*, 47(1):55–62, 1983.

[163] Toshihisa Asakura and Takeshi Karino. Flow patterns and spatial distribution of atherosclerotic lesions in human coronary arteries. *Circulation research*, 66(4):1045–1066, 1990.

[164] Mark Fisher and Sherry Fieman. Geometric factors of the bifurcation in carotid atherogenesis. *Stroke*, 21(2):267–271, 1990.

[165] S. Glagov, E. Weisenberg, C. K. Zarin, R. Stankunavicius, and G. J. Kolettis. Compensatory enlargement of human atherosclerotic coronary arteries. *The New England Journal of Medicine*, 316:1371–1375, 1987.

[166] Theodore Papaioannou, Emmanouil N. Karatzis, Manolis Vavuranakis, John P. Lekakis, and Christodoulos Stefanadis. Assessment of vascular wall shear stress and implications for atherosclerotic disease. *International Journal of Cardiology*, 113(1):12–18, 2006.

[167] Gérard Champsaur, Catherine Vedrinne, Stéphane Martinot, François Tronc, Jacques Robin, Jean Ninet, and Michel Franck. Flow-induced release

of endothelium-derived relaxing factor during pulsatile bypass: experimental study in the fetal lamb. *The Journal of Thoracic and Cardiovascular Surgery*, 114(5):738–745, 1997.

[168] Adel M Malek, Robert Jackman, Robert D Rosenberg, and Seigo Izumo. Endothelial expression of thrombomodulin is reversibly regulated by fluid shear stress. *Circulation Research*, 74(5):852–860, 1994.

[169] Ruo H. Song, Hrachya K. Kocharyan, John E. Fortunato, Seymour Glagov, and Hisham S. Bassiouny. Increased flow and shear stress enhance in vivo transforming growth factor-β1 after experimental arterial injury. *Arteriosclerosis, Thrombosis, and Vascular Biology*, 20(4):923–930, 2000.

[170] Hiroto Ueba, Masanobu Kawakami, and Toshio Yaginuma. Shear stress as an inhibitor of vascular smooth muscle cell proliferation: Role of transforming growth factor-β1 and tissue-type plasminogen activator. *Arteriosclerosis, Thrombosis, and Vascular Biology*, 17(8):1512–1516, 1997.

[171] CG Caro, JM Fitz-Gerald, and RC Schroter. Atheroma and arterial wall shear observation, correlation and proposal of a shear dependent mass transfer mechanism for atherogenesis. *Proceedings of the Royal Society of London. Series B. Biological Sciences*, 177(1046):109–133, 1971.

[172] Patrick Ozanne, Robert B Francis, and Herbert J Meiselman. Red blood cell aggregation in nephrotic syndrome. *Kidney Int*, 23(3):519–525, 1983.

[173] SL Diamond, SG Eskin, and LV McIntire. Fluid flow stimulates tissue plasminogen activator secretion by cultured human endothelial cells. *Science*, 243(4897):1483–1485, 1989.

[174] Nitzan Resnick, Tucker Collins, William Atkinson, David T Bonthron, C Forbes Dewey, and Michael A Gimbrone. Platelet-derived growth factor

B chain promoter contains a cis-acting fluid shear-stress-responsive element. *Proceedings of the National Academy of Sciences*, 90(10):4591–4595, 1993.

[175] Marina Noris, Marina Morigi, Roberta Donadelli, Sistiana Aiello, Marco Foppolo, Marta Todeschini, Silvia Orisio, Giuseppe Remuzzi, and Andrea Remuzzi. Nitric oxide synthesis by cultured endothelial cells is modulated by flow conditions. *Circulation Research*, 76(4):536–543, 1995.

[176] AM Malek, GH Gibbons, VJ Dzau, and S Izumo. Fluid shear stress differentially modulates expression of genes encoding basic fibroblast growth factor and platelet-derived growth factor B chain in vascular endothelium. *Journal of Clinical Investigation*, 92(4):2013, 1993.

[177] Anthony M Imparato, Thomas S Riles, and Frederick Gorstein. The carotid bifurcation plaque: pathologic findings associated with cerebral ischemia. *Stroke*, 10(3):238–245, 1979.

[178] Ross G Gerrity, Jennifer A Goss, and Lynn Soby. Control of monocyte recruitment by chemotactic factor (s) in lesion-prone areas of swine aorta. *Arteriosclerosis, Thrombosis, and Vascular Biology*, 5(1):55–66, 1985.

[179] Michael Gimbrone, James N. Topper, Tobi Nagel, Keith R Anderson, and Guillermo Garcia-Gardena. Endothelial dysfunction, hemodynamic forces, and atherogenesisa. *Annals of the New York Academy of Sciences*, 902(1):230–240, 2000.

[180] David N. Ku. Blood flow in arteries. *Annual Review of Fluid Mechanics*, 29(1):399–434, 1997.

[181] David N Ku and Don P Giddens. Pulsatile flow in a model carotid bifurcation. *Arteriosclerosis, Thrombosis, and Vascular Biology*, 3(1):31–39, 1983.

[182] S Glagov, C Zarins, DP Giddens, and DN Ku. Hemodynamics and Atherosclerosis. insights and perspectives gained from studies of human arteries. *Archives of Pathology Laboratory Medicine*, 112(10):1018–1031, 1988.

[183] AB Schelin, Gy Károlyi, APS De Moura, NA Booth, and C Grebogi. Chaotic advection in blood flow. *Physical Review E*, 80(1):016213, 2009.

[184] Véronique Peiffer, Spencer J Sherwin, and Peter D Weinberg. Computation in the rabbit aorta of a new metric–the transverse wall shear stress–to quantify the multidirectional character of disturbed blood flow. *Journal of Biomechanics*, 46(15):2651–2658, 2013.

[185] R Ross. George lyman duff memorial lecture. Atherosclerosis: a problem of the biology of arterial wall cells and their interactions with blood components. *Arteriosclerosis, Thrombosis, and Vascular Biology*, 1(5):293–311, 1981.

[186] John H Ip, Valentin Fuster, Lina Badimon, Juan Badimon, Mark B Taubman, and James H Chesebro. Syndromes of accelerated Atherosclerosis: role of vascular injury and smooth muscle cell proliferation. *Journal of the American College of Cardiology*, 15(7):1667–1687, 1990.

[187] Michael P Bevilacqua, JS Pober, M Elyse Wheeler, RS Cotran, and MA Gimbrone Jr. Interleukin-1 activation of vascular endothelium. effects on procoagulant activity and leukocyte adhesion. *The American journal of pathology*, 121(3):394, 1985.

[188] R Wayne Alexander. Hypertension and the pathogenesis of Atherosclerosis oxidative stress and the mediation of arterial inflammatory response: a new perspective. *Hypertension*, 25(2):155–161, 1995.

[189] Lars Lind, Jessika Andersson, Anders Larsson, and Bo Sandhagen. Shear stress in the common carotid artery is related to both intima-media thickness and echogenecitythe prospective investigation of the vasculature in uppsala seniors study. *Clinical hemorheology and microcirculation*, 43(4):299–308, 2009.

[190] GD Giannoglou, JV Soulis, TM Farmakis, DM Farmakis, and GE Louridas. Coronary vessel wall thickening in relation to velocity and viscosity distribution. In *Computers in Cardiology 2000*, pages 683–686. IEEE, 2000.

[191] C.H. Kao, J.K. Chen, J.S. Kuo, and V.C. Yang. Visualization of the transport pathways of low density lipoproteins across the endothelial cells in the branched regions of rat arteries. *Atherosclerosis*, 116(1):27 – 41, 1995.

[192] J. Boyd, J. Buick, J. A. Cosgrove, and P. Stansell. Application of the Lattice Boltzmann model to simulated stenosis growth in a two-dimensional carotid artery. *Physics in Medicine and Biology*, 50(20):4783–4796, 2005.

[193] Wolfgang Steinke, Christof Kloetzsch, and Michael Hennerici. Carotid artery disease assessed by color Doppler flow imaging: correlation with standard Doppler sonography and angiography. *American Journal of Neuroradiology*, 11(2):259–266, 1990.

[194] James Dix and James Skrocki. Evaluation of carotid stenosis by angiography: potential bias toward overestimated measurements introduced by prior interpretation of Doppler sonograms. *American Journal of Neuroradiology*, 21(4):639–642, 2000.

[195] Chun Yuan, William S Kerwin, Vasily L Yarnykh, Jianming Cai, Tobias Saam, Baocheng Chu, Norihide Takaya, Marina S Ferguson, Hunter Underhill, Dongxiang Xu, Fei Liu, and Thomas Hatsukami. MRI of Atherosclerosis in clinical trials. *NMR in Biomedicine*, 19(6):636–654, 2006.

[196] Michele Anzidei, Alessandro Napoli, Beatrice Cavallo Marincola, Miles A Kirchin, Cristina Neira, Daniel Geiger, Fulvio Zaccagna, Carlo Catalano, and Roberto Passariello. High-resolution steady state magnetic resonance angiography of the carotid arteries: are intravascular agents necessary?: feasibility and preliminary experience with gadobenate dimeglumine. *Investigative Radiology*, 44(12):784–792, 2009.

[197] Tamie L Poepping, N Nikolov, N Rankin, Mark Lee, and David W Holdsworth. An in vitro system for Doppler ultrasound flow studies in the stenosed carotid artery bifurcation. *Ultrasound in Medicine & Biology*, 28(4):495–506, 2002.

[198] David A Steinman, Tamie L Poepping, Mauro Tambasco, Richard N Rankin, and David W Holdsworth. Flow patterns at the stenosed carotid bifurcation: effect of concentric versus eccentric stenosis. *Annals of Biomedical Engineering*, 28(4):415–423, 2000.

[199] Ian Marshall, Shunzhi Zhao, Panorea Papathanasopoulou, Peter Hoskins, and X Yun Xu. MRI and CFD studies of pulsatile flow in healthy and stenosed carotid bifurcation models. *Journal of Biomechanics*, 37(5):679–687, 2004.

[200] Mark W Siebert and Petru S Fodor. Newtonian and non-Newtonian blood flow over a backward-facing step–a case study. In *COMSOL Conference*, pages 1–5, 2009.

[201] WY Chan, Y Ding, and JY Tu. Modeling of non-Newtonian blood flow through a stenosed artery incorporating fluid-structure interaction. *Anziam Journal*, 47:507–523, 2007.

[202] Johannes V Soulis, George D Giannoglou, Yiannis S Chatzizisis, Kypriani V Seralidou, George E Parcharidis, and George E Louridas. Non-Newtonian

models for molecular viscosity and wall shear stress in a 3D reconstructed human left coronary artery. *Medical Engineering & Physics*, 30(1):9–19, 2008.

[203] FJH Gijsen, FN van de Vosse, and JD Janssen. The influence of the non-Newtonian properties of blood on the flow in large arteries: steady flow in a carotid bifurcation model. *Journal of Biomechanics*, 32(6):601–608, 1999.

[204] WL Siauw, EYK Ng, and J Mazumdar. Unsteady stenosis flow prediction: a comparative study of non-Newtonian models with operator splitting scheme. *Medical Engineering & Physics*, 22(4):265–277, 2000.